# ELECTRO-ABSORPTION IN InGaAs-GaAs STRAINED-LAYER MULTIPLE QUANTUM WELL WAVEGUIDE MODULATORS

by

**NEIL EDMUND JAMES HUNT, B.Sc., M.Sc.**

A Thesis

Submitted to the School of Graduate Studies

in Partial Fulfilment of the Requirements

for the Degree

Doctor of Philosophy

McMaster University

September 1991

# ELECTRO-ABSORPTION IN InGaAs-GaAs QUANTUM WELL WAVEGUIDES

**DOCTOR OF PHILOSOPHY (1991)** McMASTER UNIVERSITY

(Engineering Physics) Hamilton, Ontario

**TITLE:** Electro-Absorption in InGaAs-GaAs Strained-Layer Multiple Quantum Well Waveguide Modulators.

**AUTHOR:** Neil Edmund James Hunt, B.Sc. (University of Waterloo)

M.Sc. (McMaster University)

**SUPERVISOR:** Professor P. E Jessop

**NUMBER OF PAGES:** xxiv, 180

# ABSTRACT

Electric field induced changes in the excitonic band-edge absorption spectra of Multiple Quantum-Well (MQW) structures were investigated theoretically and experimentally. Three $In_xGa_{1-x}As$-GaAs quantum-well p-i-n waveguide structures were designed, and were then grown by the National Research Council of Canada. Band edge absorption changes with field were then investigated using light incident perpendicular to the sample surface. Theoretically, a comparison was made of three different exactly solvable methods for calculating quantum-well energies in an electric field, both with and without conduction-band non-parabolicity. An exactly solvable method was used to calculate the hole dispersion and thereby determine the heavy-hole parallel effective mass. By using calculated wavefunctions, and these mass values, a numerical method was used [Wu, 1989] to solve for the exciton binding energies. After determining broadening factors, the absorption edge was calculated at low and moderate fields for three $In_xGa_{1-x}As$-GaAs structures for various fields. At high fields, a different Franz-Keldysh type of absorption calculation was developed. Comparisons vs. experiment were favourable, but some discrepancy was noted. Slab and rib waveguide modulators, with operating wavelengths from about 970nm to 1035nm, were processed from the three material growths. Waveguiding transmission spectra again agreed favourably with theory, although some differences were seen. The modulators typically exhibited greater than 20 dB of switching over a 40nm range with less than 2 dB of low-bias absorption loss. Switching speed was not examined. Theoretical analysis of different structures revealed many trade-offs, in design, with 3% to 17% indium, and 6.5nm to 13nm well-widths being acceptable.

# ACKNOWLEDGEMENTS

The work in this thesis is a compilation of ideas learned during my years at McMaster University. Therefore much credit must go to the colleagues and teachers that I have met throughout my studies. Thanks goes to my committee members, Dr. John Simmons and Dr. Dave Thompson, and particularly my supervisor Dr. Paul Jessop for providing encouragement and guidance, yet allowing me considerable freedom in my choice of work. I would also like to thank all the members of the opto-electronics group in the Engineering Physics department. Specific thanks should go to Doug Bruce for his knowledge and help, Mike Daly for encouraging me to pursue some theoretical calculations and for his discussions about modulators. I would also like to thank Cindy Chippindale for her ideas and for acting as 'sub basement' social convenor. I would also like to thank Jugnu Ojha and Steve Kovacic for their discussions and input on just about everything.

Specific contributions to this work were done by Alok Chakrabarti, who did some photoluminescence spectra, and by John Bowron who took some scanning photoluminescence micrographs of my samples. I would also like to thank the Ontario Laser and Lightwave Research Centre (OLLRC) for allowing me to use their Titanium-Sapphire laser and facilities. I thank Dr. Z.R. Wasilewski at NRCC for growing the structures used in this work. This work was partly supported by the Natural Sciences and Engineering Research Council of Canada.

Special thanks goes to my parents for encouraging me to learn and to pursue excellence. Most of all, I would like to thank my wife, Mary, who has put up with me during this work. I don't know what I would do without your love and support.

# TABLE OF CONTENTS

## LIST OF FIGURES

# LIST OF TABLES

# CHAPTER 1

# Introduction to Quantum-Well Devices

## 1.1 Introduction

Quantum-well structures have attracted a lot of attention in recent years for their use in semiconductor device applications. The quantum-confinement of carriers in one direction causes interesting changes to the electronic and optical properties of a material. These changes prove useful in lasers [Weisbuch, 1987], modulators [Miller, 1985], wavelength selective detectors [Larsson, 1988], and Self Electro-Optic Effect Devices (SEEDs) [Chemla, 1985][Weiner, 1987]. In this thesis, $In_xGa_{1-x}As$-GaAs quantum-well waveguide modulators will be studied. In this chapter, the unique properties of quantum-wells will be explained, and their importance to the performance of a number of devices, including modulators, will be mentioned.

For the particular case of the waveguide quantum-well modulator, it is important to understand the cause of electric-field induced changes in the band-edge absorption. As the absorption at a wavelength near the band edge changes, the modulator can switch from an optically transparent to optically opaque state. The cause of these absorption changes, the Quantum-Confined Stark Effect (QCSE) [Miller, 1984], will therefore be explained.

## 1.2 Properties of Quantum Wells

A quantum well consists of a thin layer of one type of semiconductor

sandwiched in between two layers of different material. This middle layer has a band structure such that the electrons or holes (or both) experience a potential well in that layer. In most cases, there exist discrete bound states for the carriers within this potential well. This is in contrast to the bulk case where there is a continuum of states. A typical situation is given in Figure 1.1.

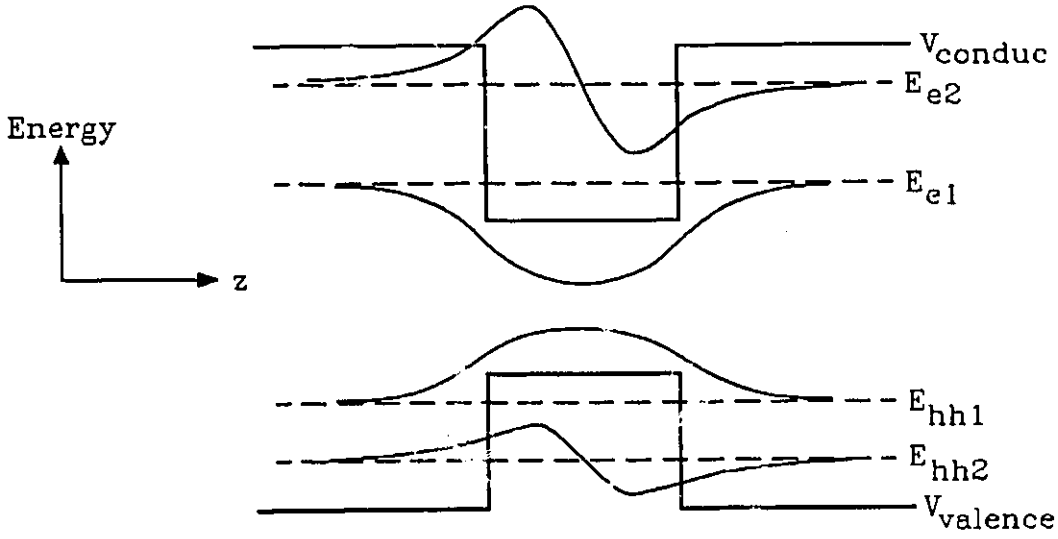


**Figure 1.1** The band structure vs. position for a typical single quantum well. Also shown are two electron and two heavy hole energy states and their corresponding wavefunctions.

While only the heavy-hole states are shown in this figure, there are light hole states as well. For the particular case of $In_xGa_{1-x}As$-GaAs quantum wells, however, the combination of material strain and different effective masses combine to ensure that the hole solution with the largest electron energy (lowest hole energy) is the heavy-hole result $E_{hh1}$ [Hunt, 1988b]. This means that the lowest energy optical transition (neglecting defects) is from the $E_{e1}$ to $E_{hh1}$ states. So, to realize how these differences will affect device performance one must first compare the density of

states of a bulk material to that of a quantum-well. This comparison is done for the conduction band in Figure 1.2. The valence band comparison would be similar, except that it would include contributions from both light and heavy holes.

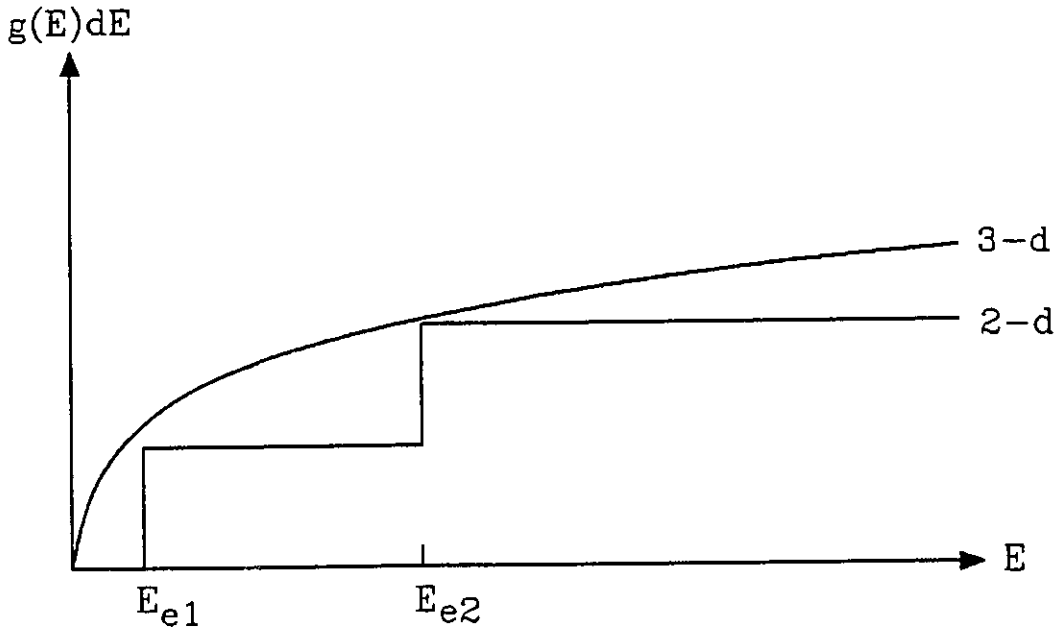


**Figure 1.2** Electron density of states curves vs. electron energy for a typical 3-d (bulk) and 2-d (quantum well) situation.

The absorption spectrum is determined from this step-like density of states. The absorption spectrum (for no carrier population) is also an approximately step-like shape, with the addition of absorption peaks due to excitons [Elliott, 1952], at energies just below the step edges. These Wannier excitons are mobile hydrogenic states involving the confined electrons and holes. In reality, there is broadening of all transitions due to lifetime effects and structural variations, so the absorption spectrum will look similar to that shown in Figure 1.3. Ignored here is the effect of Coulomb scattering of free carriers travelling parallel to the layer planes. This slightly modifies the step-like shape of the density of states plots, and of the

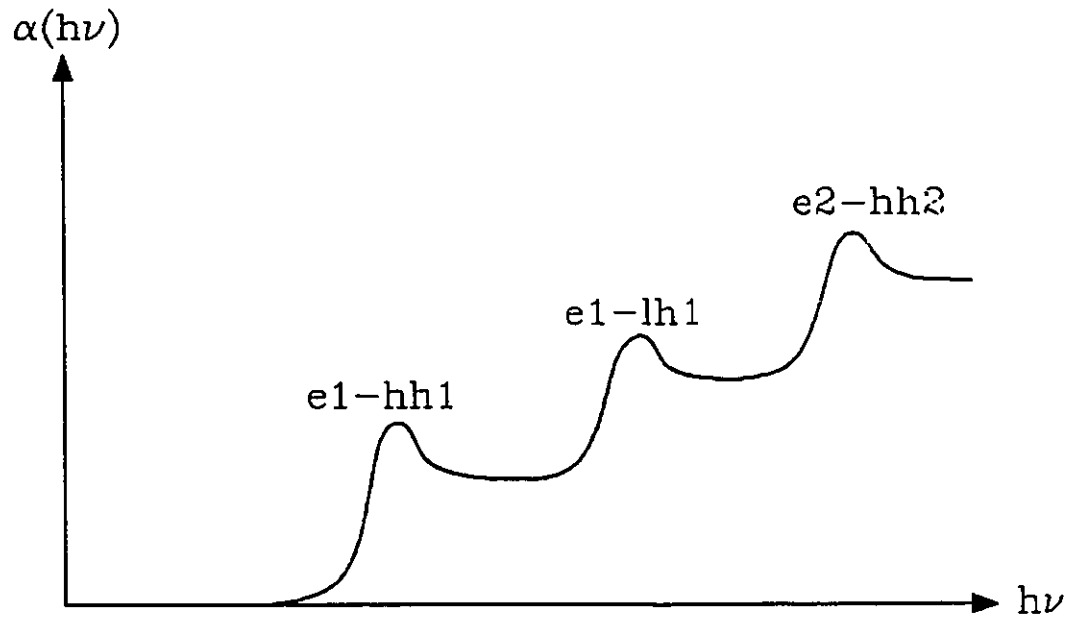


**Figure 1.3** A graph of a typical absorption coefficient vs. photon energy for a quantum well. In our InGaAs-GaAs quantum wells, the e1-lh1 transition is very weak.

absorption spectra. Also, in the case of multiple quantum wells (MQWs) where the wavefunctions between nearby wells overlap, there are also small differences in the absorption spectra. These differences will be addressed in later chapters, but will be shown not to be important for the MQWs experimentally investigated in this work.

## 1.3 The Use of Quantum Wells in Semiconductor Devices

The unique step-like density of states curve in quantum well structures is advantageous for use in semiconductor lasers. Because the carriers do not have to fill up the useless low density of states band-edge region of bulk materials, but will initially achieve population inversion at an energy where enough gain will occur for lasing, less carrier density is needed [Weisbuch, 1987]. This translates into a lower

threshold current for lasing. The density of states shape also results in a reduced sensitivity of threshold current to temperature (meaning an increased $T_0$).

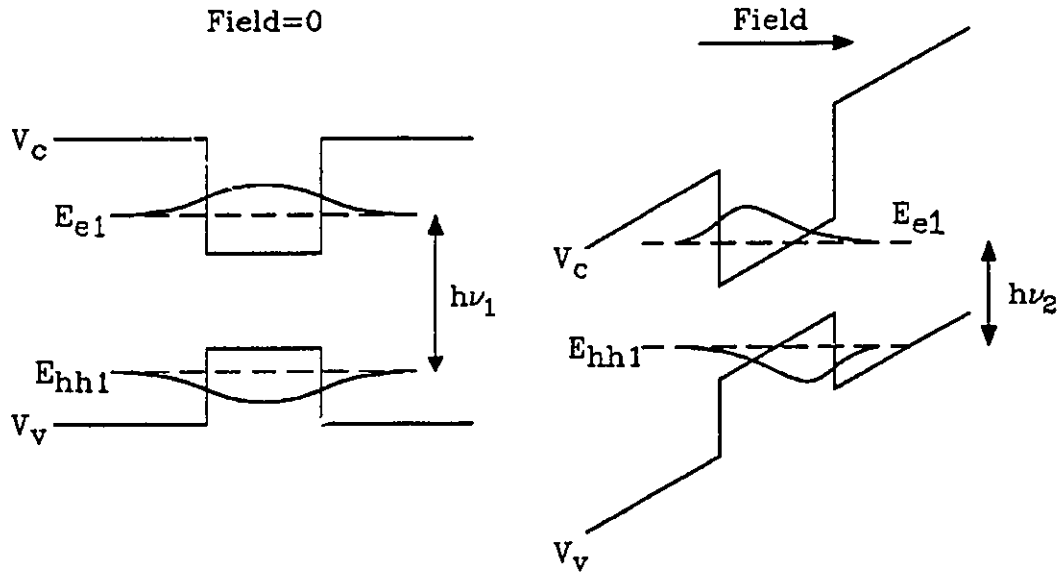


**Figure 1.4** The conduction and heavy-hole band diagrams with and without an applied field. Shown are the wavefunctions and energies corresponding to the lowest energy transition.

For photon energies lower than the e1-hh1 band edge, quantum wells are transparent to light, and can therefore be used in waveguide structures. They can also be used in waveguide modulators, the topic of this work, and in wavelength selective detectors [Larsson, 1988]. In either device, one applies an electric field to the sample, which shifts the absorption edge to longer wavelength. This effect, known as the Quantum-Confined Stark Effect (QCSE) can be explained by Figure 1.4. With the applied field, the wavefunction probability shifts to one side of the well, and the energy solutions for the electrons and holes approach each other. The lowest energy transition decreases, as shown in the figure since $h\nu_2 < h\nu_1$. The band edge therefore shifts to longer wavelength. This can change the absorption

coefficient for a wavelength just below the zero-field bandgap from a small value to a large value, as the edge shifts.

An experimental example of this change for the InGaAs-GaAs material 'B' investigated in this work is shown in Figure 1.5.

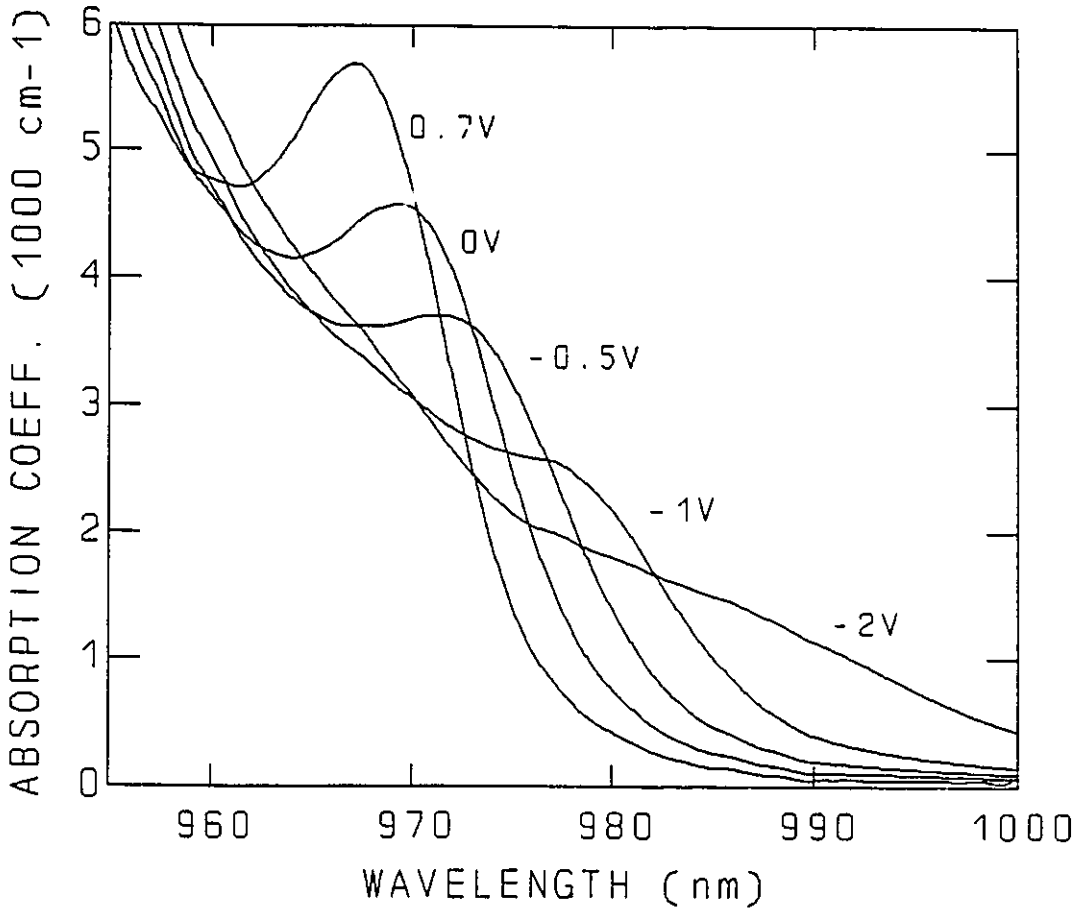


**Figure 1.5** Spectra of absorption coefficients at various bias voltages for the InGaAs-GaAs MQW sample B (described later).

A similar effect, called the Franz-Keldysh effect [Franz, 1958][Aspnes, 1966], occurs in bulk semiconductors also. Because of the sharp zero-field absorption edge of the quantum-well, however, one finds that it easier to get high contrast ratios between

an on and off state. One can also operate a modulator closer to the band-edge without getting high on-state absorption losses. Operating close to the band edge means that the possible absorption coefficient changes are quite high, even at moderate fields. This large absorption change allows the use of a shorter interaction length to reduce the device capacitance. The reduced field requirement may be used to either reduce voltage requirements, or can reduce capacitance further through use of a thicker intrinsic region. If one is willing to go to high fields, longer wavelength, and larger interaction lengths, however, it will be also shown in this work that InGaAs-GaAs quantum well modulators can give better than 20dB of switching with very small low-field loss over a wavelength range of over 50nm.

Another advantage of quantum wells is bandgap tailorability. Depending on the bandgap of the well material, as well as the depth and width of the wells, the effective bandgap will have different values. Now, by using ternary and quaternary bulk materials, the bandgaps of bulk semiconductors can also be varied, but these must always be lattice matched to their substrates to avoid dislocations. In quantum wells, however, the lattice matching requirement is relaxed since the mismatch can be accommodated in a thin epilayer through strain [Osbourn, 1982]. As long as the individual epilayers are less than some critical thickness [Hunt, 1988b] for those layers, and as long as the entire MQW structure is thinner than some other critical thickness based on its average strain, epitaxial growth will occur. The relaxation of the lattice matching requirement, then, allows greater flexibility of material combinations and operating wavelengths.

## 1.4 An Outline of the Thesis Work

In this work, three $In_{.14}Ga_{.86}As$-GaAs Multiple Quantum Well (MQW)

strained-layer waveguide modulator structures are investigated. The ultimate purpose of modulators made from these materials would be either for high speed modulation of existing lasers, or for integration into some switching matrix. It was felt, however, that since $In_xGa_{1-x}As$-GaAs modulators have not been investigated to the same extent as GaAs- $Al_xGa_{1-x}As$ structures, that the focus of this work should be to understand the electro-absorption process in these growths, rather than to produce a commercially practical device. This decision also made sense from the point of view of the device processing facilities available, and the lack of a moderate-power tunable light source for high speed measurements.

The particular properties of the $In_{.14}Ga_{.86}As$-GaAs structures which may be important to the modulator operation are the shallow wells and the layer strain. Shallow wells give good confinement of the carriers at low fields, but at high fields the confinement is poor, and the carriers tunnel quickly out of the wells. This results in a considerable field-induced lifetime broadening of the band-edge. Depending on the wavelength of modulator operation, this may positively or adversely affect device performance. The layer strain splits the bulk heavy- and light-hole bands, which in our materials ensure that the lowest energy optical transition is the e1-hh1 feature. It also causes the light holes to be confined to the GaAs layers, separating them from the electrons confined to the InGaAs layer. The light holes can then be effectively ignored when looking at the band-edge absorption.

A number of authors have done good work modelling absorption spectra for no applied field [Sanders, 1985]. The QCSE has been studied by a number of authors [Miller, 1984], and has been used to explain band-edge changes in both AlGaAs-GaAs systems [Kan, 1987][Tarucha, 1987] and InGaAs-GaAs systems [Coffey, 1988]. However, to my knowledge no-one has included enough effects to be

able to accurately model the band-edge shape with field for shallow-well InGaAs-GaAs quantum wells. In this work, the band-edge electroabsorption is investigated experimentally through a variety of transverse spectroscopy methods. In order to understand these band-edge changes, a number of calculations have been done. Three exactly solvable methods are compared for calculating the QCSE energy shifts with field (ignoring Coulomb interaction) and the corresponding carrier wavefunctions. Exactly solvable calculations of parallel hole dispersion curves are done to determine the hole parallel effective mass. This is not an obvious value, and is ignored by many authors. The wavefunctions and masses are then used for calculating the exciton wavefunctions and binding energies. After calculating some field-dependant broadening factors, and using some 0V-bias fitting parameters, the electro-absorption is theoretically calculated for the material structures. While theory and experiment show some differences, they compare well in the long-wavelength band-tail, where waveguide modulators operate. General conclusions about the performance of these and other structures in waveguide modulators will be made. Slab and rib waveguide modulators are also tested, and their low-frequency performance compared with theory.

# CHAPTER 2

## Material Structure Design and Material Quality

### 2.1 Introduction

In this chapter, the material layers will be described for the three growths investigated in this work. The justification behind the designs will be given, including calculations of band structure, quantum-well energies, and waveguiding modes shown. The material growth quality will also be commented on, and a scanning photoluminescence micrograph of one structure will be displayed.

### 2.2 The Design of the Material Structures

Three material structures were investigated in this thesis. The structures were grown by MBE (Molecular Beam Epitaxy) by Dr. Z.R. Wasilewski at The National Research Council of Canada. The growths will be labelled A,B, and C in this work. The following table compares these letter designations to the NRC growth numbers.

**Table 2.1** Growths labels A, B, and C, and their NRC growth numbers

| Thesis Label | NRC Growth |
|---|---|
| A | 693 |
| B | 1032 |
| C | 1031 |

The actual structures were designed so that they would be single-mode slab

waveguides for light with photon energy less than the Multiple Quantum Well (MQW) bandgap energy. The results of waveguiding calculations will be shown in Chapter 8. The first structure A is shown in Figure 2.1.

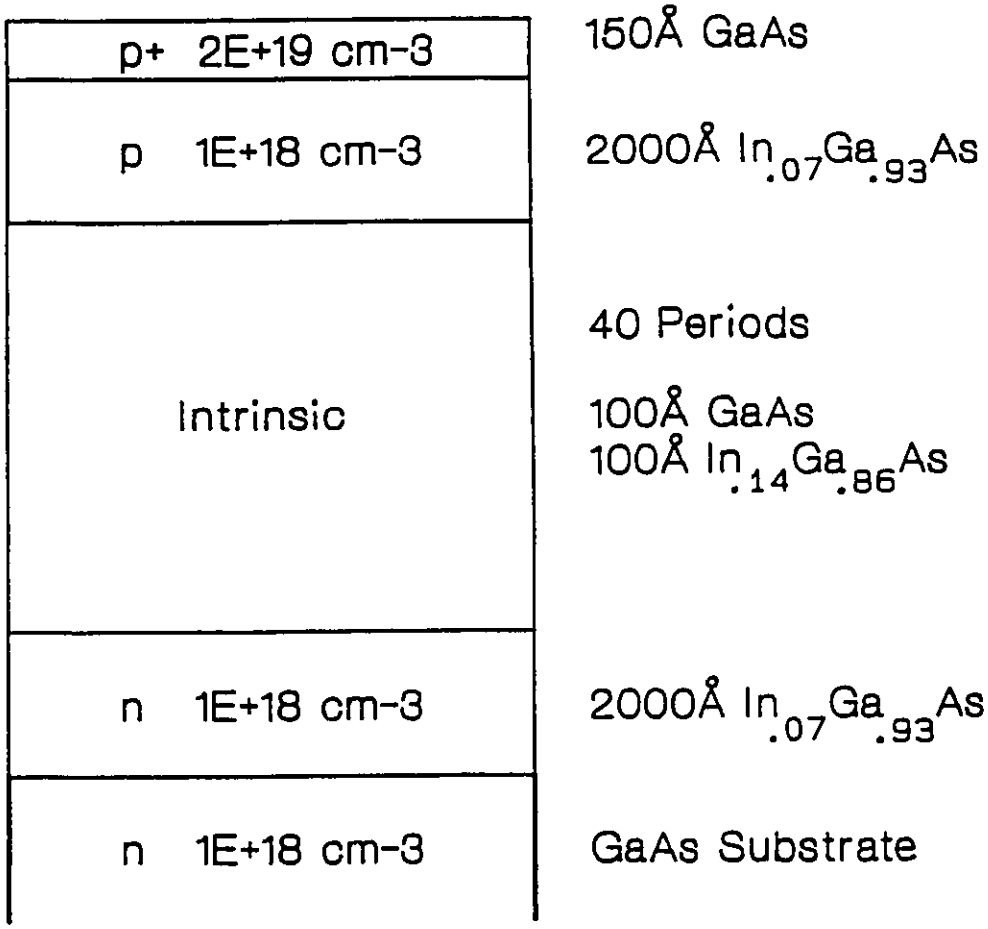


**Figure 2.1** The growth structure of material A of this thesis, consisting of a 40-period MQW waveguide in the intrinsic region of a p-i-n diode. Shown are the nominal 'as-specified' thicknesses and compositions.

Because the entire waveguiding layer consists of quantum wells, the interaction between the MQW region and the waveguiding mode is high. This means that for the waveguide to be transparent at a particular wavelength near the band edge, either the absorption coefficient must be low, or the waveguide length must be short. Because we could not cleave waveguides much shorter than 300$\mu$m in length, the

absorption coefficient must be less than about $30cm^{-1}$ for transmission. The waveguiding absorption edge, then, will be positioned considerably into the long-wavelength band tail of the band edge.

| | | |
|---|---|---|
| p+ | GaAs | 7nm |
| p+ | $In_{.07}Ga_{.93}As$ | 90nm |
| p | $In_{.07}Ga_{.93}As$ | 240nm |
| i | $In_{.07}Ga_{.93}As$ | 90nm |
| i | GaAs | 9nm |
| i | 5 periods { $In_{.14}Ga_{.86}As$ 9nm / GaAs 9nm | |
| i | $In_{.07}Ga_{.93}As$ | 90nm |
| n | $In_{.07}Ga_{.93}As$ | 390nm |
| n | Superlattice buffer | 37nm |
| n | GaAs substrate | |

**Figure 2.2** The material growth structure B, consisting of a 5-period MQW with InGaAs layers to increase the waveguide thickness. Doping is $3x10^{17}$ $cm^{-3}$ for n and p InGaAs layers.

The structure of material growth B is shown in Figure 2.2. The quantum-wells are similar to those of material A, except with slightly thinner layers. The main difference is the low number of wells -- 5 as compared to 40. This provides a smaller interaction with a waveguiding mode, and results in less absorption for the same absorption coefficient. One should therefore be able to get waveguiding transmission

in this structure at wavelengths closer to the band-edge than in material A. As with growth A, material B is a strained structure, with a total thickness larger than the critical value for non-dislocated growth. The epilayers will therefore be dislocated from the substrate at that interface [Hunt, 1988b]. The individual epilayers, however, should be strained to the same lattice constant, which will probably be very close to the unstrained lattice constant of $In_{.07}Ga_{.93}As$. Because the MQW structure itself is too thin to support a single waveguiding mode, the $In_{.07}Ga_{.93}As$ layers were sandwiched on either side. Since part of the InGaAs thickness is intrinsic, these layers also serve to increase the thickness of the intrinsic region of the p-i-n diode. This reduces the field at zero bias. The zero-bias field will still be larger than in material A, however, and less applied voltage will be required to produce large internal fields. A $2x10^{19}$ $cm^{-3}$ p+ doping is used on the upper contact layer, and the n-substrate is doped to $1x10^{18}$ $cm^{-3}$. The nominal layer thicknesses within the MQW were 10nm, not 9nm, but since samples were taken halfway to the wafer edge, it was believed that the thickness was less.

The individual quantum wells in material C are similar to those in the other two growths, although here there are only 3 periods. The main difference in this growth is that the MQW layers are thinner than the critical thickness for non-dislocated growth. Therefore the MQW layers will be strained to the GaAs substrate lattice constant. One purpose of growing this structure is to see if this different strain has any effect on waveguiding modulator performance. The surrounding AlGaAs layers act as waveguide cladding, and have approximately the same lattice constant as GaAs. Because the lattice mismatch is accommodated by elastic strain instead of dislocations, one would expect there to be fewer dislocations throughout the epilayers. Because of the variation of layer thickness across the growth wafer,

the individual layers within the growth were assumed to be 90% of the nominal values for samples taken halfway to the wafer edge. This is included in the dimensions of Figure 2.3. Optical field profiles are given in section 8.3.

| | | | |
|---|---|---|---|
| p+ | 2E+19 $cm^{-3}$ | GaAs | 13.5 nm |
| p+ | 2E+19 $cm^{-3}$ | $Al_{.20}Ga_{.80}As$ | 90 nm |
| p | 3E+17 $cm^{-3}$ | $Al_{.20}Ga_{.80}As$ | 180 nm |
| p | 5E+17 $cm^{-3}$ | GaAs | 63 nm |
| i | | GaAs | 22.5 nm |
| i | 3 periods | GaAs | 9 nm |
| | | $In_{.14}Ga_{.86}As$ | 9 nm |
| i | | GaAs | 45 nm |
| n | 5E+17 $cm^{-3}$ | GaAs | 63 nm |
| n | 3E+17 $cm^{-3}$ | $Al_{.30}Ga_{.70}As$ | 720 nm |
| n | 6E+17 $cm^{-3}$ | Superlattice Buffer | 27 nm |
| n | 4E+17 $cm^{-3}$ | GaAs Substrate | |

**Figure 2.3** The growth structure for material C, consisting of 3 MQW periods, InGaAs layers for a thicker waveguiding region, and AlGaAs cladding layers.

## 2.3 Wafer Uniformity and Material Quality

The wafer growths were not uniform in thickness or composition from centre to edge. It is believed that material A is more uniform than either B or C. Growths B and C were done on the same day, and the growers say that thickness uniformity

was worse than usual. As a test of uniformity, room temperature photoluminescence spectra were taken at difference radii from the centre of growths A and C. The results are shown in Figures 2.4 and 2.5. There was difficulty getting a reasonable photoluminescence spectrum from growth B, probably because the internal field was preventing the photogenerated carriers from diffusing down into the quantum wells.

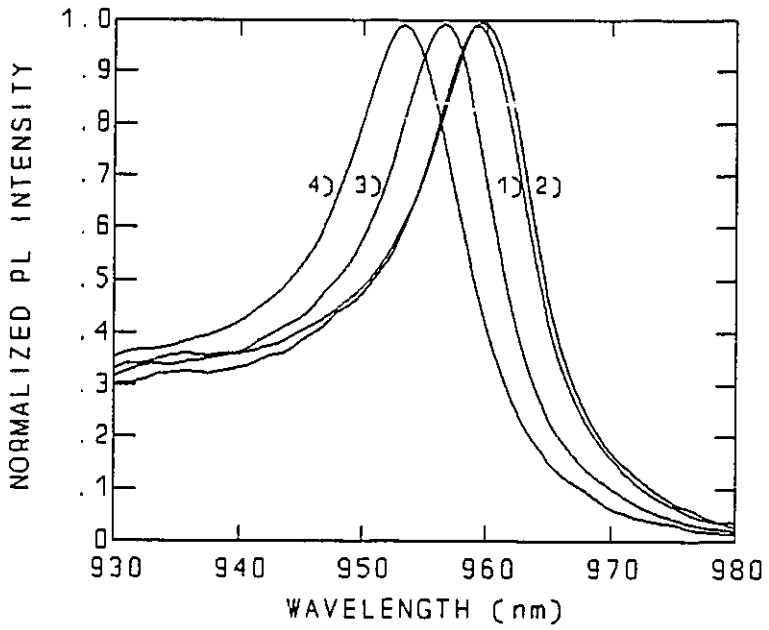


**Figure 2.4** Normalized photoluminescence spectra at various positions on wafer growth A. Graphs are at 1) wafer centre, 2) 1/4" from centre, 3) 1/2" from centre, and 4) 3/4" from centre. The wafer radius was one inch.

At very high pump intensity, only a faint, very broad peak was seen. The shifts of the photoluminescence peaks to shorter wavelength with increasing radius can partially be accounted for by a decrease in layer thicknesses. Because of the magnitude of the shifts, however, much of the change must be due to a drop in indium concentration in the wells at the wafer edges. One can notice, however, that growth A is much more uniform than growth C (and probably B).

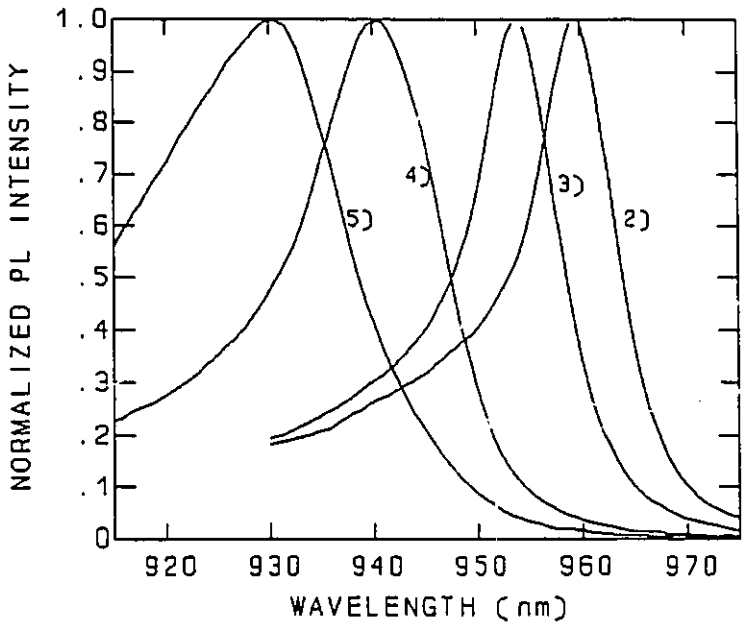


**Figure 2.5** Normalized photoluminescence spectra at different spots across material wafer C. The positions are 2) 1/4" from centre, 3) 1/2" from centre, 4) 3/4" from centre, and 5) barely on epilayer.

There is considerable uncertainty in the indium concentration in any particular sample. We are therefore justified in treating the indium concentrations in the quantum wells as free parameters. The indium concentration in the bulk $In_{.07}Ga_{.93}As$ layers will then be scaled by the same adjustment factor. The indium concentration was adjusted until the calculated photoluminescence position for any one sample matched that which was measured. All samples used were just over 1/2 inch from the wafer centre.

Material quality can be defined by a number of factors. The electrical quality can be determined by how small the reverse-bias leakage current is, and by how fast a device degrades. In reverse bias, modulators or detectors made from these structures should not degrade except at very high field, or with high photocurrents. The limit of current was not determined. In forward bias, strained-layers tend to

degrade with time. Continuous-wave (CW) lasers made from InGaAs-GaAs strained layers (dislocated from the substrate) have been shown by others to last only as long as 15 minutes [Ludowise, 1983]. Strained-layer lasers, with only a few thin wells strained to the substrate lattice constant, are better and are commercially available.

The uniformity of the interfaces between different layers of the MQW are also important to modulator performance. Uniform thickness wells result in narrower exciton features in photoluminescence, and a sharper band-edge in absorption. This uniformity is especially important in narrower wells. Low temperature photoluminescence (PL) spectra of growth A show exciton widths of 6 meV. This width is due to both alloy broadening by the ternary well material, and the well-width variations. Although not the lowest seen in these materials [Hunt, 1988b], it is not bad. The best materials exhibit about 4-5 meV. The exciton PL widths increase at higher temperature, mainly due to scattering by phonons.

Dislocations within the structures affect the electrical properties, the exciton widths, and optical scattering within a waveguide. For structures A and B, dislocations are expected at the interface between the substrate the epilayers [Rajan, 1987], but some of these dislocations also thread up to the surface. These defects provide leakage current paths. They also scatter carriers and act as recombination centres. If enough are present, the band edge will be broadened, and the photoluminescence intensity will be decreased. We suspect that the PL intensity was in fact decreased, but no affect on the optical spectrum could be seen. The defects were seen to scatter light which was waveguiding through the structures. Some spots on a slab waveguide appeared dark, while others were bright. The same scattering was not seen to the same degree in growth C, and was definitely not seen in non-strained AlGaAs-GaAs MQW waveguides [Daly, 1990].

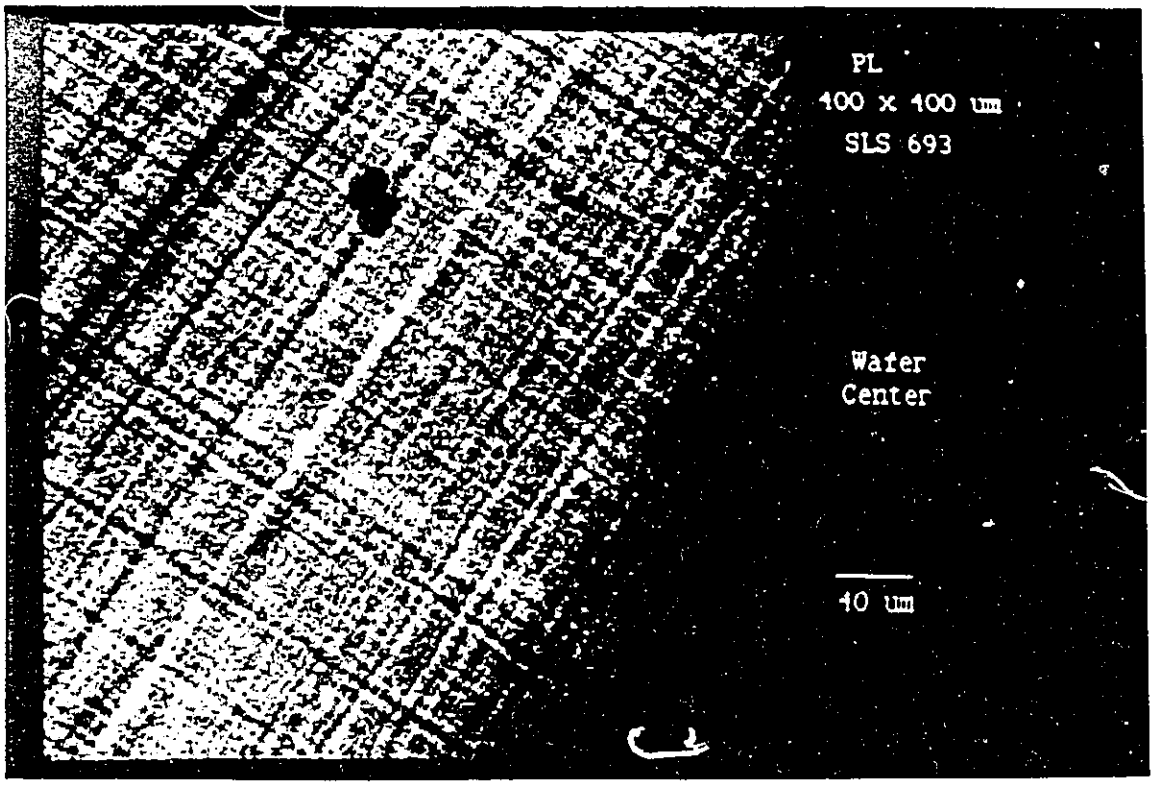


**Figure 2.6** Confocal scanning photoluminescence micrograph of a 400$\mu$m by 400$\mu$m square of material growth A. Enhancing the contrast clearly reveals dark lines, interpreted as being defects running along the lattice directions.

To the naked eye, the surfaces of growths A and B acted like gratings along the lattice planes. Growth B was the worst for this. Growth A, however, seemed much smoother. Lines could be seen in the first two growths under regular microscopy, but to investigate the surface better, samples from structure A were placed in a confocal scanning photoluminescence microscope, built and operated by J. Bowron, at the University of Waterloo. A typical picture (with contrast enhanced) is shown in Figure 2.6. Notice the numerous dark line defects running through the sample. The directions of the lines are parallel to the lattice planes.

## 2.4 The Multiple Quantum Well (MQW) Band Structure

The material parameters and the program BANDGP used to calculate the band positions and energies for InGaAs-GaAs MQWs are given in the masters thesis by Hunt [Hunt, 1988a]. The InGaAs wells undergo biaxial compressive strain, while the GaAs barriers have either biaxial tensile strain (as with growths A and B) or no strain (as with growth C). Biaxial tensile strain increases the bandgap, and splits the degenerate heavy-hole band above the light-hole band. For biaxial compressive strain, the bandgap decreases, and the heavy-hole band splits to become lower than the light-hole band. The calculated band positions, and lowest energy electron and hole solutions are given for the three growths in Tables 2.2, 2.3, and 2.4. The lowest energy interband transition is that involving the heavy-hole-1 with electron-1 Wannier exciton (a hydrogenic state not bound to a lattice site). This exciton, along with the broadened spectrum of free particle, higher energy heavy-hole-1 to electron-1 transitions, are the greatest contributors to band-edge absorption.

**Table 2.2** Material parameters for growth A. Shown are the bulk parameters, the strained-layer band energies and parameters, and the solved superlattice energies.

**Bulk Unstrained Material Parameters**

| | $Ga_{.892}In_{.108}As$ | GaAs |
|---|---|---|
| $S_{11}$ ($cm^2/10^{11}$ dyne) | .1256 | .1173 |
| $S_{12}$ ($cm^2/10^{11}$ dyne) | -.0400 | -.0366 |
| $S_{44}$ ($cm^2/10^{11}$ dyne) | .1774 | .1684 |
| Lattice Const. (Å) | 5.6972 | 5.6534 |
| Heavy-Hole Mass ($m_0$) | -.466 | -.450 |
| Light-Hole Mass ($m_0$) | -.076 | -.082 |
| Eff. Elec. Mass ($m_0$) | .062 | .067 |
| Hydrostatic Const. (eV) | -8.13 | -8.40 |
| Deformation Potential (eV) | -1.71 | -1.70 |
| Valence Band (eV) | .0254 | .0000 |
| Conduction Band (eV) | 1.2838 | 1.4247 |
| Band Gap (eV) | 1.2585 | 1.4247 |

**Superlattice Layer Parameters**

Fractional relaxation from substrate = .900

| | $Ga_{.892}In_{.108}As$ | GaAs |
|---|---|---|
| Stress ($10^{11}$ dyne/$cm^2$) | -.0483 | .0443 |
| Biaxial Strain | -.0041 | .0036 |
| Lattice Const. (Å) | 5.6736 | 5.6736 |
| Layer Thickness (Å) | 100.0 | 100.0 |
| Heavy-Hole Band (eV) | .0334 | -.0025 |
| Light-Hole Band (eV) | .0036 | .0189 |
| Conduction Band (eV) | 1.3115 | 1.3992 |

**Wavefunction Solution Energies**

| Solution # | Heavy-Hole (eV) | Light-Hole (eV) | Conduction (eV) |
|---|---|---|---|
| 1 | .0287 | .0095 | 1.3360 |
| 2 | .0152 | | |
| 3 | .0000 | | |

Assuming 8meV binding energy, the lowest energy exciton is at 9542.4 nm.

**Table 2.3** Material parameters for growth B. Shown are the bulk parameters, the strained layer band energies and parameters, and the solved superlattice energies.

**Bulk Unstrained Material Parameters**

| | $Ga_{.876}In_{.124}As$ | GaAs |
|---|---|---|
| $S_{11}$ ($cm^2/10^{11}$ dyne) | .1269 | .1173 |
| $S_{12}$ ($cm^2/10^{11}$ dyne) | -.0405 | -.0366 |
| $S_{44}$ ($cm^2/10^{11}$ dyne) | .1788 | .1684 |
| Lattice Constant (Å) | 5.7036 | 5.6534 |
| Heavy-hole Mass ($m_0$) | -.469 | -.450 |
| Light-hole Mass ($m_0$) | -.075 | -.082 |
| Eff. Elec. Mass ($m_0$) | .061 | .0667 |
| Hydrostatic Const. (eV) | -8.09 | -8.40 |
| Deformation Potential (eV) | -1.71 | -1.70 |
| Valence Band (eV) | .0291 | .0000 |
| Conduction Band (eV) | 1.2641 | 1.4247 |
| Band Gap (eV) | 1.2349 | 1.4247 |

**Superlattice Layer Parameters**

Fractional relaxation from substrate = .900

| | $Ga_{.876}In_{.124}As$ | GaAs |
|---|---|---|
| Stress ($10^{11}$ dyne/$cm^2$) | -.0547 | .0510 |
| Biaxial Strain | -.0047 | .0041 |
| Lattice Const. (Å) | 5.6767 | 5.6767 |
| Layer Thickness (Å) | 90.0 | 90.0 |
| Heavy-hole Band (eV) | .0388 | -.0025 |
| Light-hole Band (eV) | .0042 | .0218 |
| Conduction Band (eV) | 1.2954 | 1.3953 |

**Wavefunction Solution Energies**

| Solution # | Heavy-Hole (eV) | Light-Hole (eV) | Conduction (eV) |
|---|---|---|---|
| 1 | .0331 | .0106 | 1.3247 |
| 2 | .0169 | | |
| 3 | .0000 | | |

Assuming 8meV binding energy, the lowest energy exciton is at 9658.8 nm.

**Table 2.4** Material parameters for growth C. Shown are the bulk parameters, the strained-layer band energies and parameters, and the solved superlattice energies.

**Bulk Unstrained Material Parameters**

| | $Ga_{.882}In_{.118}As$ | CaAs |
|---|---|---|
| $S_{11}$ ($cm^2/10^{11}$ dyne) | .1264 | .1173 |
| $S_{12}$ ($cm^2/10^{11}$ dyne) | -.0403 | -.0366 |
| $S_{44}$ ($cm^2/10^{11}$ dyne) | .1783 | .1684 |
| Lattice Const. (Å) | 5.7012 | 5.6534 |
| Heavy-Hole Mass ($m_0$) | -.468 | -.450 |
| Light-Hole Mass ($m_0$) | -.075 | -.082 |
| Eff. Elec. Mass ($m_0$) | .062 | .0667 |
| Hydrostatic Const. (eV) | -8.10 | -8.40 |
| Deformation Position (eV) | -1.71 | -1.70 |
| Valence Band (eV) | .0277 | .0000 |
| Conduction Band (eV) | 1.2714 | 1.4247 |
| Band Gap (eV) | 1.2437 | 1.4247 |

**Superlattice Layer parameters**

Fractional relaxation from substrate = .000

| | $Ga_{.882}In_{.118}As$ | GaAs |
|---|---|---|
| Stress ($10^{11}$ dyne/$cm^2$) | -.0974 | .0000 |
| Biaxial Strain | -.0084 | .0000 |
| Lattice Const. (Å) | 5.6534 | 5.6534 |
| Layer Thickness (Å) | 90.0 | 90.0 |
| Heavy-Hole Band (eV) | .0493 | .0000 |
| Light-Hole Band (eV) | -.0165 | .0000 |
| Conduction Band (eV) | 1.3272 | 1.4247 |

**Wavefunction Solution Energies**

| Solution # | Heavy-Hole (eV) | Light-Hole (eV) | Conduction (eV) |
|---|---|---|---|
| 1 | .0433 | -.0108 | 1.3563 |
| 2 | .0262 | | |
| 3 | .0028 | | |

Assuming 8 meV binding energy, the lowest energy exciton is at 9501.1 nm.

## 2.5 Processing of Samples for Transverse Spectral Measurements

The method of processing patterned contacts onto the samples, and then cleaving the individual diodes will be explained. A wafer portion 0.5 cm by over 1.0 cm in size was fixed to a polishing block with crystal bond, and was thinned on 600 grit sandpaper to about 150-200 $\mu$m thickness. Most sample backs were then polished with 6$\mu$m and 1$\mu$m grit diamond compound against a polishing cloth. After cleaning the sample in acetone, methanol, and water, the sample was fixed to a clean glass cover slip substrate side up, to allow easier handling during processing. It was important to make sure the crystal bond was only under the sample, and not flowing out onto the rest of the cover slip, or it may have contaminated the photoresist.

A lift-off technique was used to pattern the contacts. The back contact pattern was all metal, except for a 1.25mm by 2.75mm rectangular hole for light to pass through. The sample was placed on a spinner, three drops of photoresist were applied, and sample was spun at 4000 rpm. for 30 seconds. The sample was then placed in a pre-heated oven at 85C for 10 minutes. The photoresist was then exposed to the contact pattern in the mask aligner for 20 seconds (longer than usual). The sample was then submerged in toluene for 10 minutes with no agitation. After rinsing in de-ionized water, the sample was developed in the recommended 1:5 developer:water mixture for 1 minute 15 seconds (longer than usual). The toluene hardens the top of the photoresist, slowing developing and promoting undercutting during development. This is important in a lift-off technique. After rinsing and drying, the sample was placed in an ultra-violet ozone cleaner for 3 minutes, followed by 30 seconds dip in a 5% HCl solution.

After rinsing and drying, the sample was placed in an electron-beam evaporation chamber. After a pressure of $5x10^{-6}$ torr was reached, 200Å of Ge and

400Å of Au were deposited on the back surface. After removal from the chamber, the sample was placed in acetone, and a stream of acetone was directed on the sample. After a couple of minutes, most or all of the photoresist was removed, lifting off unwanted metal with it. If there was still some photoresist left, the sample was placed in hot photoresist stripper for about 20 minutes, followed by direct acetone spray. The sample was then rinsed in methanol and de-ionized water. After removal from the cover slip (using heat, followed by acetone, methanol, water), the sample was then placed in a large carbon boat, and annealed at 400C for 20 seconds. This melted the gold-germanium eutectic, and allowed diffusion of metal into the substrate, making a good contact. On smooth-back samples, some 'balling up' of the metal was noted, with the surface texture no longer smooth.

The process is then repeated for the gold contact on the front side. There are only a few differences. The front metal pattern is a ring the same size as the back-pattern hole, but with a ring thickness ranging from 150$\mu$m on the ends to 75$\mu$m on the sides. The other main difference is that about 500Å of only Au is used for the contact, and it was not annealed. The lack of anneal was to prevent gold from finding its way into the active region of the device. A gold wire-bond made contact to the front side of the device, while silver paint made contact to the back metal. Slab waveguide samples were simply pieces of these larger samples cleaved shorter. The processing of rib-waveguide samples will be explained in later chapters.

## 2.6 Current vs. Voltage Curves

One can easily check the electrical properties of the processed diode samples by looking at the current vs. voltage (I-V) relationship. In forward bias, one would expect to get many milliamps of current with voltages approaching the value of the

bandgap. This was in fact seen. To ensure that the reverse-bias voltage is indeed causing an increasing field in the samples, one would expect the reverse-bias current to be low. A straight resistor-like I-V curve would indicate a damaged diode. It is important that the total leakage current, multiplied by any sheet resistances and contact resistances are lower than a fraction of a volt. The sheet resistivity of growth 'A' theoretically should be less than 2kΩ /square, while the sheet resistivity of growths B and C should be about 300Ω /square. This is sufficiently small given the observed leakage. The I-V characteristics of the samples processed for transverse electro-absorption measurements are shown in Figure 2.7

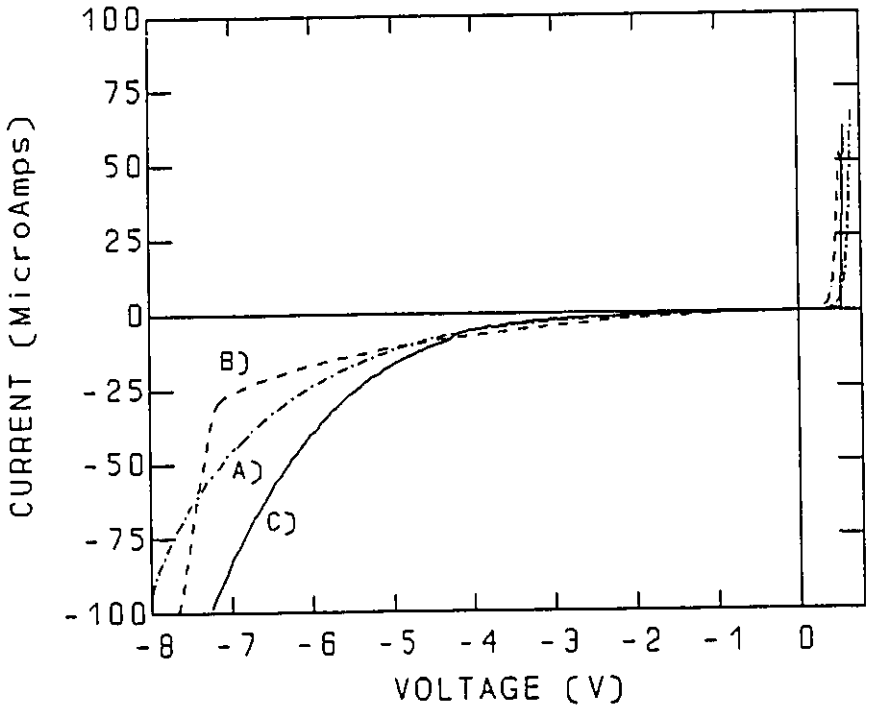


**Figure 2.7** Current vs. Voltage relationships for approx. 2mm x 3mm samples of materials A, B, and C. The reverse-bias leakage current is larger than one would like, but is small enough to not affect electro-absorption results.

All these material samples showed reverse-bias breakdown at about -8V to

-9V. The sharpness of the breakdown knee varied from sample to sample. When 20$\mu$m-wide rib waveguide modulators were processed from these materials, the reverse-bias leakage current changed considerably. An I-V curve for a rib waveguide processed from material B is shown in Figure 2.7. With an area reduced by several hundred times, the magnitude of the leakage also dropped by a similar factor. It was noticed, however, that for a rib from material A, the magnitude of the reverse-bias breakdown voltage increased to more than 15V. This corresponds to a field of about $2x10^7$ V/m. The change suggests that the reverse-bias breakdown voltage in larger samples of material A may have been limited by leakage paths through a small number of bad defects. With a much smaller area rib, there would be less chance of one of these defects being present.

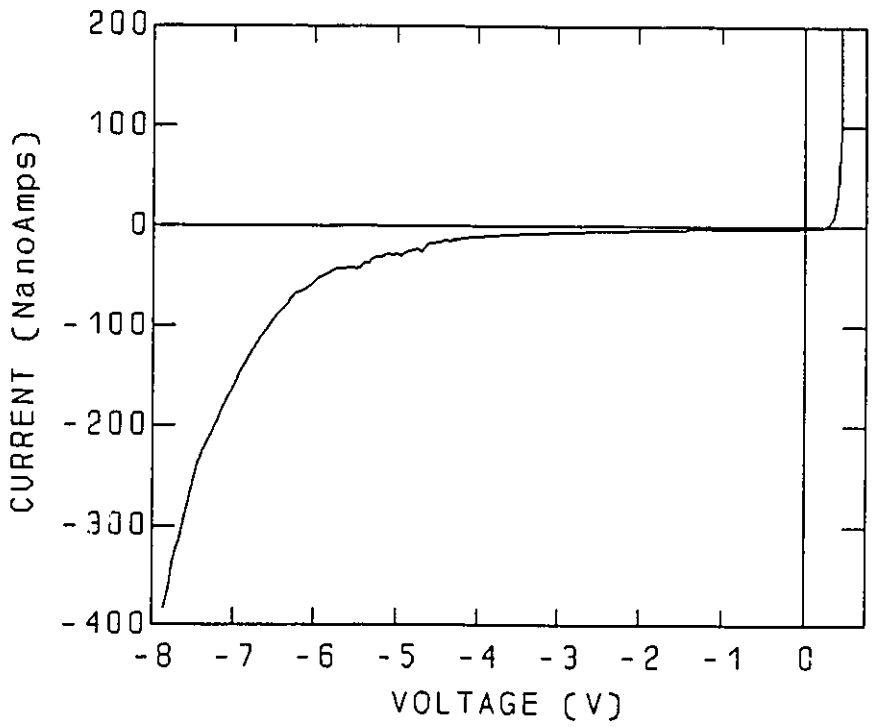


**Figure 2.8** The current vs. voltage relationship for a 20$\mu$m-wide, 900$\mu$m-long rib waveguide modulator grown processed from material B. A sharp reverse-bias breakdown is seen at -8.5V, but otherwise the reverse leakage is very low.

# CHAPTER 3

## Experimental Transverse Electro-Absorption

### 3.1 Introduction

The shape of the quantum-well absorption near the band edge can be easily measured using transverse spectroscopy techniques. By polishing the back of a sample, and by shining light through the front side of the sample, transmission and photocurrent spectra can be taken for different sample biases. The short interaction distance for the light passing through the quantum wells results in only a small absorption. This is an advantage for seeing the shape of the absorption spectrum at photon energies greater than just the extreme band edge. It is a disadvantage, however, in terms of signal-to-noise and in terms of comparing small changes in transmission for various biases. To more accurately measure transmission (and therefore absorption) changes, a transmission modulation technique is also used. The resulting families of curves can be used to both quantitatively and qualitatively examine the band-edge electro-absorption in our $In_xGa_{1-x}As$-GaAs Multiple Quantum Well (MQW) samples.

### 3.2 Experimental Apparatus

In these transverse spectral measurements, two different tunable light sources were used. For the majority of the work, a monochromated white light source was used. Light from a 55 Watt Tungsten-Halogen lamp was focused into a 0.5 metre

Jarrell-Ash monochromator. A 590 lines/mm grating, blazed at 750nm, combined with 100$\mu$m slits provided approximately 3nW of power in a 0.7nm bandwidth. The source spectrum was stable from 900nm to 1010nm to within 0.1% per hour, after a 2-hour warm up. During warm up, the intensities can change by as much as 10%. For most spectra, the optics were boxed, and dry air was allowed to flow into the boxes and monochromator to eliminate optical absorption by water vapour lines situated at 930nm-960nm. This flow rate must be kept constant to ensure a constant source spectrum. The internal monochromator motor was used to vary the source spectrum, and a Metrabyte DAS-8 card was used to digitize the desired signals. A diagram of the basic optical set-up is given if Fig. 3.1. The signals which must be amplified for the various types of spectral measurements will be given later in this section.

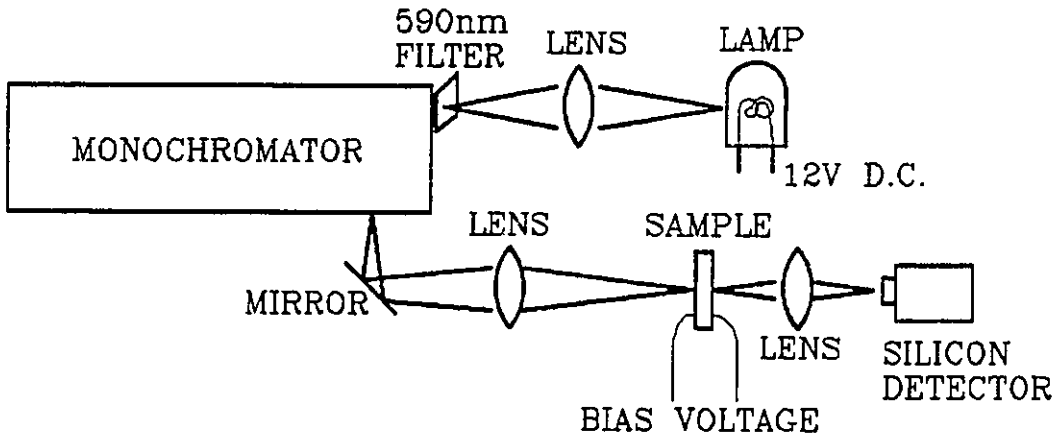


**Figure 3.1** Optical set-up for transmission, photocurrent, and transmission modulation spectra. Choppers and electronics are not shown, as they vary for the different measurements.

For the case of photocurrent spectra, where the photo-generated carriers are amplified and measured, the reverse-bias leakage current through the sample will

swamp the photocurrent for voltages more negative than -2V. In this case, the experiment was temporarily transported to the Ontario Laser and Lightwave Research Centre, and a Titanium-Sapphire laser was used as a light source. The experimental set-up is given in Fig. 3.2.

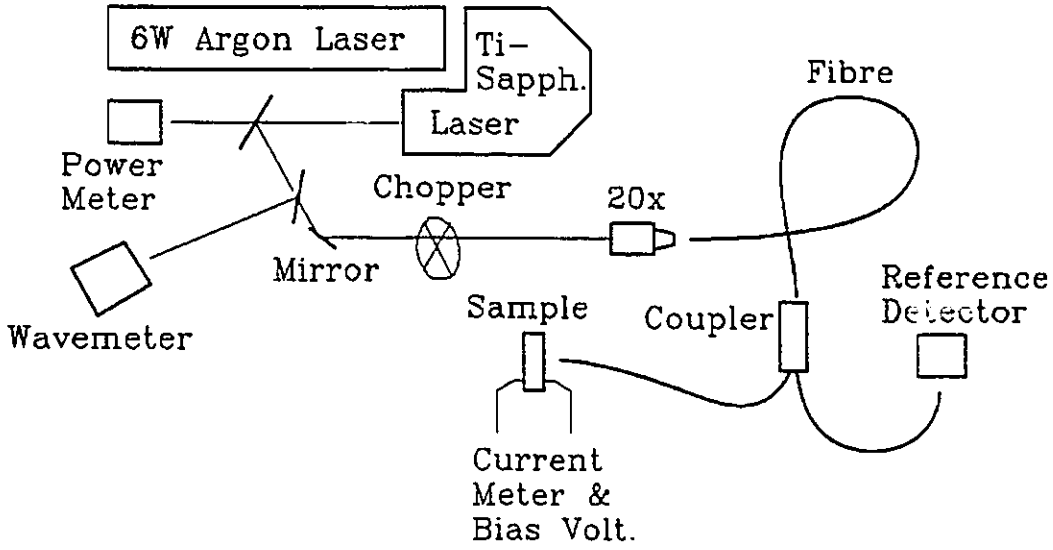


**Figure 3.2** The experimental set-up for measuring photocurrent at various reverse-bias voltages using a Ti-Sapphire laser source. Lock-in amplifiers are used for the reference detector and the photocurrent signals.

The laser light was delivered to one input of a 2x2 fibre coupler with a 50% splitting wavelength of 850nm. The coupler then split the light into two parts, one to the sample and the other to a reference detector. Once the splitting ratios are calibrated for the various wavelengths (using identical detectors at the output fibre ends), the reference detector can be used to measure the intensity of the light source at all times. By dividing by this reference signal (after computer acquisition of both signals), photocurrent spectra can be corrected for changes in source intensity with time, and with wavelength. A current-to-voltage converter, with a 5kΩ amplifying

resistor was used to detect the photocurrent. Lock-in amplifiers were used for both signals, with 0.3 sec. time constants. Unfortunately the two lock-ins did not have identical filter responses, so 20 seconds of computer integration of the signals was performed to minimize the considerable laser noise. Since the wavelength was scanned manually, this long wait between points was necessary anyway. Between each point, a micrometer on the Ti-Sapphire laser was varied to tune the wavelength to a 1nm increment. There was some inaccuracy in the positioning since the wavemeter display only had 0.3nm resolution.

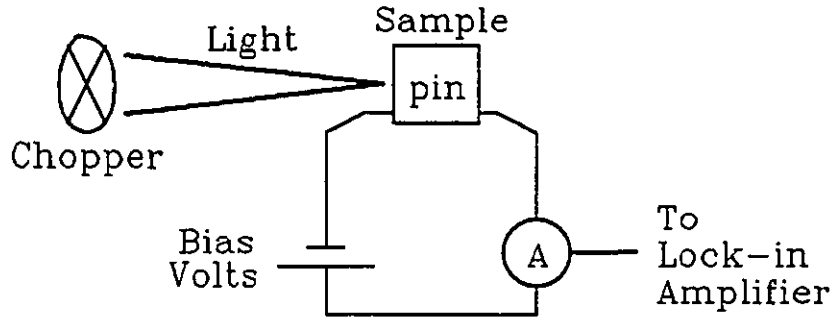


**Figure 3.3** The set-up for photocurrent measurements. The circle labelled 'A' is an ammeter, or more specifically a current to voltage converter. The output goes to a lock-in to isolate the photocurrent from leakage.

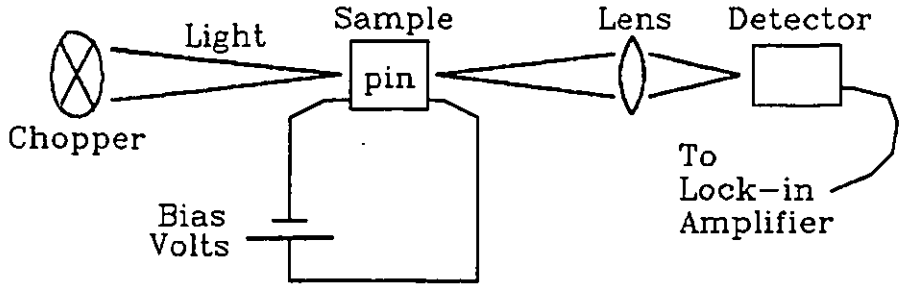


**Figure 3.4** The set-up for transmission measurements. Light is incident transverse to the sample, as with the other measurements in this chapter. A lock-in amplifier was used to minimize noise and any electronic or optical offsets.

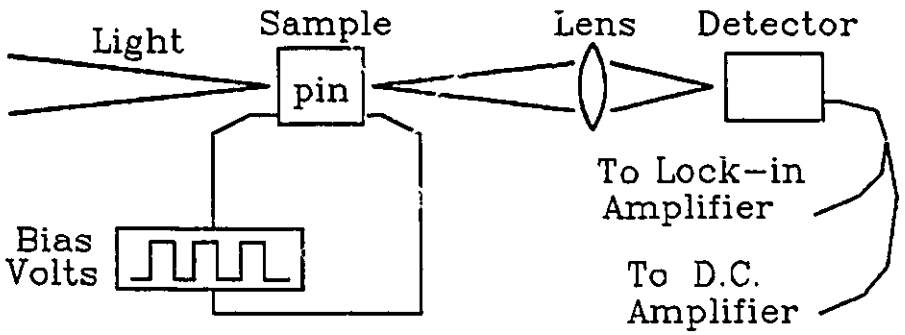


**Figure 3.5** The set-up for measurement of transmission modulation spectra. The bias voltage is modulated with a square wave, and the transmission change is measured with a lock-in amplifier. The average D.C. transmission is measured.

A comparison between the photocurrent, transmission, and transmission modulation measurements is given in Figures 3.3-3.5. For photocurrent measurements, the current through the current-to-voltage converter was sent to a lock-in amplifier which was referenced to the light chopping frequency of about 100 Hz. For the light transmission spectra, the output of a silicon photo-detector, converted to a voltage by a 20MΩ resistor and op-amp, was sent to the lock-in amplifier. Again the lock-in was referenced to the light chopping frequency For the transmission modulation spectra, the bias voltage was set to a square wave (at 100 Hz) from 0V to some test voltage (forward or reverse bias). The lock-in amplifier was used to amplify the detected signal at the reference frequency of the bias modulation. Therefore it is the difference between the 0V and test-bias transmission spectra that was measured. Also measured simultaneously was the average D.C. transmission of the two biases. By taking this average D.C. transmission, and adding or subtracting the R.M.S. modulated signal on computer, one can reproduce the actual 0V-bias and test-bias transmission curves, with their differences registered very accurately. One must be careful that the detector response is much faster than the chopping frequency, and that the lock-in time constants are kept to a fraction of the

time between points, or the final curves will not accurately represent the proper shapes. Before or after a set of spectra are taken (and sometimes both), a system response spectrum was taken using the exact same optical set-up, but without the sample. In the case of photocurrent measurements, the sample is replaced with a silicon p-i-n photodetector. While the detectors have been calibrated approximately against a Photodyne power-meter, it was found that the response was fairly constant over the spectral ranges used, and therefore correction was not performed for detector responsivity. The circuits for the silicon detectors, and the current-to-voltage converter used to measure photocurrent are given in Appendix E, along with their expected noise performance.

## 3.3 Transverse Photocurrent Spectra

Photocurrent spectra are taken most easily at zero volts bias on the sample. At this voltage, only the photocurrent flows through the device, keeping noise to a minimum. In a perfect diode, the reverse-bias noise should actually be better, but for our non-ideal devices, there was considerable leakage current in reverse-bias, with a considerable amount of flicker noise, or 1/f noise associated with it. A zero-bias photocurrent spectrum for a sample of material A is given in Figure 3.6. This is a true zero-background spectral measurement, with zero photocurrent corresponding to zero absorption within the intrinsic region of the diode. The band-edge absorption shape is therefore measured accurately. Because of signal-to-noise problems in reverse-bias spectra, they are not displayed. A light-source with more power than the 3nW that we had available would be required for a better signal.

By using the Titanium-Sapphire laser to provide a large signal, photocurrent measurements were made at a variety of bias voltages for a sample from material B.

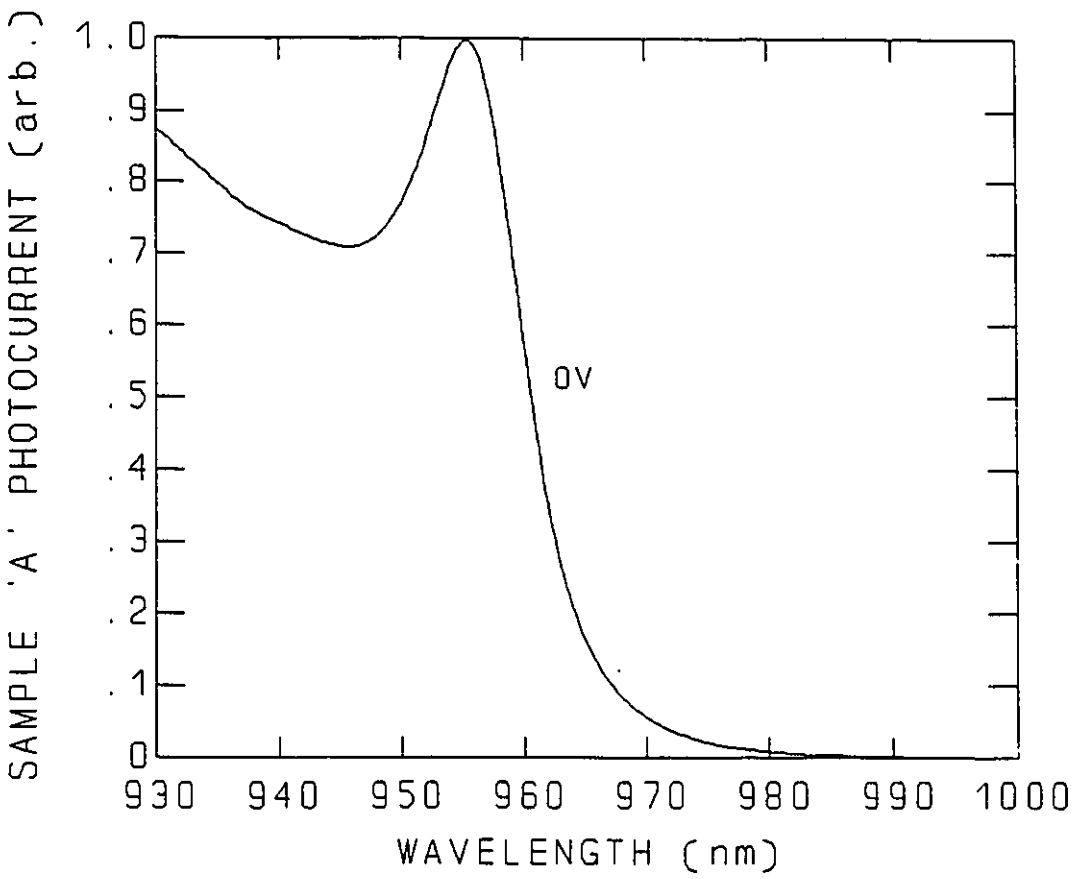


**Figure 3.6** Material 'A' photocurrent spectrum taken at 0 Volts bias. The height of the exciton peak is arbitrarily set at one.

The results are shown in Figure 3.7. The sharp exciton peak observed at 0.4V bias (low field) weakens, broadens, and shifts to longer wavelength as the reverse-bias voltage is increased (as the field is increased). While the shape of each individual curve is correct, one can not compare the absolute heights of the various curves due to variations in carrier collection efficiency with bias. The absorbed light produces electrons and holes, but these carriers must be accelerated by the electric field and be collected at the diode terminals before photocurrent is seen. There is evidence that the collection efficiency at -2V may be 15%-30% larger than at 0V bias. A 0.7V

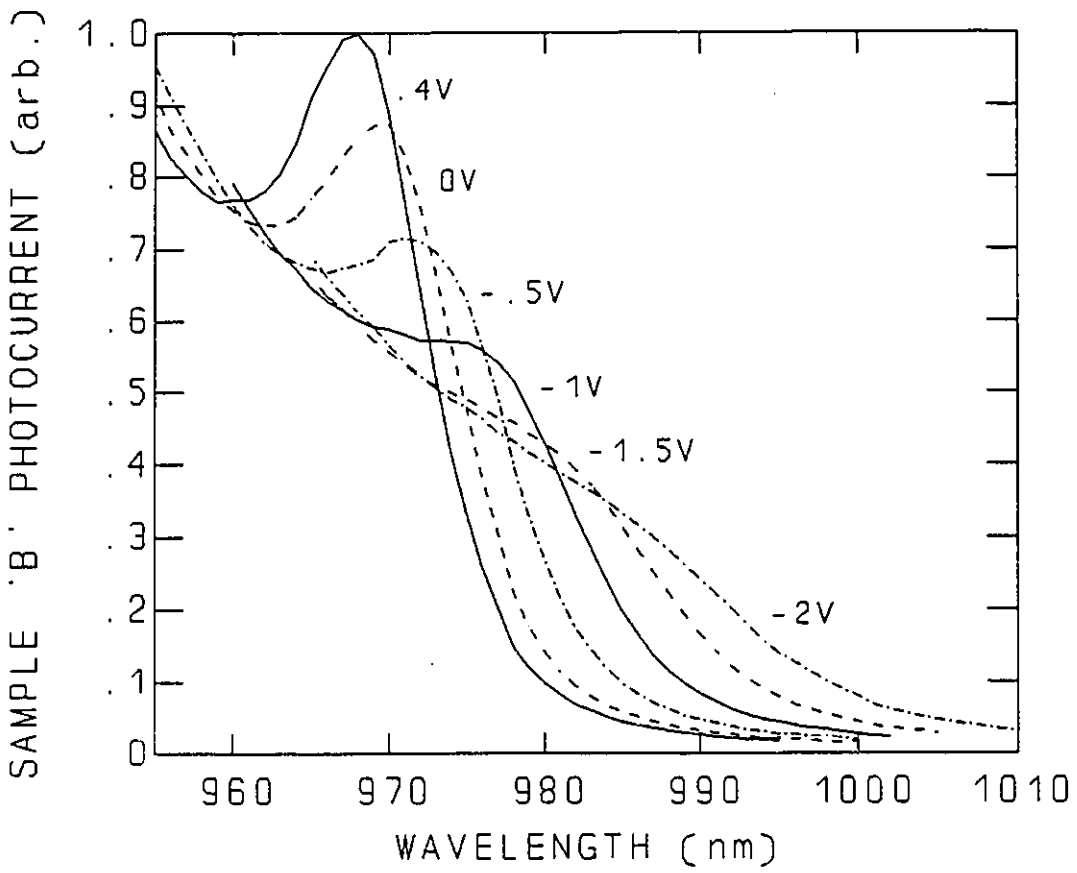


**Figure 3.7** Material 'B' photocurrent spectra for various bias voltages. The height of the 0.4V-bias exciton peak is arbitrarily set to one.

bias curve was also taken, but the peak height dropped by a factor of 1.8 compared to the expected absorption strength. This is understandable, since at this voltage, the forward-bias diffusion current is several hundred micro-amperes, and the electric-field is considerably weaker. Notice in these spectra that by -2V bias, the exciton feature is almost totally washed out, at a field of about $1.06 \times 10^7$ V/m. This broadening is due to a number of factors, the main one being lifetime broadening of the exciton due to field-induced ionization.

The photocurrent spectra of a sample of material 'C' is shown in Figure 3.8.

The exciton peak is sharp and clearly distinguishable at 0.8V bias, corresponding to a low internal electric field. By 0V-bias, the internal electric field rises to about

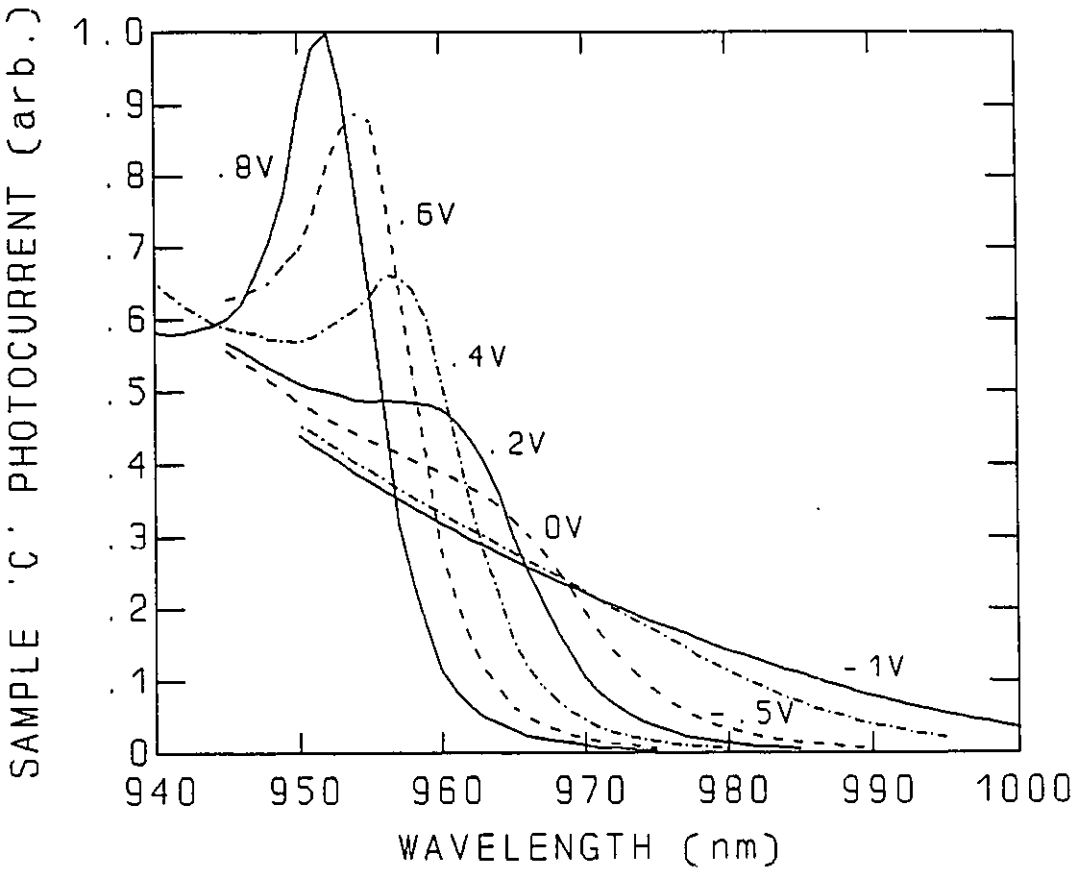


**Figure 3.8** Material 'C' photocurrent spectra for various bias voltages. The height of the 0.8V-bias exciton peak is arbitrarily set to one.

$9.4 \times 10^6$ V/m, and the exciton is considerably weakened and broadened. The high field is due to the thin intrinsic region. This growth would probably not be optimally designed for modulation using only negative voltages. Waveguiding modulation results, shown in later chapters, do indicate good performance for negative voltages only provided the wavelength of operation is long enough to provide transparency at 0V, and the waveguide has sufficient length to provide switching. The exciton peak

can no longer be seen by -1V, and the band-edge appeared much like that of a bulk material up to reverse-bias voltages of -8V.

## 3.4 Transverse Transmission Modulation Spectra

When taking transverse modulation spectra, the average D.C. transmission was recorded, as was the difference between transmission at the test bias and 0V-bias. Now, the transmission through the entire sample is going to be the incident light minus the absorbed light minus the reflected light. The maximum transmission seen

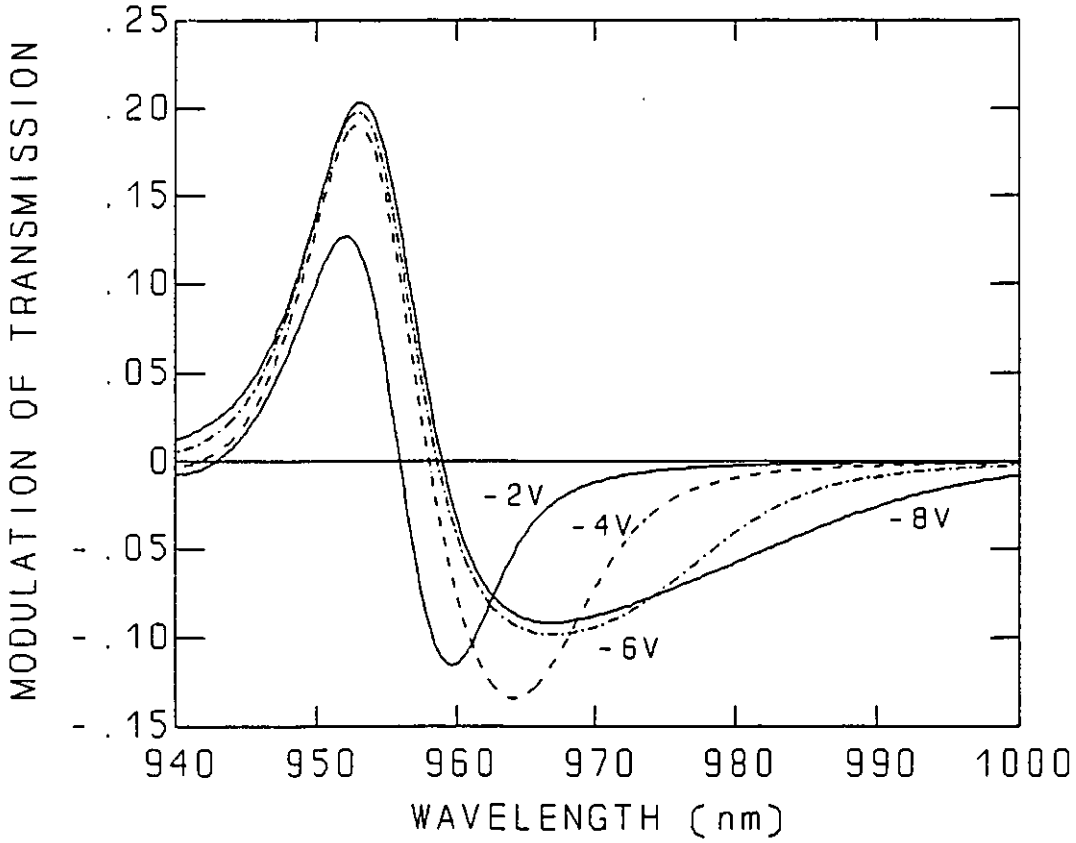


**Figure 3.9** Material 'A' transmission modulation spectra. These are calculated as the transmission at the bias-voltage indicated minus the transmission at 0V bias. An absolute transmission of one is defined as zero absorption.

in the samples is about .46±.02 of the incident intensity. For the purposes of the

following curves, however, I will define the transmission level at which zero absorption occurs in the epilayer (and therefore zero photocurrent is seen) as being equal to 1.0. Therefore the epilayer absorption plus the epilayer transmission is equal to one. To make analysis easier, we ignore the effects of multiple reflections within the sample. Because the absorption levels are low, multiple passes should not affect the spectral shapes, but may slightly effect the absolute absorption measured.

The transmission modulation spectra for material 'A' is given in Figure 3.9, with full transmission equal to one. While low voltages provide high transmission change at 965nm, which is close to the zero-bias band edge, higher voltages are

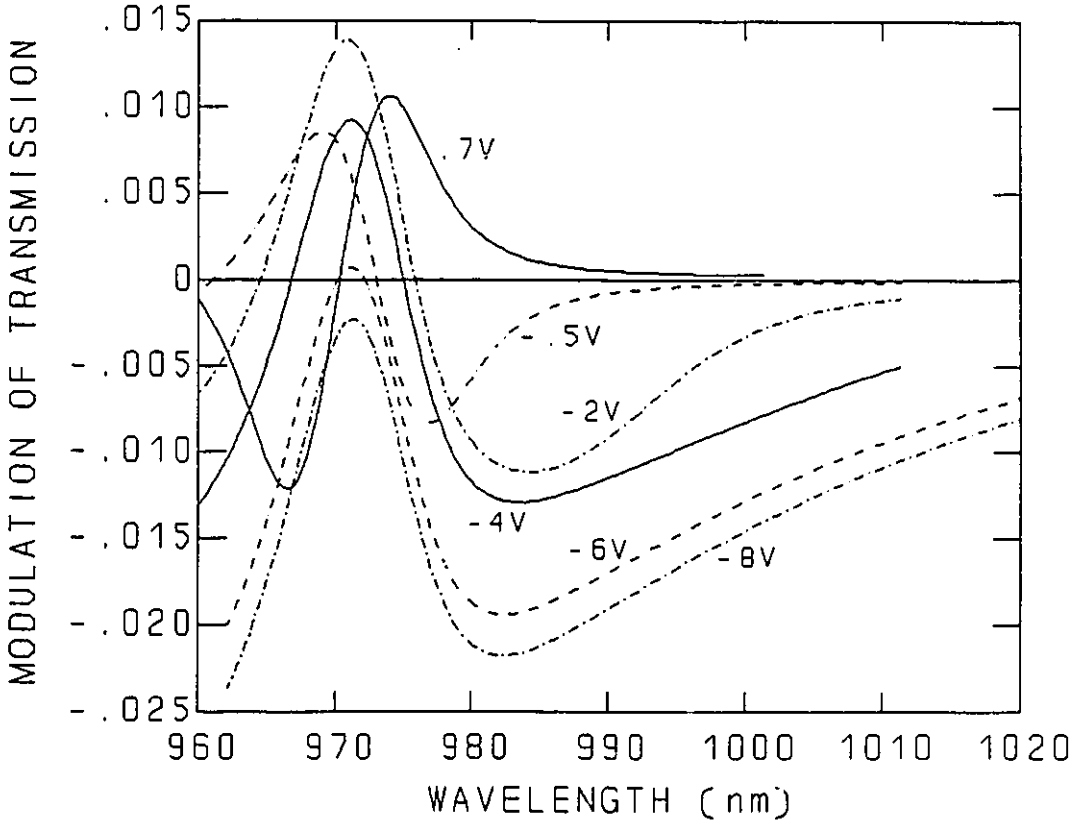


**Figure 3.10** Material 'B' transmission modulation spectra. These are calculated as the transmission at the bias-voltage indicated minus the transmission at 0V bias. An absolute transmission of one is defined as zero absorption.

required to create transmission changes at longer wavelengths. Rib waveguide samples of this material could be pushed to -15V bias, but the larger sample used could not due to high reverse-bias leakage currents.

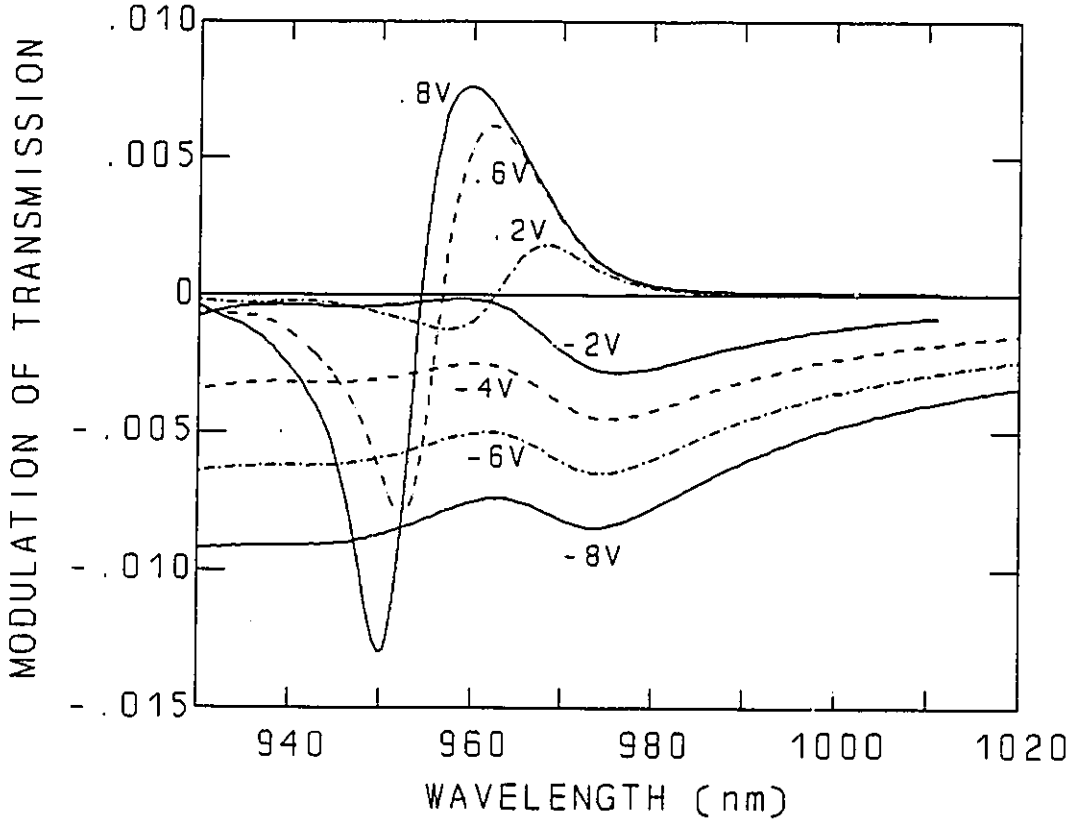


**Figure 3.11** Material 'C' transmission modulation spectra. These are calculated as the transmission at the bias-voltage indicated minus the transmission at 0V bias. An absolute transmission of one is defined as zero absorption.

The transmission modulation spectra for material 'B' are shown in Figure 3.10, and the spectra for material 'C' are shown in Figure 3.11. The magnitude of the modulation is low because materials B and C have only 5 and 3 wells respectively. The most important feature is the drop in transmission at longer wavelength with large reverse-bias voltages. The high applied fields result in a large shift and a large

broadening of the band edge, causing a strong absorption to occur at wavelengths where there was no absorption previously. This is advantageous for achieving switching ratios in modulators. In a practical device, however, one would usually want switching to occur at low fields, which allows the intrinsic region to be wider for a given switching voltage. This reduces the device capacitance, and increases speed. Alternatively, lower fields would allow smaller operating voltages to be used.

## 3.5 Final Transmission and Absorption Spectra

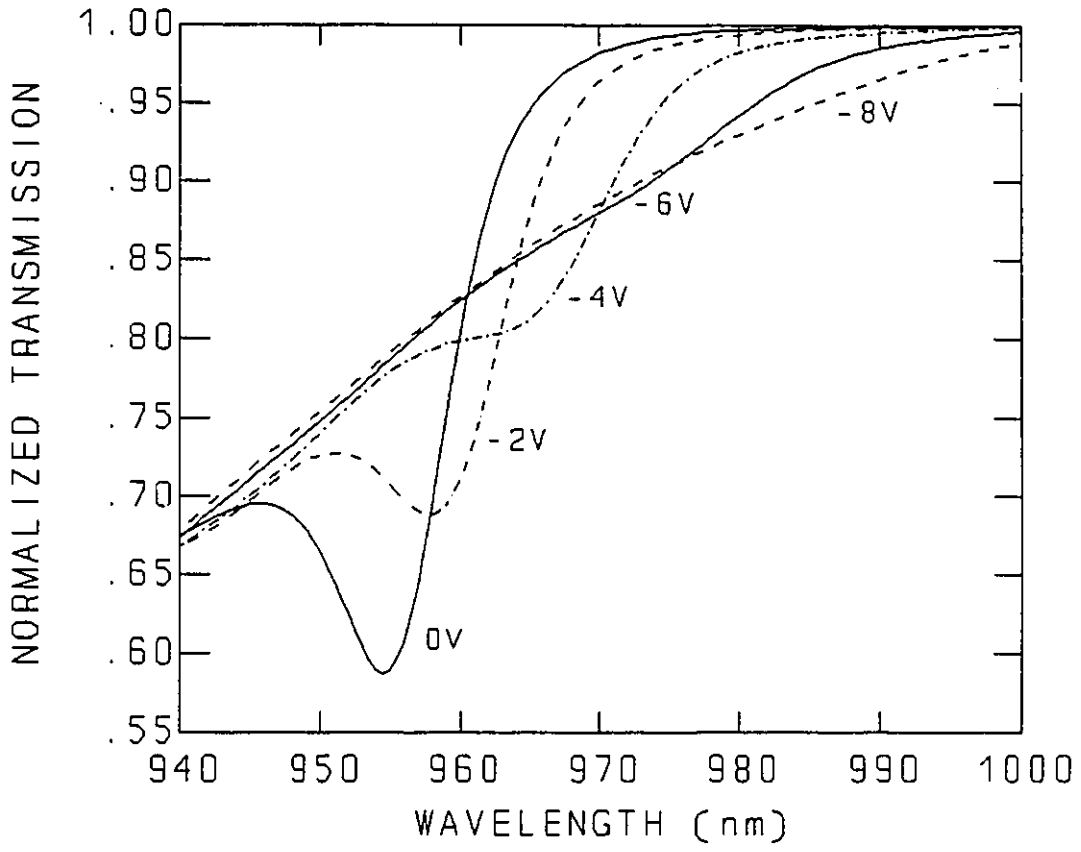


**Figure 3.12** Material 'A' transmission spectra for various bias voltages. These are direct transmission measurements, with the 100% transmission line determined using the zero-bias photocurrent spectrum.

A set of transverse transmission spectra at various biases is a good way of displaying the band-edge absorption changes with electric field. Waveguiding transmission would only display the changes far into the band tail, since even small absorption coefficients result in total absorption. The transverse spectra give more information about the changes in strength, position, and width of the band-edge exciton.

The transverse transmission spectra for material 'A' are shown in Figure 3.12. The absorption plus transmission is equal to one. These spectra are direct transmission curves, with the 100% line determined from comparison with the 0V-bias photocurrent spectra. To compensate for small changes in the lamp spectrum between curves (taken 20 minutes apart), the modulation spectra have been used to individually scale the spectral heights. This ensures an accurate spectrum at longer wavelengths, where the transmission is almost equal to one. The zero-bias exciton peak is quite sharp, resulting in a small amount of absorption to longer wavelength than 970nm. The peak shifts, broadens, and weakens with applied reverse bias, and it is clear that the absorption coefficient increases by many times over a long wavelength range. A high ratio of absorption coefficients between high and low bias (coupled with an appropriate length modulator for the absorption strengths involved) is the necessary condition for a high switching ratio with low loss. If the absorption changes occur at a wavelength with high absolute absorption coefficients, the modulator must be kept short (which is good for speed) to reduce transmission losses. A high absorption coefficient ratio at a longer wavelength, where there is a small absolute absorption coefficient, means that the modulator must be longer to provide enough interaction length for switching. The absorption coefficient at the peak of the 0V-bias exciton feature is about 6800 $cm^{-1}$.

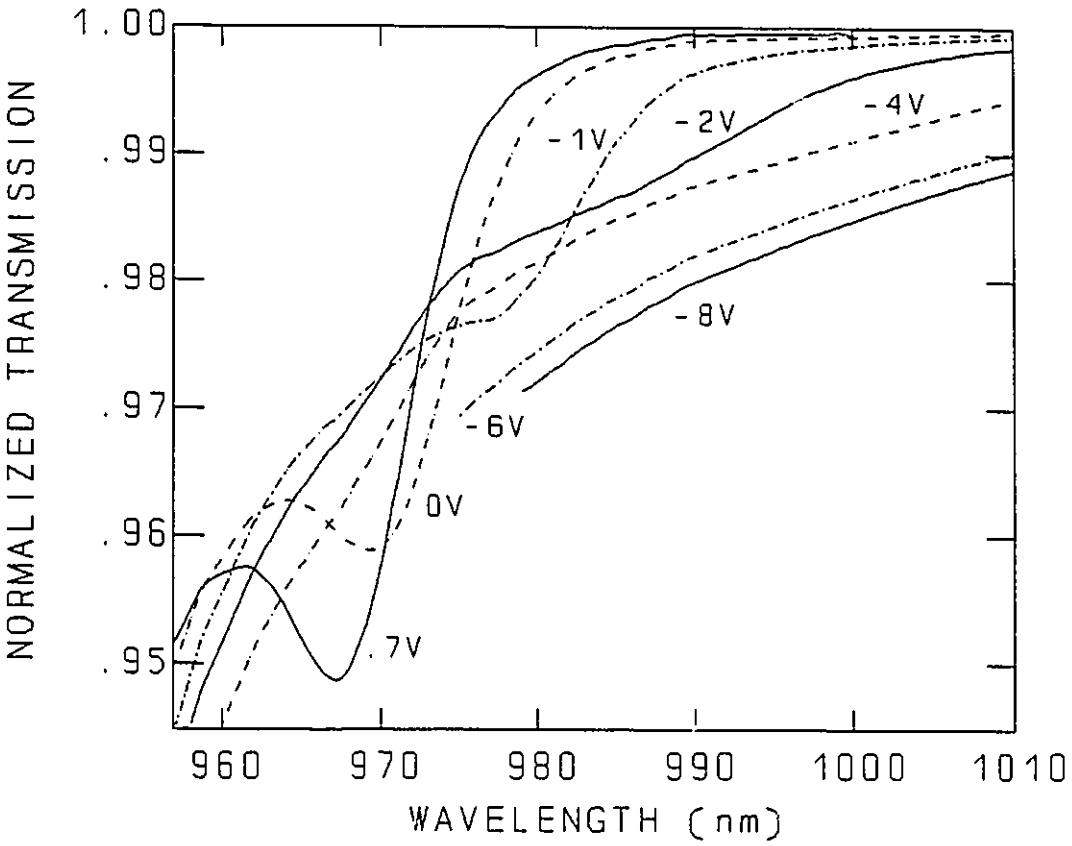


**Figure 3.13** Material 'B' transmission spectra for various bias voltages. Transmission plus absorption is defined as being 1.0. The spectra are built up from transmission modulation measurements.

The absorption spectra for materials 'B' and 'C' are given in Figures 3.13 and 3.14 respectively. To obtain these from the transmission modulation data, a 0V-bias transmission curve is found first. For material B, this was accomplished by subtracting half of the peak -0.5V vs. 0V modulation data from the average D.C. transmission seen for the two biases. For material C, the 0.2V vs. 0V modulation data and average D.C. transmission were used. Now, the peak modulation spectra for various biases was added to these 0V-bias curves to produce a family of curves. The low-field photocurrent data were then used to determine a 100% line for the

transmission. By dividing all curves by this line, the normalized transmission spectra are produced for any one material. The longest wavelength portion of the lowest-field (forward-bias) curve has been forced to a value of 1.0 (and the other curves altered accordingly), since it would wander slightly from this 100% line. This results in the most correct depiction of the long-wavelength quantum-well transmission.

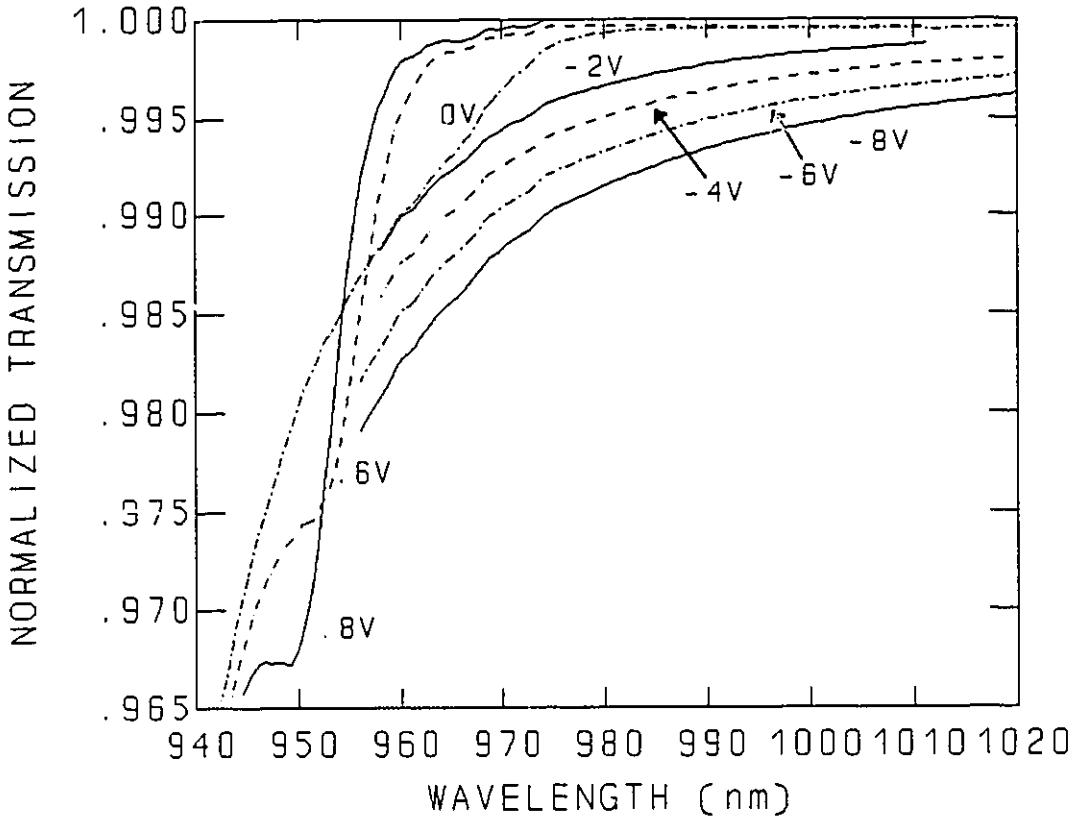


**Figure 3.14** Material 'C' transmission spectra for various bias voltages. Transmission plus absorption is defined as being 1.0. The spectra are built up from transmission modulation measurements.

The thin intrinsic regions in growths B and C result in high fields even at 0V bias. That is why the forward-bias transmission is much sharper than it is at 0V bias. For ideal switching, one would therefore operate the modulator at forward bias in the 'on' state, and reverse-bias in the 'off' state. However, it may not be practical in

a commercial device to use a bipolar power supply for switching. In fact, these modulators will give good switching with just negative voltages. Operation of these diodes at high fields results in large absorption coefficient ratios between reverse-bias and 0-bias absorption at longer wavelengths. The absorption coefficient at the 0.7V exciton peak in material B is about 5800 $cm^{-1}$. The absorption coefficient at the 0.8V exciton peak in material C is about 6200 $cm^{-1}$.

## 3.6 Discussion

The spectra shown in this chapter are sufficient to determine the expected performance and wavelengths of operation of a waveguide modulator processed from these three growths. More important for determining the factors limiting modulator performance is to determine why the band edge behaves as it does. The next step in this work is to attempt to model the band-edge electro-absorption. That is, one should try to determine the reasons behind the quantity of exciton wavelength shift, weakening, and broadening. If this can be done well, one will have a tool for theoretically predicting modulator performance. If theory does not match experiment closely enough to predict performance, at least it will provide qualitative answers as to what structural parameters contribute to good switching ratios, low losses, and modulator frequency. Although speed measurements are not made in this thesis, one can still qualitatively argue the requirements for high speed operation. Developing a quantitative theory for band-edge changes with field is an interesting problem in itself, which can be applied to other quantum-well devices and structures, and which has not been adequately solved by others.

# CHAPTER 4

# Multiple-Quantum-Well Energy Solution Methods.

## 4.1 Introduction

The first step in calculating the band-edge changes with electric field is to calculate the shifts of the quantum-well energies with field. Shown here is a method for calculating the energy solutions and wavefunctions for the bottom of an electron energy sub-band (where $k_{\|} = 0$) in the envelope-function approximation. With this method, the electron energies and wavefunctions can be solved for in any semiconductor multiple quantum-well structure with a non-zero applied electric field. Hole wavefunctions can likewise be derived by flipping over the hole band. This method, therefore assumes that the conduction and valence bands are uncoupled, which is correct for the large bandgap III-V materials used in this investigation. The effects of the Coulomb potential between electrons and holes is ignored at this stage. The calculation solves the one-dimensional energy solutions for the z-direction (perpendicular to the lattice planes). We compare the results with and without conduction-band non-parabolicity for three different solution methods.

## 4.2 Case 1: Calculations Involving Parabolic Bands

The Schrodinger equation for an electron with a wavefunction $\psi$ and an energy $E$ (defined at $z=0$) in an electric field is

$$-\frac{\hbar^2}{2m^*(z)}\frac{\partial^2\psi}{\partial z^2} + [V(z)+eFz]\psi = E\psi \qquad [4.1]$$

Here $V(z)$ is the electron potential energy for zero-field, $F$ is the electric field in the $z$-direction, and $e$ is the magnitude of the electron charge. This equation can be re-written as

$$\frac{\partial^2\psi}{\partial z^2} - \frac{2m^*(z)}{\hbar^2}[V(z)+eFz-E]\psi = 0 \qquad [4.2]$$

Let the energy assume complex values under some circumstances. We can define the energy $E$ in terms of the real component $E_R$ and the imaginary component $E_I$ as follows,

$$E = E_R + iE_I \;,\; i=\sqrt{-1} \qquad [4.3]$$

We will first consider the case of parabolic bands, where the effective mass is constant in any one material type. Let the structure contain $s$ material layers. The region consisting of material layer $n$ ($n \in \{1..s\}$) is now considered where the zero-field potential is a constant, or $V(z)=V_n$. We define $K_n$ as being the kinetic energy in layer $n$:

$$K_n(z) = E_R - V_n - eFz \qquad [4.4]$$

We now define the effective mass in layer $n$ as $m^*(z)=m^*_n$. Now, define the variable $Z_n$ in region $n$ such that

$$Z_n = \left[\frac{2m_n^*}{(e\hbar F)^2}\right]^{\frac{1}{3}}(-K_n - iE_I) \qquad [4.5]$$

Equation 4.2 then becomes, for a structure consisting of $s$ materials,

$$\frac{\partial^2 \psi_n}{\partial Z_n^{\,2}} - Z_n \psi_n = 0 \ , \ n \in \{1..s\} \qquad [4.6]$$

This is the Airy differential equation, the solutions of which are linear combinations of $\mathrm{Ai}(Z_n)$ and $\mathrm{Bi}(Z_n)$: the Airy and Bairy functions [Abramowitz, 1964]. The wavefunctions solutions within each region can be written as:

$$\psi_n(z) = C_n \ \mathrm{Ai}(Z_n(K_n(z))) + D_n \ \mathrm{Bi}(Z_n(K_n(z))) \ , \ n \in \{1..s\} \qquad [4.7]$$

Graphs of the Airy and Bairy functions, along with a method for calculating them are given in Appendix C. The functions are oscillatory for positive kinetic energy and either monotonically decreasing or increasing for negative kinetic energy.

## 4.3 Case 2: First Order Band Non-Parabolicity

Now consider a second case, where we assume first order band-nonparabolicity, meaning that the effective mass is a linear function of positive kinetic energy.

$$m_n^*(K_n(z)) = \begin{cases} a_n K_n + b_n \ , \ K_n > 0 \\ b_n \ , \ K_n \le 0 \end{cases} \qquad [4.8]$$

The Schrodinger equation is the same as case 1 for negative kinetic energy. For positive kinetic energy, however, the Schrodinger equation becomes:

$$-\frac{\hbar^2}{2(a_n(E_R - V_n - eFz) + b_n)} \frac{\partial^2 \psi}{\partial z^2} - (E_R + iE_I - V_n - eFz)\psi = 0 \qquad [4.9]$$

To make the mathematics easier, some substitutions will be made:

$$X_n = \frac{\sqrt[4]{2a}}{\sqrt{\hbar|eF|}}\left(K_n + \frac{ia_nE_l + b_n}{2a_n}\right) \qquad [4.10]$$

$$\epsilon_n = \frac{\sqrt{2}(b_n - ia_nE_l)^2}{4\hbar|eF|\sqrt{a_n^3}} \qquad [4.11]$$

The Schrodinger equation then becomes,

$$\frac{\partial^2\psi_n}{\partial X_n^2} + (X_n^2 - \epsilon_n)\psi_n = 0\ ,\ K_n > 0 \qquad [4.12]$$

The solution to this equation is a linear combination of parabolic cylinder functions $W$ [Abramowitz, 1964]:

$$\psi_n = R_n W(\sqrt{2}X_n, \frac{\epsilon_n}{2}) + S_n W(-\sqrt{2}X_n, \frac{\epsilon_n}{2}) \qquad [4.13]$$

However it turns out that these functions are difficult to evaluate in the region of interest (small positive $K_n$). Also, one needs to join the equations to the Airy and Bairy functions for negative $K_n$. As shown in Appendix D, then, we define solutions $A_n^W$ and $B_n^W$ which smoothly become Ai and Bi at $K_n \leq 0$. They are evaluated using series solutions, joined for different ranges. The solution to the Schrodinger equation then becomes:

$$\psi_n(z) = C_n A_n^W(K_n(z)) + D_n B_n^W(K_n(z)) \qquad [4.14]$$

## 4.4 Three Solution Methods

The continuity conditions at the interface $z = z_{n-1|n}$ between materials *n-1* and *n* are:

$$\psi_{n-1}(z_{n-1|n}) = \psi_n(z_{n-1|n}) \ , \ n \in \{2..s\} \qquad [4.15]$$

$$\frac{1}{m^*_{n-1}} \frac{\partial \psi_{n-1}}{\partial z}\Big|_{z=z_{n-1|n}} = \frac{1}{m^*_n} \frac{\partial \psi_n}{\partial z}\Big|_{z=z_{n-1|n}} \ , \ n \in \{2..s\} \qquad [4.16]$$

This gives (*2s-2*) equations, but the coefficients $C_n$ and $D_n$ constitute *2s* unknowns. The boundary conditions at plus and minus infinity give the other two equations.

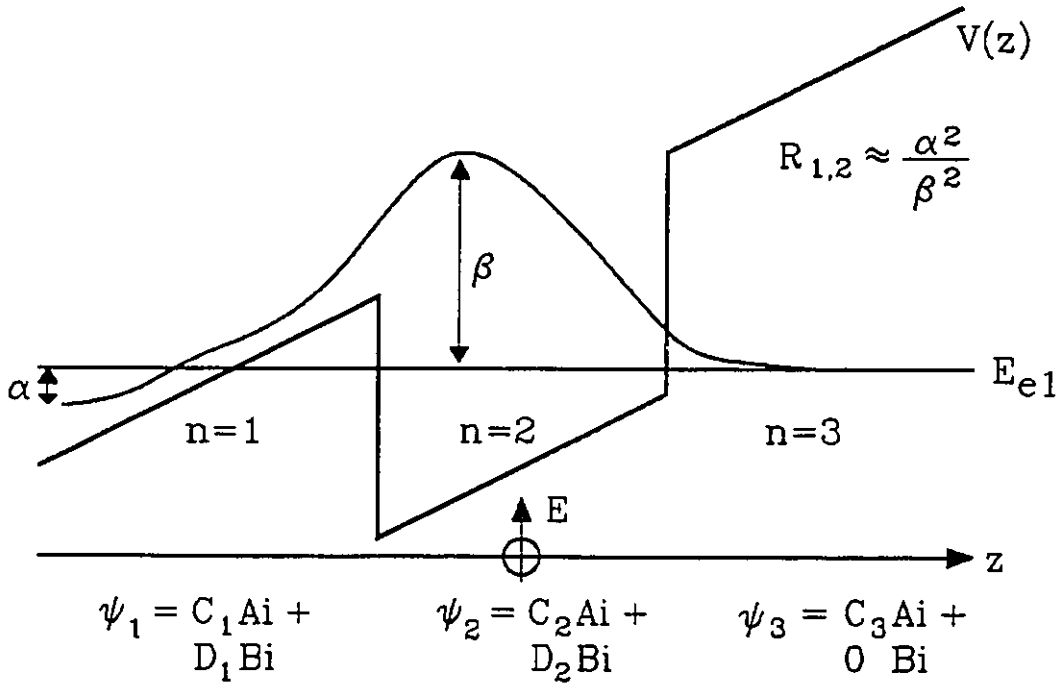


**Figure 4.1** A typical energy and wavefunction solution for a single well structure. Also shown are the wavefunction formulas for parabolic bands, and the value *R* used in the resonant tunnelling solution method.

In this chapter we compare three different sets of boundary conditions which will give slightly different eigen-energies. For all methods, however, the wavefunction must decay in the forbidden energy region. So, if one enumerates the layers such that the forbidden potential region is layer *s*, and that the energy continuum is layer *1*, then one can say,

$$\psi|_{z=\infty}=0, \text{ or } D_s=0 \qquad [4.17]$$

The first solution method is a complex-energy method which requires the use of complex mathematics for all coefficients and energies. A negative imaginary part to the eigen-energy means that the wavefunction is decaying due to tunnelling from the well. In fact, the lifetime $\tau$ is given by,

$$\text{If } E = E_R + iE_I \text{ , then } \tau = -\frac{\hbar}{2E_I} \qquad [4.18]$$

The boundary condition in region *1* (the energy continuum) is that the wavefunction should consist only of an outgoing wave. This means,

$$C_1 = iD_1 \text{ , } i=\sqrt{-1} \qquad [4.19]$$

The second solution method is a resonant-tunnelling method [Ghatak 1988], which ensures that the probability of the wavefunction being in the continuum as compared to one of the quantum-wells be a local minimum. Real energies and coefficients are used. This gives us the following boundary condition [Hunt, 1991a][Ghatak, 1990]:

$$\underline{\text{minimize}}\left(R_{1,n}(E)=\frac{C_1^2+D_1^2}{C_n^2+D_n^2}\right) \text{ , } n \text{ is a potential well} \qquad [4.20]$$

An energy width $\Delta E_p$ around an energy solution $E_p$ can be defined by the following equation:

$$\lim_{E \to E_p}\left(\frac{1}{R_{1,n}(E)}\right) = \frac{1}{1+\dfrac{4(E-E_p)^2}{\Delta E_p^{\,2}}} \qquad [4.21]$$

The shape of the probability resonance $1/R_{1,n}(E)$ around $E_p$ is a Lorentzian. One can fit a parabola to $R_{1,n}(E)$ at three energy values $E$ around $E_p$, and therefore determine $\Delta E$.

The third solution method is a discrete-energy solution method using only real energies and coefficients [Ghatak, 1990][Hunt, 1991a]. It gives good results for low fields where the wavefunction tunnelling to the continuum is small, but should be considered as an approximation for higher fields [Hunt, 1991b]. The boundary condition is:

$$C_k = 0,\ k \text{ is the first layer where } K_k(z_{k|k+1}) < 0 \qquad [4.22]$$

This means that for the first layer where the energy level $E$ is not totally above the potential barriers, one sets the wavefunction only equal to a multiple of the Bi (or $B_n^{\,w}$) function.

This gives enough information to solve for the energy solutions and their non-normalized wavefunctions. To solve the equations, we have used a single matrix of size $2s$ for each energy trial. The columns of the matrix correspond to the unknown coefficients $(C_1,D_1,...,C_s,D_s)$. Because this matrix is usually reasonably small, no special memory storage is needed. Because the non-zero elements are situated near the diagonal, it could be stored in a reduced space. This matrix structure also allows one to use a naive Gaussian elimination procedure of linear order to reduce the matrix to upper-diagonal form. For the complex-energy method and the discrete-solution method, a Newton's method is used to solve for the energy where the matrix

determinant is zero (derived from the multiplication of the diagonal elements of the reduced matrix). For the resonant-tunnelling method, we used Brent's method of parabolic fitting [Press, 1989] to minimize $R_{1,n}$ and solve for the energy. One can then set to $C_s = 1$, and the wavefunction coefficients are produced by backwards substitution. We then performed Rhomberg integration [Press, 1989] on the wavefunction probability to determine the normalization constant. A sample electron and hole wavefunction solution for material 'A' at about -7V bias is shown in Fig. 4.2.

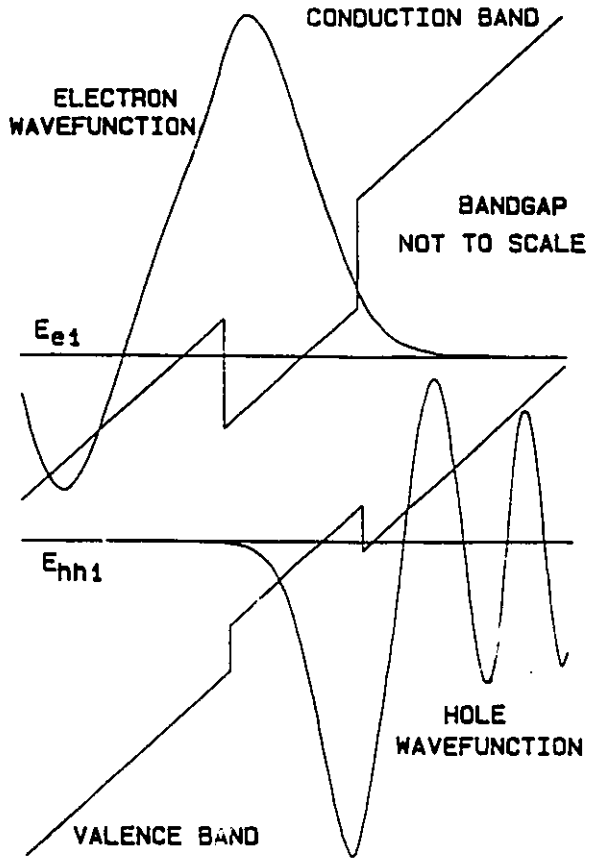


**Figure 4.2** The solution energies and wavefunctions for a single quantum-well of material 'A'. This situation corresponds to about -7V bias. The bandgap is not to scale in this diagram.

## 4.5 A Comparison of Results from the Energy-Solution Methods

Calculations show that the energy shifts with field are almost the same for multiple and single quantum-well calculations for the structure of this investigation. For simplicity we therefore calculate the theoretical bandgaps vs. field for a 9 nm wide single $In_{.124}Ga_{.876}As$ quantum-well corresponding to material 'B'. Figure 4.3 shows the shift in bandgap for the resonant-tunnelling method with no conduction-

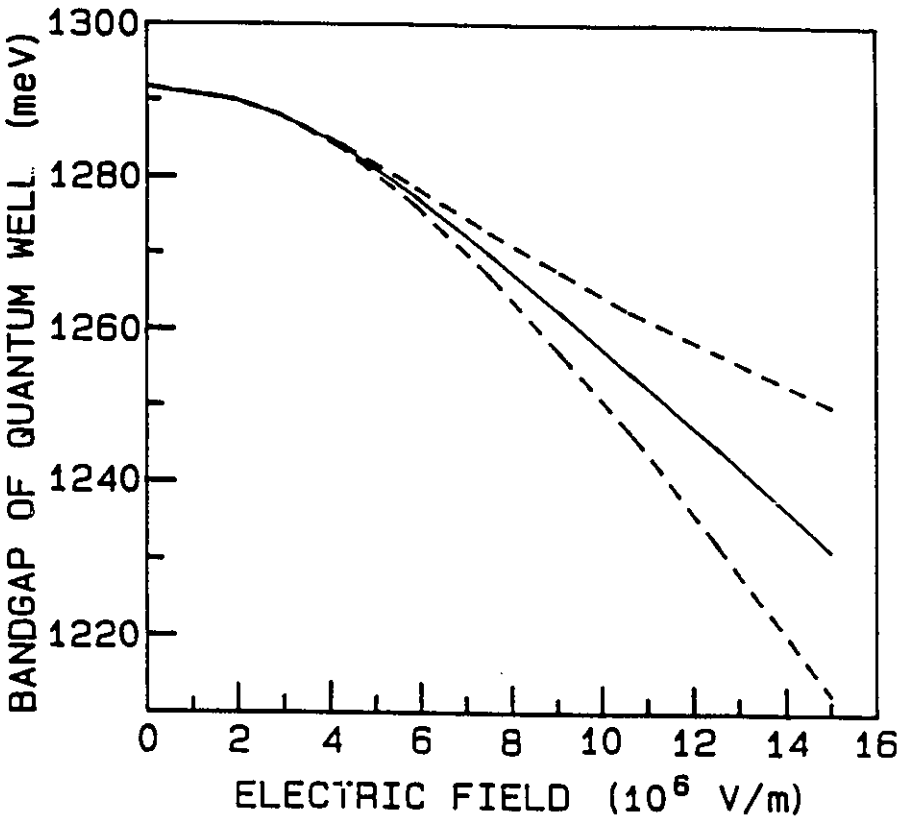


**Figure 4.3** The difference between the electron-1 and heavy-hole-1 energies vs. electric field (solid line) for the resonant-tunnelling method with parabolic bands, showing the energy width due to tunnelling (dashed line).

band non-parabolicity. Also shown is the half-maximum points on either side of the resonance positions (derived by summing the electron and hole tunnelling widths). In Fig. 4.4 we show the deviation from the calculation of Fig. 4.3 for all the different solutions: that is the resonant-tunnelling, discrete-solution, and complex-energy methods, each with and without conduction-band non-parabolicity. Notice that the discrete solution method deviates considerably from the resonant-tunnelling and complex-energy methods at high fields. Also, the calculated band gaps with conduction-band non-parabolicity are shifted slightly downwards, but otherwise follow a very similar trend to the parabolic band case. This indicates that conduction-band

non-parabolicity is not an important factor in determining energy shifts with field.

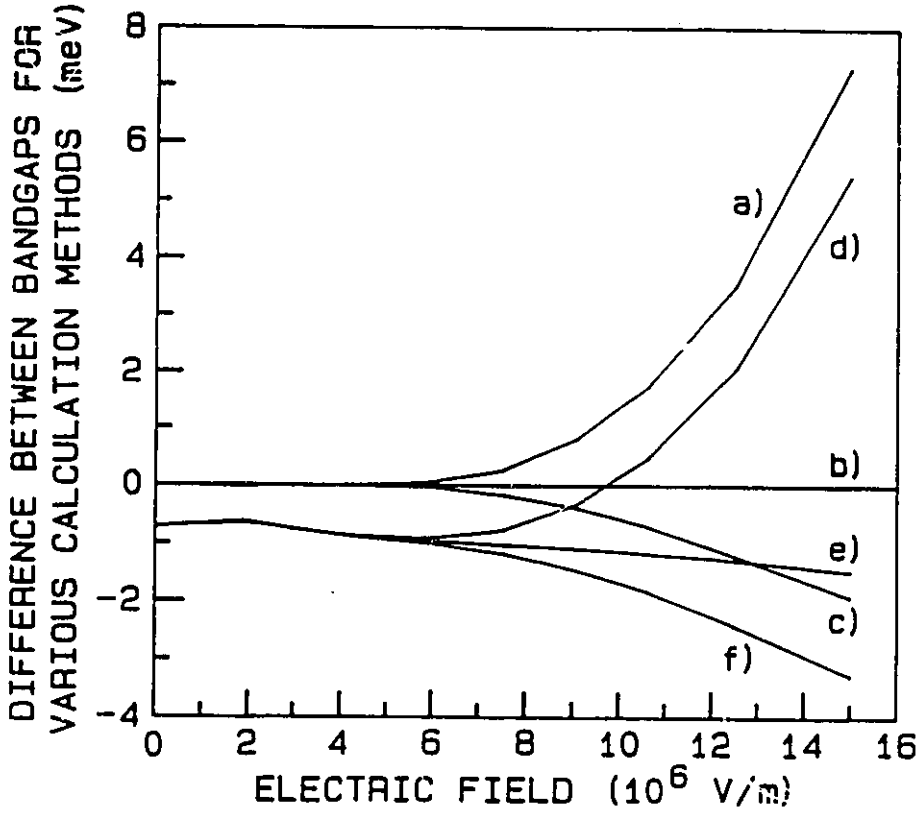


**Figure 4.4** The difference between the bandgap energies calculated for Case 1 (a, b, c) and Case 2 (d, e, f). Compared are the discrete-solution method (a, d), the resonant-tunnelling method (b, e), and complex-energy method (c, f).

Notice also that the deviations in the calculation methods are approximately proportional to the energy width due to tunnelling shown in Fig. 4.3. Since the imaginary portion of the complex energy is equal to the half-width of the broadening due to tunnelling, one can also compare the tunnelling widths calculated by the resonant-tunnelling and complex-energy methods. They correspond to better than one percent at low field, and deviate by about ten percent at $1.5 \times 10^7$ V/m.

## 4.6 Theoretical vs. Experimental Exciton Shifts with Field

The first step in comparing theoretical and experimental band-edge shifts with applied voltage is to determine the relationship between bias voltage and internal electric field. The electric field will be reasonably constant in the intrinsic region

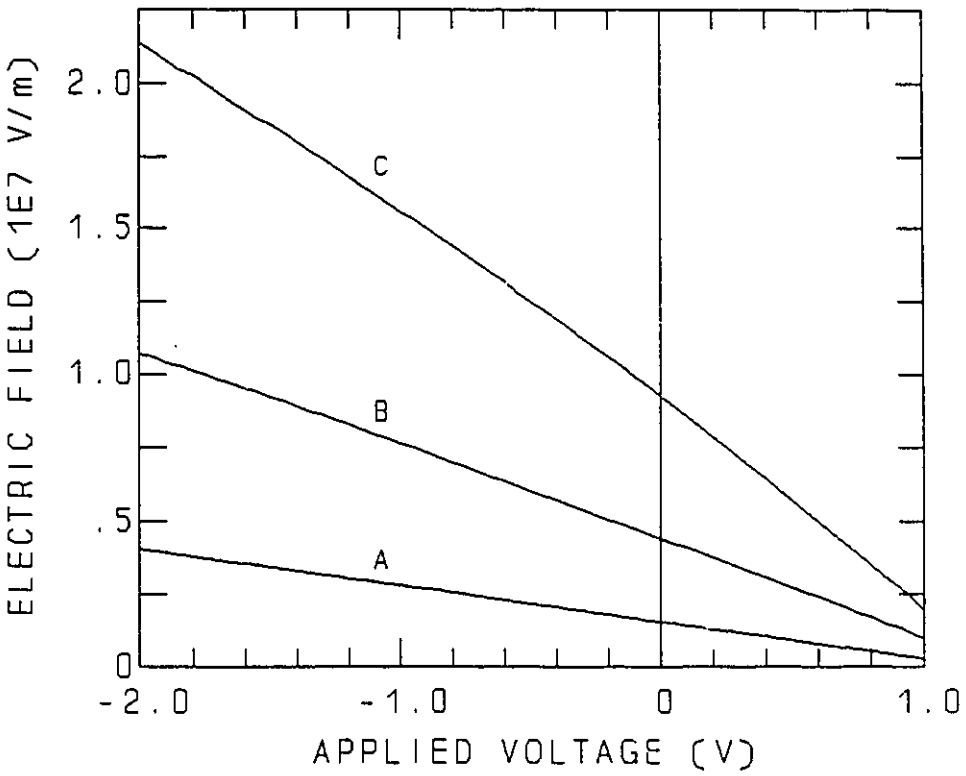


**Figure 4.5** The field vs. applied voltage for the intrinsic regions of materials A, B, and C. The small voltage range from -2V to 1V is shown.

(with residual doping levels below $10^{15}$ $cm^{-3}$). The *n* and *p*-type doping levels on either side of the intrinsic region are the same densities. The field is solved by integration of Poisson's equation in the abrupt-junction approximation.

$$\nabla^2 V = -\frac{\rho}{\epsilon_0 \epsilon_r} \qquad [4.23]$$

Here V is the potential, ρ is the charge density (the same magnitude as the doping density for depleted n and p regions), and $\epsilon_0\epsilon_r$ is the electric permittivity of the

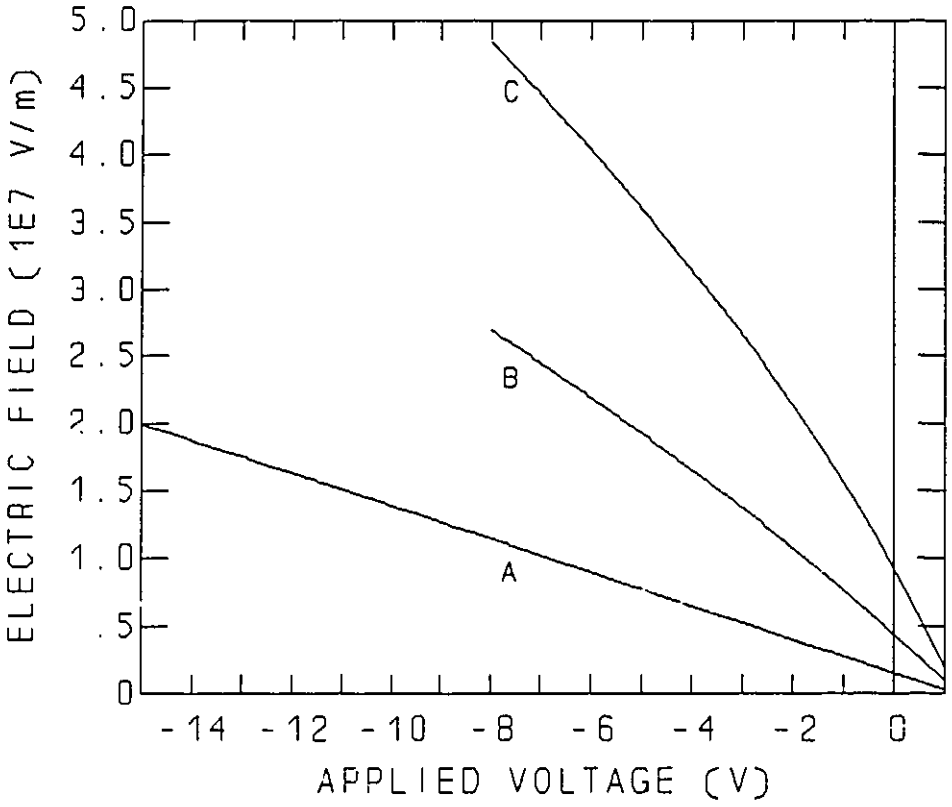


**Figure 4.6** The field vs. applied voltage relationship for materials A, B, and C. Results are shown for the full voltage ranges used in any experiments.

semiconductor. For our particular situation, define the intrinsic region thickness as $2t$, the total depletion region thickness as $2t+2l$, and one finds that,

$$l = \sqrt{t^2 - \frac{\epsilon_0 \epsilon_r (V_{bi} + V_{app})}{q\rho}} - t \quad ; \quad |E| = \frac{q\rho l}{\epsilon_0 \epsilon_r} \qquad [4.24]$$

The built-in potential is $V_{bi}$ (negative), the applied potential is $V_{app}$ and the magnitude of the electron charge is $q$. The resulting field vs. voltage curves are given in Figures 4.5 and 4.6.

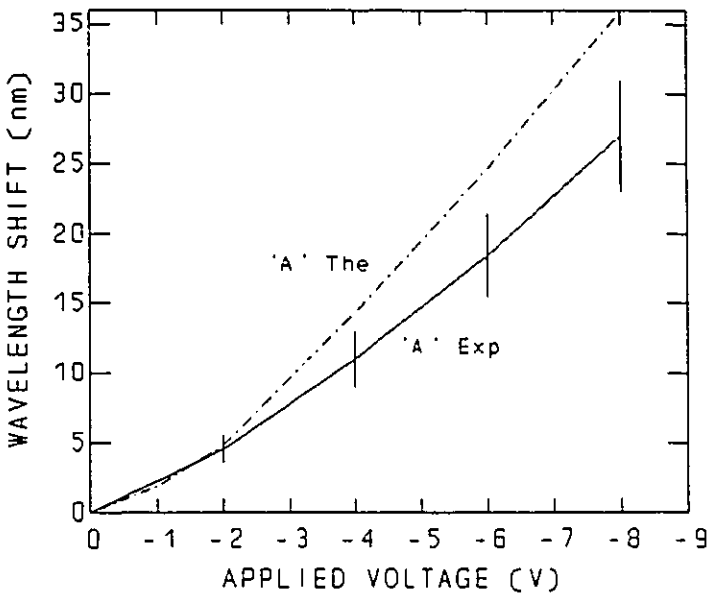


**Figure 4.7** Experimental and theoretical wavelength red-shifts vs. applied bias voltage for material 'A'. Experimental points are shown with error bars.

One can now compare the theoretical and experimental shifts with applied bias voltage for the various materials. At very high fields, the band-edge exciton peak is not visible, and its position cannot be measured. At lower fields the peak position can be measured, but with increasing uncertainty as the peak broadens and weakens with field. One should mention that the theoretical curves should not match the experimental ones because we have not yet taken into account the effects of

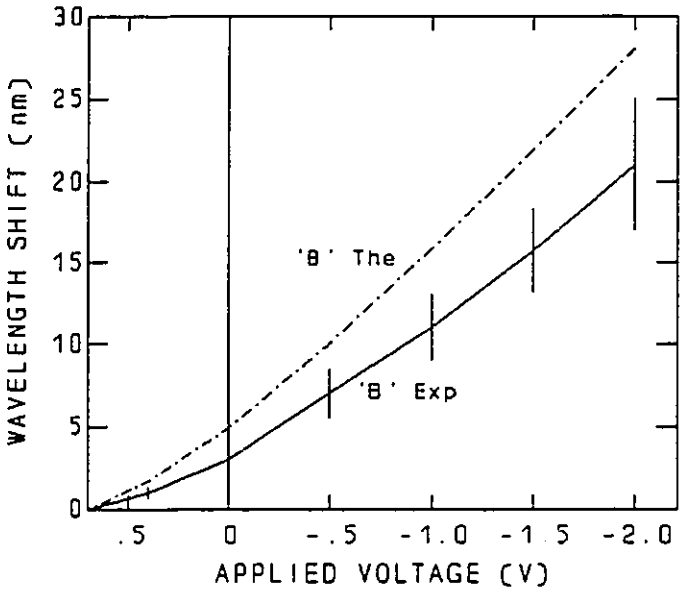


**Figure 4.8** Theoretical and experimental wavelength red-shifts vs. applied bias voltage for material 'B'. The experimental points are shown with error bars.

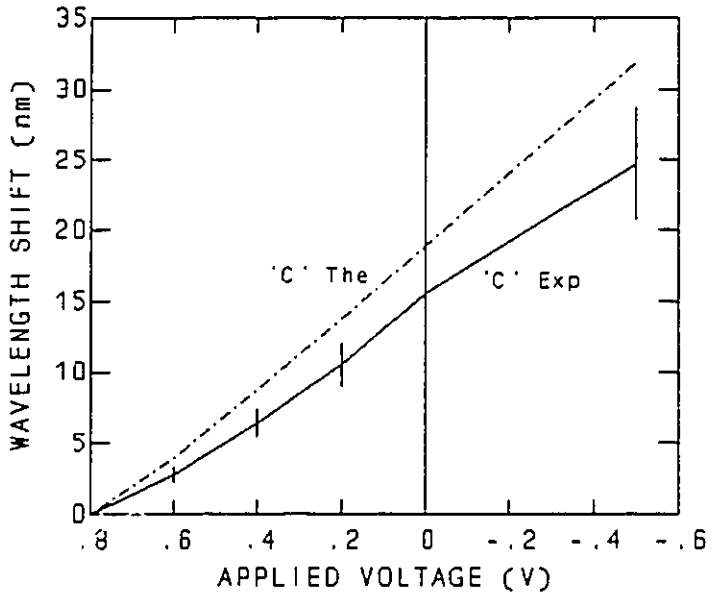


**Figure 4.9** Theoretical and experimental wavelength red-shifts vs. applied bias voltage for material 'C'. The experimental points are shown with error bars.

binding energy changes with field. The experimental vs. theoretical peak shifts with

field are given in Figures 4.7, 4.8, and 4.9 for materials A, B, and C respectively. The experimental curves are derived from visual inspection of the transverse photocurrent and transmission spectra, and the theoretical curves are calculated using the resonant tunnelling method, assuming parabolic bands. The experimental shifts seen in the materials appear to be less than those calculated theoretically. This is partly accounted for by a drop in exciton binding energy with field. Deviations in layer thicknesses from those assumed can have some effect also. However, as long as all layers are in error by the same percentage, the resulting field changes cause opposite and counteracting changes. A possible explanation is some screening of the field at poor contacts. Measurements show, however, that the contacts are reasonably good. Interactions between adjoining wells in the MQW structure can make some difference, but probably not more than 2 nm at any field. There is, however, a large uncertainty in the determination of the experimental peak positions. The exciton peak strength drops at higher fields, and blends in with a non-excitonic absorption edge. It is not always clear where the peak is actually situated.

Also, there is really no longer a single exciton transition, but rather a range of energy transitions at higher fields. Varying optical transition strengths with energy can result in an apparently smaller shift than was calculated in this chapter. This situation of a continuum of transitions is addressed in Chapter 7.

## 4.7 Conclusions

Three exact solution methods have been compared theoretically, each with

and without band non-parabolicity. The discrete solution and resonant-tunnelling methods using Airy functions have been reported before [Ghatak, 1990]. However, the methods were never compared, and the complex-energy solutions have not been done. The non-parabolic band solution using functions defined here as $A^W$ and $B^W$ has not been done previously. Band non-parabolicity was usually incorporated only into a staircase approximation [Ghatak, 1988] of the potential. Comparisons revealed that the resonant-tunnelling method was the most practical to use, since it works with real wavefunctions, and it gives information about the broadening of the energy solutions due to their tunnelling out of the well. The discrete solution method also uses real wavefunctions, but does not give accurate results at high fields, where the energy broadening is large. The complex energy solution gives a lifetime value, and therefore a energy width value, but it is not clear how physical the actual wavefunction is. It is preferable to have real energies and wavefunctions so that one can use perturbation theory or variational mixing methods when calculating actual exciton solutions later. It was decided that conduction band non-parabolicity did not significantly affect the energy shifts, although a slight drop in the absolute energy solutions was seen.

The comparisons of energy shift with field have some discrepancy, but this may be accounted for by changes in the binding energy with field, and the changes in the relative strength of the exciton as compared to the absorption edge due to free carriers. As the exciton strength drops, it blends in with this free-carrier edge, and it is not clear where the exciton position really is. It is clear that one must do more

than model the exciton shifts to theoretically determine the quantum-well electro-absorption. One must model the strength, broadening, and shifts of both the free-carrier edge and the e1-hh1 exciton peak with field. At high fields, one may have to model the absorption edge as a continuum of transitions.

# CHAPTER 5

## Valence Band Mixing in a Quantum-Well Solution

### 5.1 Introduction

It is known that valence-band mixing greatly affects the dispersion curves for $k$-values parallel to the planes of the quantum-well layers [Altarelli, 1985]. This has been investigated by a number of authors [Ahn, 1988][Altarelli, 1985], but it not clear what one should use as a band-edge heavy-hole mass in our heavily strained materials. A parallel effective mass is necessary for calculation of the band-edge exciton's binding energy and oscillator strength. We therefore derive these effective masses by solving for the dispersion curve for holes in the parallel direction (ignoring matrix terms linear in $k$).

### 5.2 Valence Band Mixing in Quantum Wells

The Schrodinger equation for the valence band (with electron potential energy positive) in the envelope-function approximation for a material layer '$n$' is:

$$\left[\sum_{q=1}^{4} H_{pq}^{1} A_n^q(z) + [V_n - E]\right] A_n^p(z) = 0 \; : \quad p,q \in \{1..4\} \qquad [5.1]$$

$V(z)$ is the unstrained valence band potential in the $z$-direction, E is the energy where the full hole envelope wavefunction is defined by:

$$\Psi_n(z) = \sum_{m=1}^{4} A_n^m(z)\psi_m \qquad [5.2]$$

The basis for the matrix is like that of Luttinger [Luttinger, 1955], except with real coefficients. They are the p-like hydrogenic wavefunctions $|J,m_j>$ given by:

$$\psi_1 = \left|\frac{3}{2},\frac{3}{2}\right\rangle = -\frac{1}{\sqrt{2}}|(X+iY)\uparrow\rangle \qquad [5.3]$$

$$\psi_2 = \left|\frac{3}{2},-\frac{1}{2}\right\rangle = \frac{1}{\sqrt{6}}|(X-iY)\uparrow> + \sqrt{\frac{2}{3}}|Z\downarrow\rangle \qquad [5.4]$$

$$\psi_3 = \left|\frac{3}{2},\frac{1}{2}\right\rangle = -\frac{1}{\sqrt{6}}|(X+iY)\downarrow\rangle + \sqrt{\frac{2}{3}}|Z\uparrow\rangle \qquad [5.5]$$

$$\psi_4 = \left|\frac{3}{2},-\frac{3}{2}\right\rangle = \frac{1}{\sqrt{2}}|(X-iY)\downarrow\rangle \qquad [5.6]$$

The up and down arrows mean spin up and spin down states (spin in +z and -z directions). The Hamiltonian $H^1$ is given by [Luttinger, 1955] [Ahn, 1988] [Twardowski, 1987] [Broido, 1985]:

$$H^1 = -\begin{bmatrix} P+(Q+\zeta_n) & R & -S & 0 \\ R^* & P-(Q+\zeta_n) & 0 & S \\ -S^* & 0 & P-(Q+\zeta_n) & R \\ 0 & S^* & R^* & P+(Q+\zeta_n) \end{bmatrix} \qquad [5.7]$$

Here $\zeta_n$ is the strain potential, while P,Q,R,S are given by:

$$P = \frac{1}{2}\left(\frac{\hbar^2}{m}\right)\gamma_1(k_x^2+k_y^2+k_z^2) \qquad [5.8]$$

$$Q = \frac{1}{2}\left(\frac{\hbar^2}{m}\right)\gamma_2(k_x^2+k_y^2-2k_z^2) \qquad [5.9]$$

$$S = \sqrt{3}\left(\frac{\hbar^2}{m}\right)\gamma_3(k_x-ik_y)k_z \qquad [5.10]$$

$$R = -\frac{\sqrt{3}}{2}\left(\frac{\hbar^2}{m}\right)\overline{\gamma}(k_x-ik_y)^2+T \quad , \overline{\gamma} = \frac{\gamma_2+\gamma_3}{2} \qquad [5.11]$$

$$T = \begin{cases} \frac{\sqrt{3}}{4}\left(\frac{\hbar^2}{m}\right)(\gamma_3-\gamma_2)(k_x-ik_y)^2, \text{ normally} \\ 0, \text{ axial approximation} \end{cases} \qquad [5.12]$$

The gammas are the Luttinger parameters [Luttinger, 1956], which can be different for each material layer, though we haven't explicitly labelled them with the index '*n*'. The variables $k_x$ and $k_y$ are the in-plane *k*-vectors, and can be considered constants, while $k_z$ is the Hermitian operator $-i\partial/\partial z$. $R^*$ means the Hermitian conjugate of *R*, not the numerical complex conjugate. We have defined in the axial approximation [Altarelli, 1985] that $T=0$. In this approximation, the energy solutions to the Hamiltonian are invariant to the direction of the wavevector *k* in the plane of the layers. The axial approximation is a good compromise for an average energy solution for all *k*- directions in the *x-y* plane. While the original form of the Luttinger Hamiltonian has been solved exactly by Andreani et al. [Andreani, 1987] for the single quantum-well, and has been successfully repeated by us, we choose instead to show the method of Broido and Sham [Broido, 1985] for reducing the Hamiltonian to a block diagonal form. This will reduce the calculations necessary to exactly solve for the energies. The Hamiltonian $H^1$ is transformed by a unitary transformation *U* into:

$$\tilde{H} = UH^{1}U^{\dagger} = \begin{bmatrix} P+(Q+\zeta_n) & \tilde{R} & 0 & 0 \\ \tilde{R}^{*} & P-(Q+\zeta_n) & 0 & 0 \\ 0 & 0 & P-(Q+\zeta_n) & \tilde{R} \\ 0 & 0 & \tilde{R}^{*} & P+(Q+\zeta_n) \end{bmatrix} \quad [5.13]$$

where $\tilde{R}=|R-T|-i|S|-|T|e^{i\phi}$ . In the axial approximation this reduces to the form reported by others [Broido, 1985] [Ahn, 1988], $\tilde{R}=|R|-i|S|$. The magnitude signs do not mean the numerical magnitude, but rather the square-root of the term times its Hermitian conjugate. For complex or imaginary $k_z$ the result can be complex or imaginary. The unitary transformation $U$ is [Broido, 1985][Twardowski, 1987]:

$$U = \begin{bmatrix} a^{*} & 0 & 0 & -a \\ 0 & b^{*} & -b & 0 \\ 0 & b^{*} & b & 0 \\ a^{*} & 0 & 0 & a \end{bmatrix} \quad [5.14]$$

where

$$a = \frac{1}{\sqrt{2}}\exp\left[i\left(\frac{3\pi}{4}-\frac{3\phi}{2}\right)\right] \quad [5.15]$$

$$b = \frac{1}{\sqrt{2}}\exp\left[i\left(-\frac{\pi}{4}+\frac{\phi}{2}\right)\right] \quad [5.16]$$

and $\phi$ is the azimuthal angle in the plane parallel to the layers. The $k$-vector can be defined in terms of cylindrical co-ordinates in material layer $n$:

$$\vec{k}_n = (k_l\cos(\phi),k_l\sin(\phi),k_{z,n}),\ k_l = \sqrt{k_x^2+k_y^2},\ \phi = \tan^{-1}\left(\frac{k_y}{k_x}\right) \quad [5.17]$$

The basis functions change to the following:

$$|1\rangle = a\left|\frac{3}{2},\frac{3}{2}\right\rangle - a^*\left|\frac{3}{2},-\frac{3}{2}\right\rangle \qquad [5.18]$$

$$|2\rangle = b\left|\frac{3}{2},-\frac{1}{2}\right\rangle - b^*\left|\frac{3}{2},\frac{1}{2}\right\rangle \qquad [5.19]$$

$$|3\rangle = b\left|\frac{3}{2},-\frac{1}{2}\right\rangle + b^*\left|\frac{3}{2},\frac{1}{2}\right\rangle \qquad [5.20]$$

$$|4\rangle = a\left|\frac{3}{2},\frac{3}{2}\right\rangle + a^*\left|\frac{3}{2},-\frac{3}{2}\right\rangle \qquad [5.21]$$

The hole wavefunction $\Psi$ can now be defined in terms of this basis.

$$\Psi_n(z) = \sum_{m=1}^{4} B_n^m(z)|m\rangle \qquad [5.22]$$

The upper and lower blocks of the new Hamiltonian $\tilde{H}$ can be solved separately. The Schrodinger equation becomes in the bases $|1\rangle$ to $|4\rangle$ in the envelope function approximation:

$$\left[\sum_q \tilde{H}_{pq}B_n^q + [V_n - E]\right] = 0 : \begin{cases} p,q \in \{1..2\} \text{ for upper} \\ p,q \in \{3..4\} \text{ for lower} \end{cases} \qquad [5.23]$$

Now, one has to determine the boundary conditions for the interfaces between two material regions. As shown in Appendix F, if the wavefunction $\psi$ is continuous, then so are the following vectors:

$$\vec{I}_n^U = \begin{bmatrix} (\gamma_1 - 2\gamma_2)k_z & -i\sqrt{3}\gamma_3 k_t \\ i\sqrt{3}\gamma_3 k_t & (\gamma_1 + 2\gamma_2)k_z \end{bmatrix} \begin{bmatrix} B_n^1 \\ B_n^2 \end{bmatrix} \text{ and } \vec{I}_n^L = \begin{bmatrix} (\gamma_1 + 2\gamma_2)k_z & -i\sqrt{3}\gamma_3 k_t \\ i\sqrt{3}\gamma_3 k_t & (\gamma_1 - 2\gamma_2)k_z \end{bmatrix} \begin{bmatrix} B_n^3 \\ B_n^4 \end{bmatrix} \qquad [5.24]$$

Before solving for situations involving multiple layers, one must know the wavefunction solution for a single layer of index $n$. Two independent solutions can

be found : one involving only states |1> and |2> (the upper block), and the other involving only states |3> and |4> (the lower block). We will call these solutions $f_n^U(k)$ and $f_n^L(k)$:

$$\vec{f}_n^U(z,\vec{k}) = \begin{bmatrix} -\tilde{R} \\ P+E-V_n+(Q+\zeta) \end{bmatrix} \exp(ik_{z,n}z) \text{ , in the basis } \begin{bmatrix} |1\rangle \\ |2\rangle \end{bmatrix} \qquad [5.25]$$

$$\vec{f}_n^L(z,\vec{k}) = \begin{bmatrix} -\tilde{R} \\ P+E-V_n-(Q+\zeta) \end{bmatrix} \exp(ik_{z,n}z) \text{ , in the basis } \begin{bmatrix} |3\rangle \\ |4\rangle \end{bmatrix} \qquad [5.26]$$

The variable $k_{z,n}$ is the solved $k_z$ value for material $n$. Now, the upper and lower blocks can be solved separately, and have identical eigenenergies. However, each block has four degenerate solutions with different $k_z$. These can be derived by solving for $k_z$ (for a constant $k_x$ and $k_y$) from the following determinant:

$$(E-V_n+P)^2 = (Q+\zeta_n)^2 + \tilde{R}\tilde{R}^* \qquad [5.27]$$

We define the solutions in the following manner:

$$k_{z,n} = \{k_{h,n}, k_{l,n}, -k_{l,n}, -k_{h,n}\} \qquad [5.28]$$

These $k$-values are the positive-going and negative-going waves for the heavy and light holes. The envelope function has been defined as the four-element vector $B_n$ in Eqn. 5.22. We define the two-element envelope-function vector $B_n^\sigma$ where $\sigma = \{\text{Upper or Lower}\}$. Consider the solution to the Upper or Lower block (but not both at once).

$$\vec{B}_n^\sigma = F_n^1\vec{f}_n^\sigma(k_{h,n}) + F_n^2\vec{f}_n^\sigma(k_{l,n}) + F_n^3\vec{f}_n^\sigma(-k_{l,n}) + F_n^4\vec{f}_n^\sigma(-k_{h,n}) \qquad [5.29]$$

The four constants $F_{n1..n4}$ are unknowns which must be solved for each layer n. Consider the case of a structure consisting of $s$ layers. We will have $4s$ unknowns. One can solve exactly for the Eigen-energies and the non-normalized wavefunctions

just by using the boundary conditions at the interfaces, and by introducing boundary conditions at $z \to \infty$ and $z \to -\infty$. Enumerate the layers so that the negative-most $z$-layer is *1* and the positive-most layer is $s$. At the negative $z$ boundary, set:

$$F_1^3 = 0 \ , \ F_1^4 = 0 \qquad [5.30]$$

For a single upper or lower block, this amounts to two equations. At the interface $z = z_{n|n-1}$ between the layer $n$ and layer $n$-*1*:

$$\vec{B}^o_{n-1}(z_{n|n-1}) \ = \ \vec{B}^o_n(z_{n|n-1}) \ , \ n \in \{2..s\} \qquad [5.31]$$

$$\vec{\Gamma}^o_{n-1}(z_{n|n-1}) \ = \ \vec{\Gamma}^o_n(z_{n|n-1}) \ , \ n \in \{2..s\} \qquad [5.32]$$

This gives another (*4s-4*) equations for a particular block. Lastly, at the positive $z$ boundary set:

$$F_s^1 = 0 \ , \ F_s^2 = 0 \qquad [5.33]$$

We now have *4s* linear homogeneous equations with *4s* unknowns. One can set up a matrix, which only has a non-trivial solution if the determinant is zero. We store only those filled blocks close to the diagonal of the matrix. By using naive Gaussian elimination to solve the matrix, the off-diagonal zeros do not change, and are not needed. A diagram of the resultant matrix blocks are given in Figure 5.1.

As shown by Andreani et al. [Andreani, 1987], for a symmetric single-quantum well, one can further reduce the number of unknowns by realizing that the solutions are either symmetric or anti-symmetric about the well centre. We do not do this to ensure that our method can be generalized to any situation.

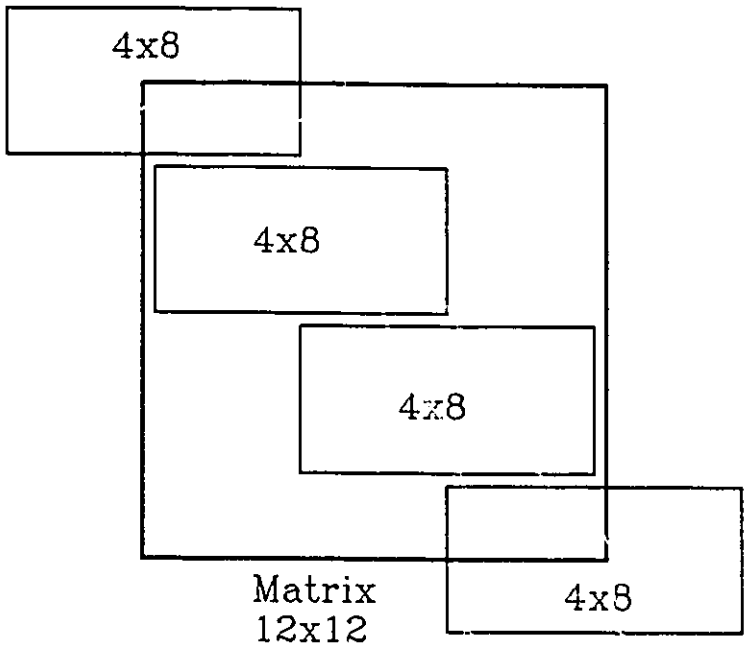


**Figure 5.1** The structure of the valence-band solution matrix for a three-layer structure. The continuity conditions at each interface create 4x8 matrices, and the end conditions create 2x4 matrices, stored as 4x8.

## 5.2 Results

The structure in this investigation is a type-I superlattice for heavy-holes, while it is a type-II superlattice for light holes. In order not to ignore the effects of the light holes, we use a five layer approximation for the structure. The parameters used are shown in Table 5.1 for materials A,B, and C. The heavy-hole well is surrounded by two light-hole wells on either side. One might be tempted to say that since the light holes are separated both in energy and in space from the first heavy-hole, one can ignore the off-diagonal terms in the Hamiltonian. In that case, the parallel effective mass would be $m_0/(\gamma_1+\gamma_2)$ [Altarelli, 1985]. We show in Figure 5.2 the parallel effective mass vs. $k_{\|}$ is shown for the three materials. These were calculated by the formula,

**Table 5.3** Parameters for the hole bands in 5-layer approximations of the InGaAs-GaAs MQW materials A,B, and C. The parameters are used to calculate the quantum-well parallel-direction hole dispersion.

| **Material 'A' Parameters** | | | | | |
|---|---|---|---|---|---|
| | **Layer 1** | **Layer 2** | **Layer 3** | **Layer 4** | **Layer 5** |
| $\zeta_n$ (meV) | 0.0 | 10.7 | -14.9 | 10.7 | 0.0 |
| $V_n$ (meV) | 3.6 | 8.2 | 18.5 | 8.2 | 3.6 |
| $\gamma_1$ | 8.23 | 6.85 | 8.23 | 6.85 | 8.23 |
| $\gamma_2$ | 2.78 | 2.10 | 2.78 | 2.10 | 2.78 |
| $\gamma_3$ | 3.59 | 2.90 | 3.59 | 2.90 | 3.59 |
| **Material 'B' Parameters** | | | | | |
| | **Layer 1** | **Layer 2** | **Layer 3** | **Layer 4** | **Layer 5** |
| $\zeta_n$ (meV) | 0.0 | 12.15 | -17.3 | 12.15 | 0.0 |
| $V_n$ (meV) | -2.50 | 9.65 | 21.50 | 9.65 | -2.50 |
| $\gamma_1$ | 8.44 | 6.85 | 8.44 | 6.85 | 8.44 |
| $\gamma_2$ | 2.88 | 2.10 | 2.88 | 2.10 | 2.88 |
| $\gamma_3$ | 3.69 | 2.90 | 3.69 | 2.90 | 3.69 |
| **Material 'C' Parameters** | | | | | |
| | **Layer 1** | **Layer 2** | **Layer 3** | **Layer 4** | **Layer 5** |
| $\zeta_n$ (meV) | 0.0 | 0.0 | -32.9 | 0.0 | 0.0 |
| $V_n$ (meV) | -16.5 | 0.0 | 16.4 | 0.0 | -16.5 |
| $\gamma_1$ | 8.36 | 6.85 | 8.36 | 6.85 | 8.36 |
| $\gamma_2$ | 2.84 | 2.10 | 2.84 | 2.10 | 2.84 |
| $\gamma_3$ | 3.65 | 2.90 | 3.65 | 2.90 | 3.65 |

$$\frac{1}{m_{\perp}^{*}(k_{\perp})} = \frac{1}{\hbar^2}\frac{\partial^2 E(k_{\perp})}{\partial k_{\perp}^{\,2}} \qquad [5.34]$$

Because energies were only calculated for a finite number of $k_{\parallel}$ values, a second difference formula was used to calculate the second derivative. One can see from Figure 5.2 that the mass values are considerably higher than the value of about $0.09m_0$ that one would expect from the uncoupled-band model. This suggests that a calculation of the hole dispersion curves is necessary if one wishes to know the hole effective masses. Coulomb binding further perturbs the system and mixes the heavy

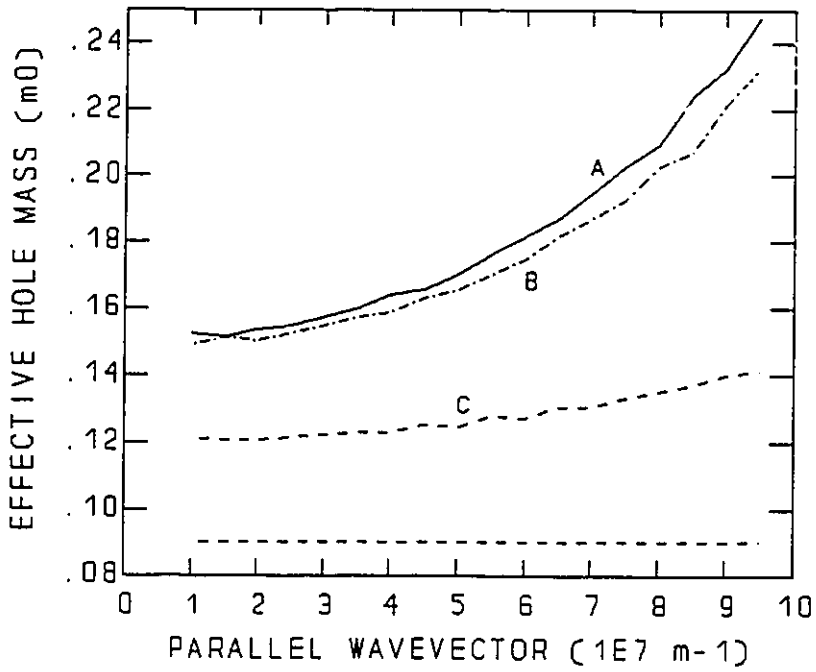


**Figure 5.2** The calculated parallel effective masses of the heavy-hole-1 energy level vs. the wavevector $k_{\|}$ for materials A,B,and C. The mass $m_0/(\gamma_1+\gamma_2)=0.09m_0$ is also shown.

and light holes. This means that the effective masses calculated here may not be exact, but as long as the first heavy-hole solution and the first light-hole solution are separated by a considerable amount in energy they should be close. For unstrained situations, where the light and heavy-hole excitons are close in energy, one would have to include the Coulomb potential and the hole Hamiltonian in some sort of variational solution to the total band-edge quantum-well exciton [Ekenberg, 1987]. Fortunately, that is not necessary for our materials. The parallel-direction wavevectors should be mostly below $5x10^7$ $m^{-1}$ within an exciton, so the calculated masses can be treated as constants. The resultant parallel heavy-hole masses for the first hole solution are approximately $0.15m_0$ for materials A and B, and $0.12m_0$ for material C.

## 5.3 Discussion

Rudin et al. [Rudin, 1988] [Rudin, 1990] used calculated $m^*_{\parallel}$ values of $.15m_0$ for 10nm width unstrained AlGaAs-GaAs wells in their work. Our calculations suggest a similar value. The lower effective mass of material 'C' is due to the larger strain, and therefore the larger splitting between light and heavy-hole solution energies. This larger splitting reduces the mixing between bands, and results in a parallel mass value closer to the uncoupled-band value of $0.09m_0$. These mass values may now be used in calculations of the band-edge exciton binding energies.

# CHAPTER 6

## A Determination of the Binding Energy

### 6.1 Introduction

The band-edge absorption is dominated by the *1s* electron-1 to heavy-hole-1 exciton transition. This exciton is a hydrogenic state, where the electron and hole are bound by their Coulomb attraction. In order to calculate the band-edge absorption changes with applied electric field, one must first calculate the binding energy of this excitonic state, as well as the corresponding wavefunction. In this chapter, an approximate solution method which assumes a wavefunction separable in circular-cylindrical co-ordinates will be used to calculate the exciton solutions in our three material growths for various electric fields.

### 6.2 Overview of Binding Energy Calculation Methods

The Schrodinger equation for a bound electron and hole with the inclusion of binding energy is:

$$[H_{elec}(z_e) - H_{hole}(z_h) + H_\rho(\rho) + H_{Coulomb}]\psi(\rho, z_e, z_h) = 0 \qquad [6.1]$$

The Hamiltonians $H_{elec}(z_e)$ and $H_{hole}(z_h)$ are for the electron and hole in the z-direction for no Coulomb interaction. These are the same Hamiltonians used to calculate the *z*-direction wavefunctions in chapter 4. The variable $\rho$ is the electron-hole separation along the plane of the layers ($\rho^2 = x^2 + y^2$). The Hamiltonian $H_\rho$ is

given by:

$$H_{\rho}(\rho) = -\frac{\hbar^2}{2\mu}\frac{1}{\rho}\frac{\partial}{\partial\rho}\left(\rho\frac{\partial}{\partial\rho}\right) \ , \ \mu = \frac{m_e^* m_h^*}{m_e^* + m_h^*} \qquad [6.2]$$

where $\mu$ is the reduced in-plane mass, and the Hamiltonian $H_{\text{Coulomb}}$ is:

$$H_{Coulomb} = -\frac{e^2}{4\pi\epsilon_0\epsilon_r}\frac{1}{\sqrt{\rho^2+(z_e-z_h)^2}} \qquad [6.3]$$

An analytical solution of the Schrodinger equation is not possible, and a numerical one is extremely impractical. Therefore one usually assumes a solution separable into a no-Coulomb binding part and an electron-hole interaction part. Let us define the wavefunction solutions $\psi_e(z_e)$ and $\psi_h(z_h)$, calculated for the electron and hole in the quantum-well in the absence of a Coulomb potential. These are the same wavefunctions calculated in chapter 4. One then lets the exciton wavefunction $\psi(\rho,z_e,z_h)$ be:

$$\psi(\rho,z_e,z_h) = \psi_e(z_e)\psi_h(z_h)\phi_{e\text{-}h}(\rho,z_e-z_h) \qquad [6.4]$$

The binding energy $E_B$ is defined by,

$$E_{tot} = E_{elec} - E_{hole} - E_B \qquad [6.5]$$

where $E_{\text{elec}}$ and $E_{\text{hole}}$ are the Eigen-energies of $H_{\text{elec}}$ and $H_{\text{hole}}$ (with electron energy positive and hole energy negative).

The solution to the exciton within a quantum-well has been considered by a number of authors [Bastard, 1982b] [Ekenberg,1987] [Andreani,1989] [Mo, 1988] [Sanders, 1985] [Wu, 1989]. Some of these [Ekenberg, 1987] [Andreani, 1989] [Mo, 1988] [Sanders, 1985] have included valence band mixing in their analyses. Most work in the literature, however, has assumed a form for the excitonic wavefunction.

and has employed a variational procedure to determine the unknown coefficients. The usual forms for the electron-hole interaction term for the 1s-exciton wavefunction have been [Bastard, 1982b] [Bastard, 1986]:

$$\phi_{e\text{-}h,1} = N_1 \exp\left(-\frac{\rho}{\lambda_1}\right) \qquad [6.6]$$

or,

$$\phi_{e\text{-}h,2} = N_2 \exp\left(-\frac{1}{\lambda_2}\sqrt{\rho^2+(z_e-z_h)^2}\right) \qquad [6.7]$$

Here $\lambda_1$ and $\lambda_2$ are variational parameters, $N_1$ and $N_2$ are normalization parameters. The function $\phi_{e\text{-}h,1}$ is simply the form for a two-dimensional hydrogenic state, while the second function $\phi_{e\text{-}h,2}$ is the form of a 3-dimensional-bulk hydrogenic state. Although these forms are easy to work with, they are clearly only approximations of the actual solution. While $\phi_{e\text{-}h,2}$ usually gives a larger binding energy [Bastard, 1982b] for the single quantum-well with no electric field, and is therefore the more accurate solution, it is not clear that this solution form is as appropriate in the situation of a transverse electric field. In an electric field the electron and hole wavefunctions are spatially separated, and some tunnelling to the continuum occurs, regardless of Coulomb binding. So, instead of using either solution form, we apply the solution method of Wu [Wu, 1989] to the case of the single quantum-well in an electric field.

Wu numerically solves for $\phi_{e\text{-}h}(\rho)$, assuming that it is a function of $\rho$ only. While this may not be accurate for very thick quantum-wells, Wu has shown that this method gives a larger binding energy than the form $\phi_{e\text{-}h,2}$ for $Al_{.25}Ga_{.75}As/GaAs$ single quantum-wells of less than 150Å thickness. The Hamiltonian for the exciton binding energy $E_B$ is given by,

$$\left[-\frac{\hbar^2}{2\mu}\frac{1}{\rho}\frac{d}{d\rho}\left(\rho\frac{d}{d\rho}\right)+V(\rho)\right]\phi_{e\text{-}h}(\rho) = -E_B\phi_{e\text{-}h}(\rho) \qquad [6.8]$$

where the potential in the radial direction $\rho$ is given by,

$$V(\rho) = -\frac{e^2}{4\pi\epsilon_0\epsilon_r\rho}\int dz_e\int dz_h\frac{|\psi_e(z_e)|^2|\psi_h(z_h)|^2}{\sqrt{1+\left(\frac{z_e-z_h}{\rho}\right)^2}} \qquad [6.9]$$

By using the appropriate functions $\psi_e(z_e)$ and $\psi_h(z_h)$ calculated for electrons and holes in a single quantum-well with an applied electric field, we can solve for the binding energy. One can extend this method to solve for the binding energy in a multiple quantum-well (MQW) with strongly interacting wells also. One would define $\psi_e(z_e)$ and $\psi_h(z_h)$ as linear combinations of the various MQW solutions within a certain energy range. Given a good starting guess for the mixing coefficients, a variational procedure would then be used to minimize the total energy of the system.

## 6.3 The Exciton Calculation Methods and Solutions

We have used a Runge-Kutta method with adaptive stepsize [Press, 1989] to integrate the binding energy differential equation. A shooting method was then used to solve for the particular binding-energy which satisfied the boundary conditions. To save in computing time, the potential $V(\rho)$ was calculated for a number of $\rho$ values, with a smaller stepsize between values being used for smaller $\rho$. The steps were even in the axis $\rho^{1/2}$. Then, we define a form factor $F(\rho)$ [Wu, 1989] such that:

$$V(\rho) = -\frac{e^2}{4\pi\epsilon_0\epsilon_r\rho}F(\rho) \qquad [6.10]$$

Given a set of values for $F(\rho)$, one can then use 4-point rational interpolation to

determine the other $F(\rho)$ values (and therefore $V(\rho)$ values) during the Runge-Kutta integration. The $F(\rho)$ curve for material 'B' at low field is given in Figure 6.1.

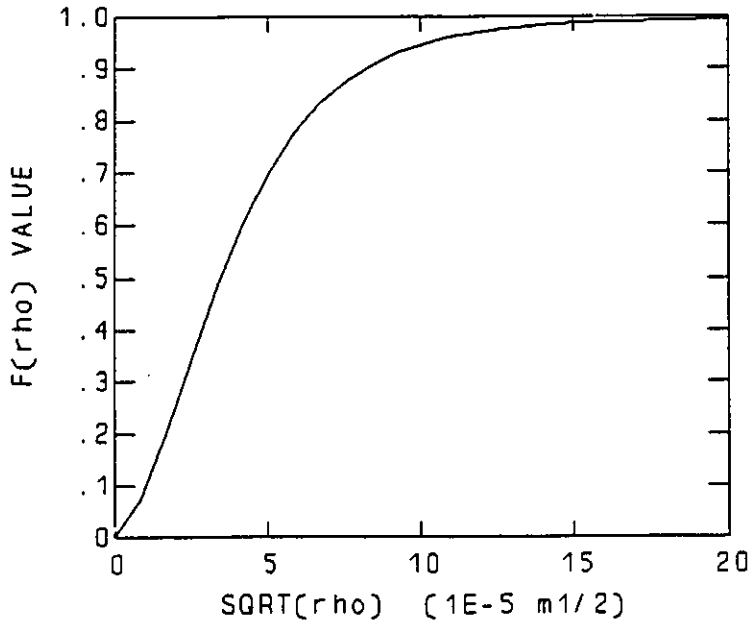


**Figure 6.1** The calculated $F(\rho)$ values vs. $\rho^{1/2}$ for the zero-field, single well situation in material 'B'. Four point rational interpolation is used to determine other $F(\rho)$ values given $\rho^{1/2}$.

The integration is performed on two simultaneous first order differential equations as opposed to the second order Schrodinger equation. They are,

$$\phi'(\rho) = \chi(\rho) \qquad [6.11]$$

$$\chi'(\rho) = \frac{2\mu}{\hbar^2}(V(\rho)+E_B)\phi(\rho) - \frac{1}{\rho}\chi(\rho) \qquad [6.12]$$

The boundary conditions for the radial wavefunction are,

$$\chi(\rho=0) = 0\ ,\quad \phi(\rho\to\infty) = 0 \qquad [6.13]$$

The radial integration is performed from $\rho = 1\text{x}10^{-13}$m to $\rho = 2.5\text{x}10^{-7}$m, with the

boundary conditions imposed as if these were $\rho = 0$ and $\rho = \infty$. The wavefunction $\phi(\rho)$ at $\rho = 0$ is arbitrarily defined as 1.0 during the solution. The attempted fractional accuracy for $\phi$ and $\chi$ was $1 \times 10^{-5}$ during the Runge-Kutta integration. The double integration used to calculate the $F(\rho)$ points was performed using Rhomberg integration [Press, 1989], with an attempted fractional accuracy of $1 \times 10^{-5}$ for both the inner and outer integrations. A test solution using an $F(\rho)$ curve equal to one was done, corresponding to a 2-dimensional exciton. The resulting binding energy should be,

$$E_B = \frac{\mu e^4}{8\pi^2 \epsilon_0^2 \epsilon_r^2 \hbar^2} \quad \text{, in 2 dimensions} \qquad [6.14]$$

this corresponds to 11.09 meV for $In_{.124}Ga_{.876}As$, when the integration result is 11.03 meV. The 0.05 meV discrepancy is mainly because of the incorrect boundary condition $\phi'_{e\text{-}h}(\rho = 0) = 0$ for the 2-D case. The potential $V(\rho)$ in our real calculations is very smooth near zero radius, and the solution is much easier to calculate than the 2-dimensional case. The fractional stability of the actual energies to small changes in the wavefunctions or integration limits is excellent (about $1 \times 10^{-6}$), but the 2-dimensional energy solution is not very stable. We therefore believe that an accuracy estimate of 0.01 meV for the material band-edge binding energies is conservative. Figure 6.2 shows the wavefunction solutions for material 'B' at different transverse electric field. The solutions with a higher binding energy have a larger amplitude at $\rho = 0$. The probability density per unit radial increment is then given in Figure 6.3 for the same exciton solutions. The peak maximum, corresponding to the most probable radius of occupation, shifts to larger radius as the field is increased and the binding energy drops.

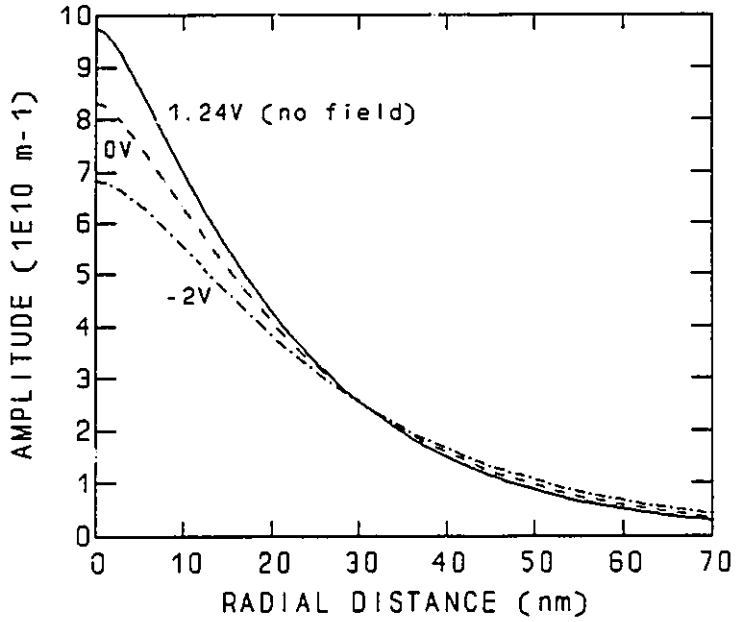


**Figure 6.2** The radial wavefunction amplitude $\phi(\rho)$ vs. radial electron-hole separation $\rho$ for three different voltages applied to material 'B'.

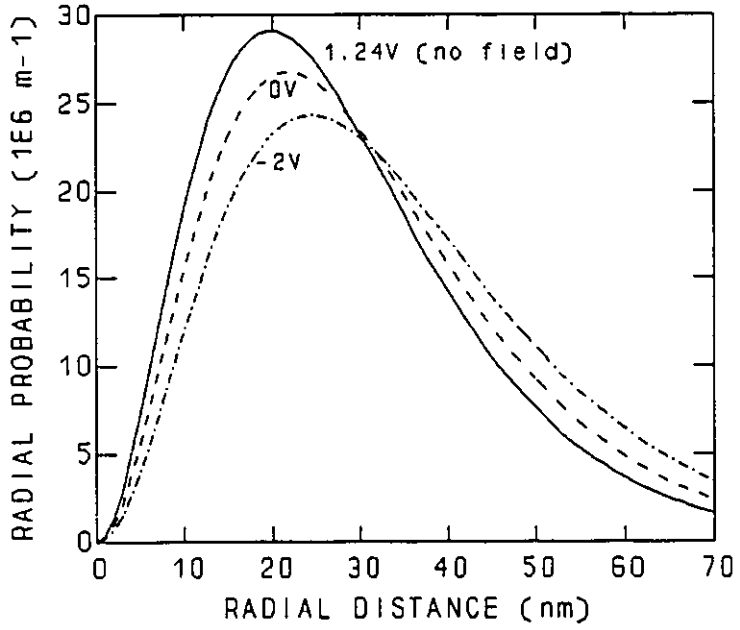


**Figure 6.3** The probability density $2\pi\rho\phi(\rho)^2$ per unit radial increment vs. radial separation $\rho$ for three voltage applied to material 'B'.

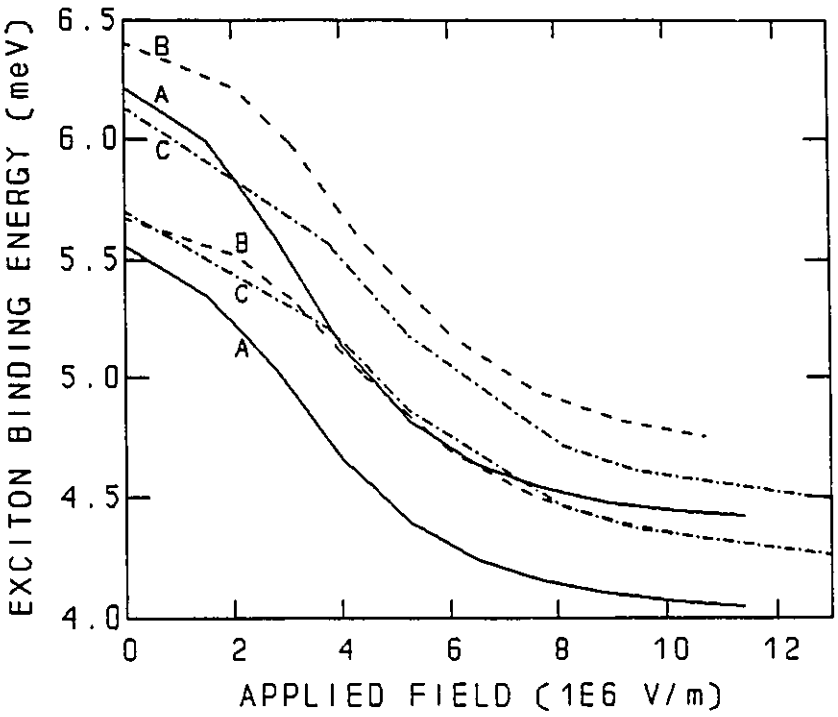


**Figure 6.4** Binding energies vs. electric field for the three material growths. The upper curve for each growth corresponds to use of the calculated hole mass, while the lower curve is for an assumed mass of $.09m_0$.

The calculated binding energies vs. field for all three materials are shown in Figure 6.4. The upper curve for each material shows the results using the parallel hole masses calculated in Chapter 5. These were $0.15m_0$ for materials A and B, and $0.12m_0$ for material C. The lower curve for each material shows the binding-energy results without including the effects of valence-band mixing. In the case of the lower curves, we have calculated a weighted hole effective mass $m_{h\|}^*$ for the different layers.

$$\frac{1}{m_{h\|}^*} = \frac{1}{m_0}\sum_{n=1}^{s}\frac{1}{(\gamma_1+\gamma_2)_n}\int_{layer\,n}|\psi_h(z_h)|^2 dz_h \qquad [6.15]$$

This effective mass value in material 'B' ranges from $0.0892m_0$ at zero field to

$0.093m_0$ at $1.5x10^7$ V/m. The inclusion of this field-dependent mass reduces the binding energy change with field in the lower curves of Fig. 6.4. However, it is clear that the absolute binding energies of the upper curves are going to be more accurate.

## 6.4 Excitons in MQWs and Superlattices

We have been approximating the multiple quantum well materials as if they were composed of single uncoupled wells. Part of the justification for this is that in a comparison of the calculated energies with and without coupling, only small differences were observed at any field (at most 1.5 meV). One also notices that the wavefunctions are considerably localized to a single well when electric field is applied. We would, however, like to develop a method for calculating excitons in coupled well situations, especially at low field, and would like to see if any exciton differences exist when well-coupling is included in our materials. To do this, one can calculate all of the energy solutions within a certain energy range for the multiple-well system, and use a variational mixing method to solve for the final wavefunction and binding energy. The exciton calculation methods used previously still apply, but instead of $\phi_e(z_e)$ and $\phi_h(z_h)$ being eigenfunctions of the no-Coulomb one-dimensional Schrodinger calculations, they will be mixtures of these eigenfunctions. It might not be strictly correct to call $E_B$ the binding energy in this case, but we will anyway.

Because the heavy-holes have less dispersion than the electrons in our materials, any effects of coupling will first show up in the conduction band. This allows us to approximate the hole wavefunction by the solution to a single well. Since we don't expect a large effect due to well coupling, we will approximate the *z*-direction electron wavefunction $\psi_e(z_e)$ as a mixture of the three lowest energy solutions to a three well calculation. Because the wavefunction is no longer an

eigenfunction of the Hamiltonian, one must use a variational method to minimize the total energy. The true energy $E$ is derived by minimizing the value $P$ given by,

$$E_{tot} \leq P = \int_{z_{low}}^{z_{high}} \psi^* H \psi \, dz \qquad [6.16]$$

Here $\psi$ is the entire exciton wavefunction, and $H$ is the entire Hamiltonian. Once the z-direction electron wavefunctions are chosen, the radial energy component $E_B$ of the value $P$ can be calculated using the previously mentioned method (of sections 6.2 and 6.3). The $z$-direction hole wavefunction is still an eigenfunction with energy $E_{z,hole}$. The $z$-direction component of $P$ is derived by one-dimensional Rhomberg integration using the following equation (derived using identities and Gauss' theorem):

$$P - E_B - E_{z,hole} = \int_{z_{low}}^{z_{high}} \left[ \frac{\hbar^2}{2m^*_{n,e}} \psi_e^{*\prime} \psi_e^{\prime} + (V_n + eFz) \psi_e^* \psi_e \right] dz_e - \frac{\hbar^2}{2m^*_{n,e}} \left[ \psi_e^* \psi_e^{\prime} \right]_{z_{low}}^{z_{high}} \qquad [6.17]$$

Because the integral is discontinuous at the boundaries between different effective mass materials, one should perform separate integrations on each constituent layer, and add the results. The mixing parameters between the electron eigenfunctions are guessed at initially, and are then found by performing a parabolic minimization of $P$ in multi-dimensions [Press, 1989]. One mixing coefficient is kept fixed, and the other two are the variable parameters. Of course the final resulting $z$-direction electron wavefunction is then normalized by multiplying all mixing coefficients by an appropriate constant.

The electron potential, the energy solutions, and the $z$-direction wavefunctions for the three-well approximation of material B is given in Figure 6.5. The applied field is $5 \times 10^4$ V/m. The three lowest energy wavefunctions shown were mixed, and

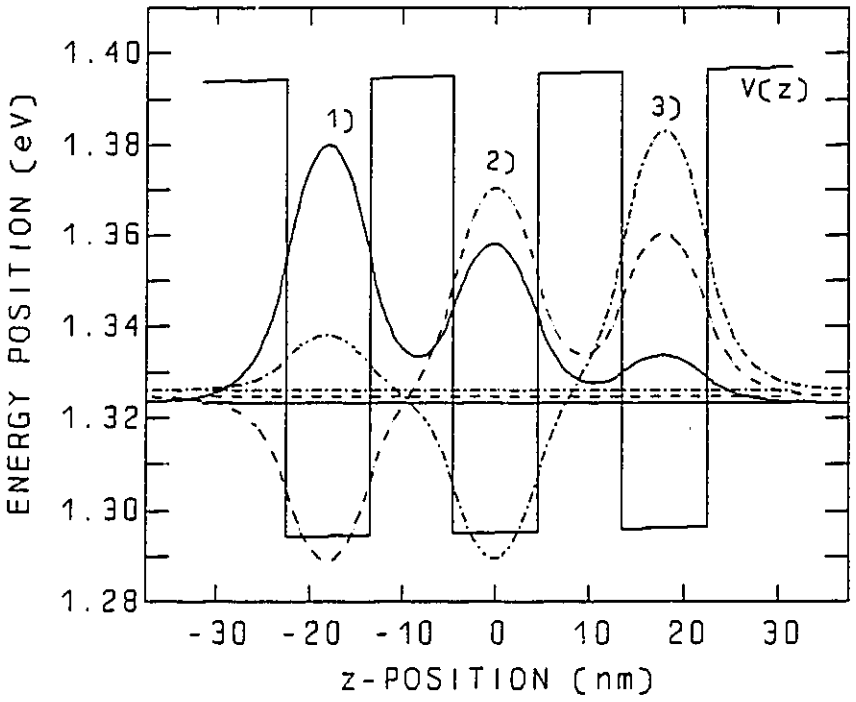


**Figure 6.5** A three-well conduction-band potential $V(z)$, the three lowest electron energies (horizontal lines), and the three corresponding wavefunctions numbered 1) to 3). The situation is for material 'B'.

the resulting total energy was minimized by using Eqn. 6.16 and Eqn. 6.17. The resulting z-direction wavefunction is shown in Figure 6.6. It is clear that the Coulomb potential mixes the three low-field, lowest energy solutions such that the wavefunction is approximately the same as that for a single quantum well. At higher fields, the wavefunction in a multiple-well structure is localized to a single well simply due to the electric-field perturbation. This indicates that it is valid to assume a single-well approximation when calculating the electro-absorption in the three material structures. For material structures with thinner barriers or shallower wells, it may be necessary to use these mixing calculations. In those cases one has to worry about more than one exciton solution at non-zero fields. There will, in fact be many

different transitions between Stark-localized states [Mendez, 1990].

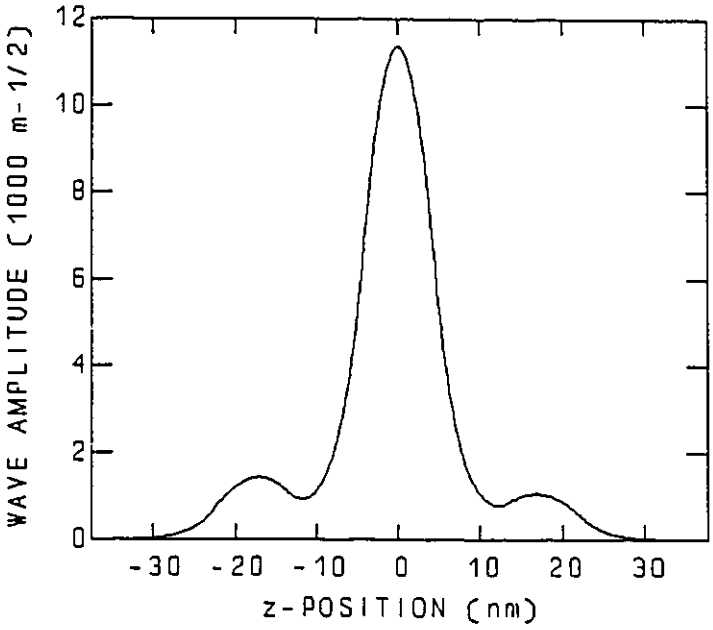


**Figure 6.6** The z-direction electron wavefunction resulting from mixing the energy solutions 1),2), and 3) of Figure 6.5 with the inclusion of a Coulomb potential. The mixing coefficients are .6401, .6483, -.4123.

## 6.5 Conclusions

The method of Wu [Wu, 1989] has been used to calculate exciton solutions in the presence of electric fields. We have extended his method to work for coupled multiple-well excitons. We determined, however, that it is sufficient to use a single-well approximation for our three material growths. The binding energy is seen to decrease with applied electric field, as the electrons and holes become separated. The wavefunction and binding-energy solutions calculated in this chapter will be used in the next chapter to model the band-edge changes with electric field.

# CHAPTER 7

## Theoretical Band-Edge Absorption Shapes

### 7.1 Introduction

In this chapter, the theoretical band-edge shapes are calculated for various electric fields. These are then compared to experiment. The results of the previous energy, wavefunction, and exciton solutions will be used, but one also needs to determine the magnitude of the factors which cause broadening of the lowest energy exciton. One also needs to calculate the strengths of the band-edge exciton and the free-carrier continuum. At high fields (greater than $1x10^7$ V/m), it is not sufficient to approximate the edge as a single broadened transition, so a Franz-Keldysh [Franz, 1958] [Aspnes, 1966] type of calculation is used to calculate these situations.

### 7.2 Absorption Strength and Broadening

We separate the broadening into a Gaussian linewidth $\Delta_G$ and a Lorentzian linewidth $\Delta_L$. These can be further broken down into components:

$$\Delta_G^2 = \Delta_{mater}^2 + \Delta_{well}^2 \qquad [7.1]$$

$$\Delta_L = \Delta_{tunn} + \Delta_{phon} \qquad [7.2]$$

The term $\Delta_{mater}$ we define as all those broadening factors which are not related to lifetime or well width variations [Ogale, 1987] [Sugawara, 1988]. A value of 4 meV

is assigned to this, which is typical of low-field exciton widths reported for best quality material [Hunt, 1988b]. The term $\Delta_{well}$ is defined as the broadening due to well width variations. Fig. 7.1 shows a calculation of the broadening caused by a one-monolayer difference $\Delta z$ in well widths for different fields. Note how the broadening asymptotically approaches the dashed line $|eF\Delta z|$ ($\Delta z$ = 2.82 Å = one monolayer). The well broadening, then, must be scaled with field according to the curve shown. Also present will be broadening due to local variations in field due to non-uniform doping, and due to residual doping in the intrinsic region. This field variation has been ignored, however. The Lorentzian broadening term $\Delta_{tunn}$ is due to tunnelling of the wavefunction out of the well due to field, and is the sum of the

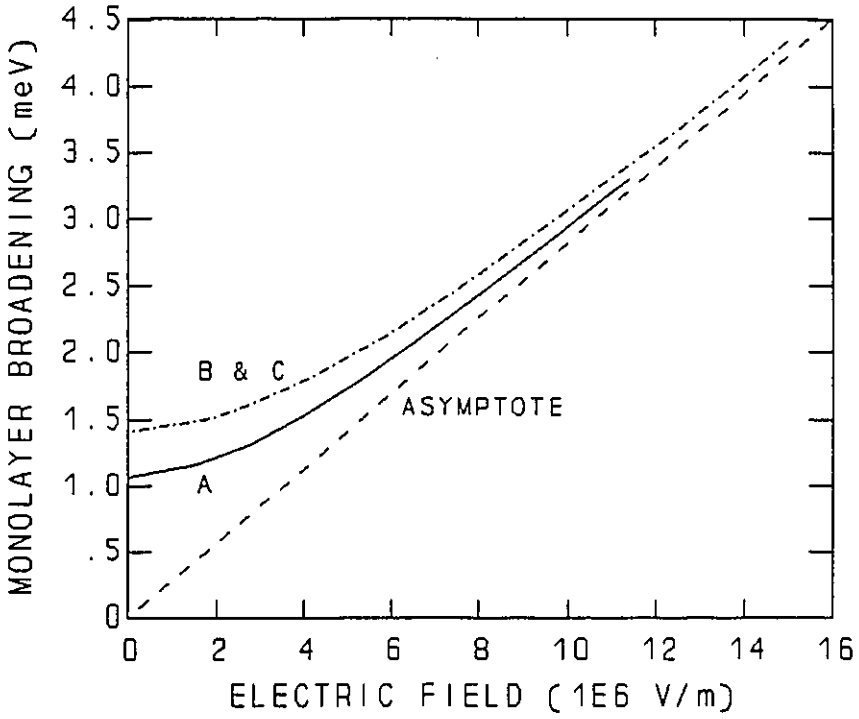


**Figure 7.1** The broadening caused by a one monolayer variation, $\Delta z$ for the three materials. At high field, these curves approach the approximate asymptote $\Delta E = |eF\Delta z|$.

calculated broadening of the electron and hole energies. The other Lorentzian term $\Delta_{phon}$ is due to phonon-induced ionization of the exciton. We have used a phonon broadening value from Rudin et al. [Rudin, 1990], scaled to 295K (giving 3.7 meV). Although their calculations are for an AlGaAs-GaAs quantum well with infinite barriers, they also use a parallel hole mass of $0.15m_0$, so the results should be applicable to our situation. Rudin and Reinecke [Rudin, 1988] also found that there was very little change in this broadening with field. Coffey [Coffey, 1989] calculated phonon scattering results for an InGaAs-GaAs quantum-well, with inclusion of finite potential barriers, and did find an extra broadening with field. The broadening values were still around 4 meV, however.

The absorption strength of the exciton can be expressed as,

$$\alpha_{exciton} \propto |\langle\psi_e|\psi_h\rangle|^2 \; |\phi_{e-h}(\rho=0)|^2 \qquad [7.3]$$

This means that the integrated strength of the absorption peak is proportional to the square of the electron-hole wavefunction overlap. It is also proportional to the number of allowed excitonic states per unit area, which is proportional to the square of the radial part of the normalized excitonic wavefunction at $\rho = 0$. Values for these parameters are found in Tables 7.1-7.3. Tables 7.1-7.3 also show the transition strengths and broadening parameters for different bias voltages on the three material growths.

In order to reproduce a theoretical absorption curve, one must realize that the E-field-broadened 2-dimensional continuum of states, as well as broadened higher energy transitions will add to the lowest energy exciton absorption peak. As the exciton peak weakens, these become increasingly important. We have included this effect by adding a broadened 2-D continuum step to the exciton peak. Since this continuum is not as affected by Coulomb effects as much as is the exciton, its

**Table 7.1** Material 'A' broadening parameters and absorption strength parameters for various applied fields

| **Material A, L=800nm** | | | | |
|---|---|---|---|---|
| | **0V Bias** | **-2V Bias** | **-4V Bias** | **-6V Bias** |
| Field ($10^6$ V/m) | 1.54 | 4.03 | 6.50 | 8.97 |
| $\lvert\langle\psi_e\lvert\psi_h\rangle\rvert^2$ | 0.862 | 0.488 | 0.253 | 0.150 |
| $\lvert\phi(\rho=0)/\phi_{F=0}\rvert^2$ | 0.924 | 0.643 | 0.502 | 0.455 |
| $\Delta_G$ (meV) | 10.4 | 13.3 | 17.5 | 22.5 |
| $\Delta_{mater}$ (meV) | 4.0 | 4.0 | 4.0 | 4.0 |
| $\Delta_{well}$ (meV) | 9.6 | 12.7 | 17.0 | 22.1 |
| $\Delta_L$ (meV) | 3.7 | 4.8 | 7.6 | 20.1 |
| $\Delta_{tunn}$ (meV) | 0.0 | 1.06 | 3.9 | 16.4 |
| $\Delta_{phon}$ (meV) | 3.7 | 3.7 | 3.7 | 3.7 |
| $\kappa$ ($cm^{-1}$) | 5480 | 5480 | 5480 | 5480 |
| $\xi$ (meV) | 19.6 | 19.6 | 19.6 | 19.6 |

**Table 7.2** Material 'B' broadening parameters and absorption strength parameters for various applied fields.

| **Material B, L=90nm** | | | |
|---|---|---|---|
| | **0V Bias** | **-1V Bias** | **-2V Bias** |
| Field ($10^6$ V/m) | 4.25 | 7.52 | 10.61 |
| $\lvert\langle\psi_e\lvert\psi_h\rangle\rvert^2$ | 0.598 | 0.305 | 0.183 |
| $\lvert\phi(\rho=0)/\phi_{F=0}\rvert^2$ | 0.726 | 0.531 | 0.488 |
| $\Delta_G$ (meV) | 11.2 | 14.7 | 18.8 |
| $\Delta_{mater}$ (meV) | 4.0 | 4.0 | 4.0 |
| $\Delta_{well}$ (meV) | 10.5 | 14.1 | 18.4 |
| $\Delta_L$ (meV) | 4.1 | 9.4 | 19.6 |
| $\Delta_{tunn}$ (meV) | 0.4 | 5.7 | 15.9 |
| $\Delta_{phon}$ (meV) | 3.7 | 3.7 | 3.7 |
| $\kappa$ ($cm^{-1}$) | 7370 | 7370 | 7370 |
| $\xi$ (meV) | 18.4 | 18.4 | 18.4 |

absorption strength is considered to be affected only by the square of the

wavefunction overlap. In a crude approximation (assuming constant effective mass with energy), the continuum is a broadened Heaviside function $H$ which starts at one binding energy above the exciton peak energy. The Heaviside function is defined as,

$$H(\zeta) = \begin{cases} 0, & \zeta<0 \\ 1, & \zeta\geq 0 \end{cases} \qquad [7.4]$$

**Table 7.3** Material 'C' broadening parameters and absorption strength parameters for various applied fields.

| **Material C, L=54nm** | | | | |
|---|---|---|---|---|
| | **0.8V Bias** | **0V Bias** | **-0.5V Bias** | **-1V Bias** |
| Field ($10^6$ V/m) | 3.76 | 9.45 | 12.7 | 15.76 |
| $\lvert\langle\psi_e\lvert\psi_h\rangle\rvert^2$ | 0.683 | 0.230 | 0.142 | 0.099 |
| $\lvert\phi(\rho=0)/\phi_{F=0}\rvert^2$ | 0.804 | 0.508 | 0.473 | 0.461 |
| $\Delta_G$ (meV) | 9.2 | 14.4 | 18.1 | 22.0 |
| $\Delta_{mater}$ (meV) | 4.0 | 4.0 | 4.0 | 4.0 |
| $\Delta_{well}$ (meV) | 8.3 | 13.9 | 17.6 | 21.6 |
| $\Delta_L$ (meV) | 3.77 | 13.5 | 25.1 | 42.8 |
| $\Delta_{tunn}$ (meV) | 0.07 | 9.8 | 21.4 | 39.1 |
| $\Delta_{phon}$ (meV) | 3.7 | 3.7 | 3.7 | 3.7 |
| $\kappa$ ($cm^{-1}$) | 8890 | 8890 | 8890 | 8890 |
| $\xi$ (meV) | 14.8 | 14.8 | 14.8 | 14.8 |

We allow this continuum to be convolved with the same broadening function as is the exciton peak. This broadening function $\Gamma(E)$ is a convolution of Gaussian and Lorentzian lineshapes, which can be related to the Voigt function[23] $K(x,y)$.

$$K(x,y) = \frac{y}{\pi}\int_{-\infty}^{\infty}\frac{e^{-t^2}}{y^2+(x-t)^2}dt \qquad [7.5]$$

$$\Gamma(E) = \frac{2\sqrt{ln2}}{\sqrt{\pi}\Delta_G} K\left(\frac{2E\sqrt{ln2}}{\Delta_G}, \frac{\Delta_L\sqrt{ln2}}{\Delta_G}\right) \qquad [7.6]$$

We evaluate the Voigt function using the rational approximation of Hui et al. [Hui, 1978]. In mathematical form, then, the non-broadened absorption $\alpha_{nb}$ is given by,

$$\alpha_{nb}(h\nu) = \kappa|\langle\psi_e|\psi_h\rangle|^2\left[H(h\nu - E_{e1} + E_{hh1}) + \xi\,\delta(h\nu - E_{e1} + E_{hh1} + E_B)\left(\frac{\phi(\rho=0)}{\phi_{F=0}(\rho=0)}\right)^2\right] \qquad [7.7]$$

Here $\kappa$ and $\xi$ are constants which are dependent on the material. They are set as fitting parameters, controlling the absorption coefficients of the continuum and the exciton feature. Values are given in Tables 7.1-7.3. $E_B$ is the binding energy, $E_{e1}$ and $E_{hh1}$ are the first electron and heavy-hole energies, measured in terms of absolute electron potential, and $h\nu$ is the photon energy. The value $\phi_{F=0}(\rho=0)$ is the value of the radial portion of the exciton wavefunction for zero applied electric field at $\rho=0$. This function $\alpha_{nb}(h\nu)$ becomes $\alpha_{broad}(h\nu)$ when convolved with the broadening function $\Gamma(E)$:

$$\alpha_{broad}(h\nu) = \int_{-\infty}^{\infty} \alpha_{nb}(h\nu - E)\Gamma(E)\,dE \qquad [7.8]$$

Convolution with the Heaviside function was done numerically. The final transmission curve (ignoring reflections) is given by a standard exponential absorption formula,

$$Trans = \exp(-\alpha_{broad}L) \qquad [7.9]$$

Here L is the length of material that the wave passes through (given in Tables 7.1-7.3).

## 7.3 Theoretical vs. Experimental Absorption Shapes

Figures 7.2, 7.3, and 7.4 shows a comparison of theory vs. experiment for transverse transmission spectra for different biases in the three materials. In order to calculate the theoretical curves, the absolute exciton strength and 2-D continuum strength (determined by $\xi$ and $\kappa$), and total Gaussian broadening $\Delta_G$ were manual fitting parameters for the lowest-field curve each comparison figure. In materials 'A' and 'B', this fitting was done on the 0V curve, while for material 'C' fitting was done to the 0.8V curve. Once these parameters were set, the other bias-voltage curves were determined with no adjustable parameters.

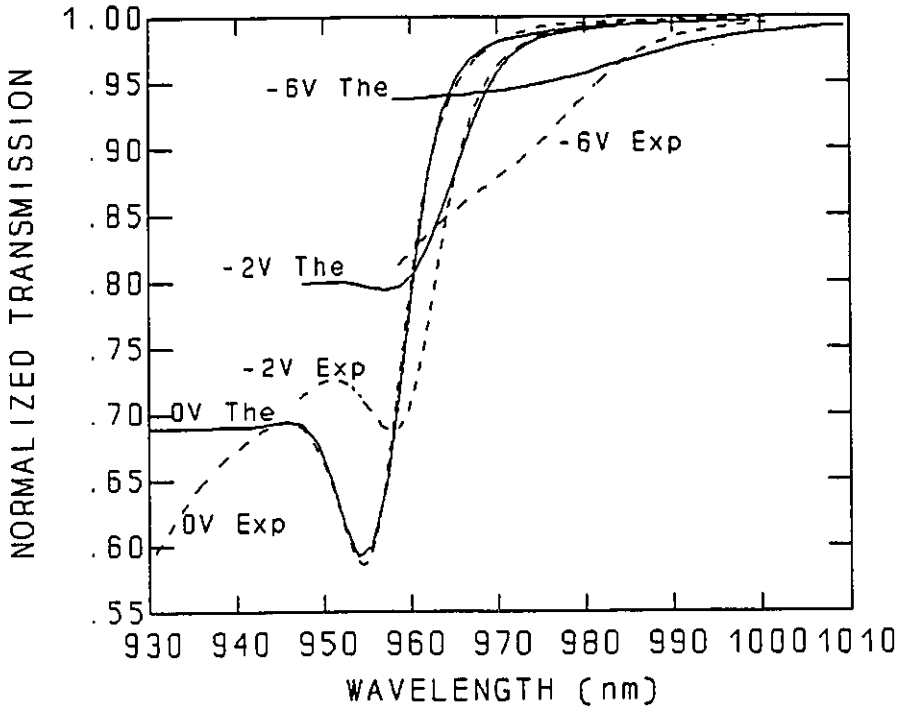


**Figure 7.2** Theoretical and experimental transverse transmission spectra for material 'A'. The 0V-bias curves are matched by using adjustable parameters.

Our main interest in doing these calculations is to be able to predict the absorption coefficients in the long wavelength band tails, at wavelengths which will

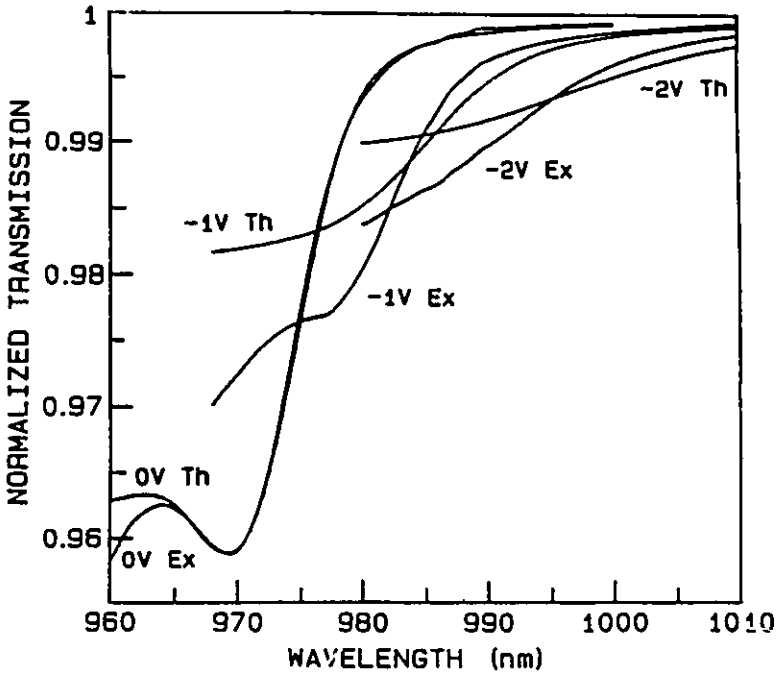


**Figure 7.3** Theoretical and experimental transverse transmission spectra for material 'B'. The 0V-bias curves are matched using some theoretical fitting parameters.

be used for waveguide modulators. The fit of the theoretical curve to experimental at 0V bias is very good in the band tail. This would indicate that the Lorentzian-shaped phonon-induced broadening predicted by Rudin et al. [Rudin, 1990] is close to accurate for our materials. In the long wavelength band-tail, the reverse-bias theoretical and experimental absorption spectra are also quite close. The absorption coefficients at the centre of the exciton peaks do not compare as well, however.

One result of the comparison is that the theory predicts a more rapid reduction in the exciton absorption with electric field than is observed experimentally. A similar discrepancy was seen by Coffey [Coffey, 1988]. This result was especially clear at low fields in this material and similar structures. This can be partly

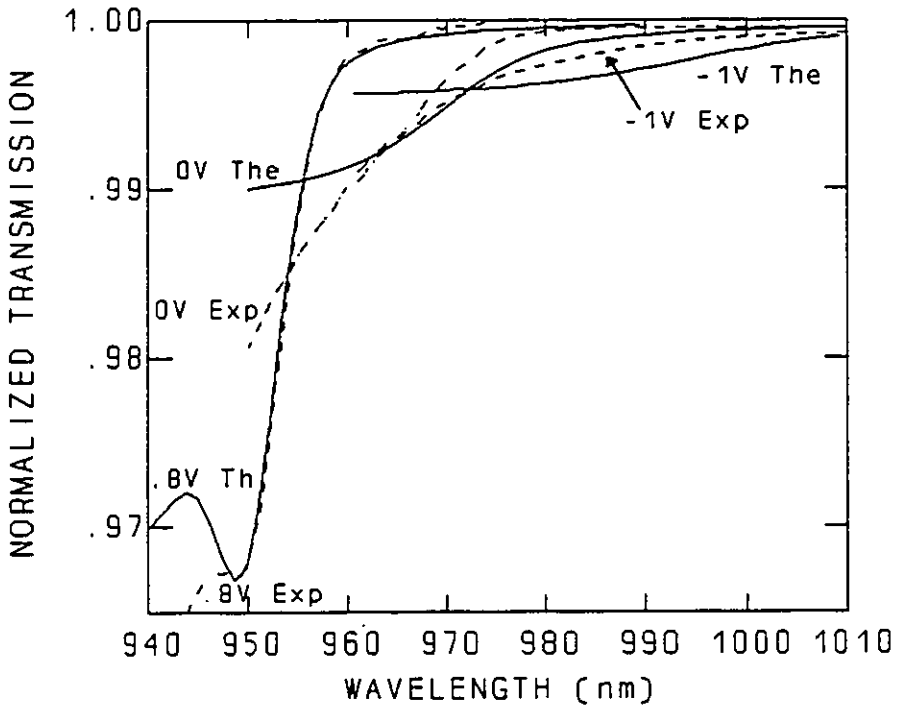


**Figure 7.4** Theoretical and experimental transverse transmission spectra for material 'C'. The 0.8V-bias spectra are matched by using some adjustable theoretical parameters.

attributed to our neglecting the effect of the Coulomb potential on the wavefunctions in the $z$-direction (growth direction). This Coulomb potential would inhibit the electron and hole wavefunctions from separating to any large degree under low fields. To partially account for this, one could multiply the wavefunction by a variational term $\exp[-\beta|(z_e-z_h)|]$. By combining our binding energy solution method with a one-parameter (given by $\beta$) energy minimization, one could possibly improve the results. However, because a new form factor curve $F(\rho)$ must be calculated for each $\beta$-value, this is much more computation intensive. Instead of using a wavefunction form separable in $z$ and $\rho$, one might assume a two-parameter electron-hole interaction term $\phi_{e\text{-}h} = \exp\{-[\xi(z_e-z_h)^2+\beta\rho^2]^{1/2}\}$. One would then perform a two-parameter

energy minimization only. It is not clear how well this form will work for high fields, however.

Another factor causing the theoretical peak strengths to be less than experiment, especially at high fields, is our neglect of higher energy transitions in the absorption spectrum. It is clear that the absorption to higher energy than the exciton is not a broadened constant 2-D continuum, but rather increases sharply with increasing photon energy. Light hole excitons, hole-band non-parabolicity, excitons and transitions involving higher order wavefunction solutions, and transitions to the 3-D continuum all contribute to the experimentally observed absorption. For non-zero fields, previously forbidden sub-band transitions become allowed (such as e1-hh2), and contribute to absorption just above the band edge. At higher fields, as the e1-hh1 band-edge exciton weakens and broadens, the influence of these higher energy features on the shape of the band-edge become increasingly important. At very high fields, such as that at -8V bias, there are no pseudo-bound states, and one must think of the edge as a continuum of states. In the intermediate fields, these higher energy states are still important. It should also be noted that there is considerable uncertainty in many of the parameters used [Hunt, 1988a], and in the resulting band offsets between the constituent layers. The larger theoretical peak shifts compared to experiment may partly be due to our assumption of a single broadened feature.

## 7.4 Theoretical Absorption Calculations at High Fields

At high fields, it is no longer accurate to consider the band-edge as a single broadened exciton solution, plus a broadened step-edge. It is better to consider the band edge as a continuum of different transitions, which can be calculated by the

method of Appendix B. The method is similar to a Franz-Keldysh [Keldysh, 1966] calculation, but implemented for a quantum-well instead of a bulk material. The exciton binding is not strong at high fields, and while it is not correct to ignore the exciton, we will do so anyway. By neglecting the reduction in the strength of the Coulomb-enhanced free-carrier transitions with field, we may be creating a counteracting error.

As given in Appendix B, and adding the proportionality constant $\kappa$ introduced earlier in this chapter, one gets for the band-edge absorption (ignoring excitons),

$$\alpha_{nb}(h\nu) = \kappa \int\int N_e^2 N_h^2 \left|\langle \psi_e | \psi_h \rangle\right|^2 g_{ze}(E_e) g_{zh}(E_h) H(E_e - E_h - h\nu) dE_e dE_h \quad [7.10]$$

Here $H$ is the Heaviside function, $g_{ze}$ and $g_{zh}$ are density of states functions defined in appendix B, $N_e$ and $N_h$ are normalization constants, and $E_e$ and $E_h$ are the electron and hole energies (in terms of electron potential). The integral is actually calculated as a sum of discrete energy transitions. Wavefunctions were calculated for 50 electron and 50 hole energies for a sufficient range around the first solution energy for a probability resonance within the conduction or valence-band well. The absorption due to all 2500 possible transitions were summed. The resulting curve was then convolved with the broadening function $\Gamma$. However, this time one does not include the Lorentzian broadening due to tunnelling from the well, since it is included in the resulting curve. Also, the Gaussian broadening due to well-width variations may need to be modified at high fields.

To properly calculate broadening due to well-width variations at high field, one should really calculate absorption spectra for each monolayer of well-width change across the entire range of variation. The spectra would then be weighted according to some Gaussian probability of well thickness (such that the weights add to one). For wide or shallow wells at high field, the real broadening using this

**Table 7.4** The broadening parameters for the three materials at various high fields.

| **Material A** | **-6V** | **-10V** | **-15V** |
|---|---|---|---|
| Field ($10^6$ V/m) | 8.97 | 13.9 | 19.9 |
| $eF\delta z_{well}$ (meV) | 20.9 | 31.9 | 46.4 |
| $eF\delta z_{stren}$ (meV) | 28.7 | 31.5 | 33.8 |
| $\Delta_{well}$ (meV) | 16.9 | 22.4 | 27.3 |
| $\Delta_G$ (meV) | 17.4 | 22.8 | 27.6 |
| $\Delta_L$ (meV) | 3.7 | 3.7 | 3.7 |
| | | | |
| **Material B** | **-2V** | **-5V** | **-8V** |
| Field ($10_6$ V/m) | 10.7 | 19.3 | 26.9 |
| $eF\delta z_{well}$ (meV) | 18.3 | 33.0 | 45.6 |
| $eF\delta z_{stren}$ (meV) | 35.3 | 40.5 | 43.0 |
| $\Delta_{well}$ (meV) | 16.2 | 25.6 | 31.3 |
| $\Delta_G$ (meV) | 16.7 | 25.9 | 31.5 |
| $\Delta_L$ (meV) | 3.7 | 3.7 | 3.7 |
| | | | |
| **Material C** | **-1V** | **-4V** | **-6V** |
| Field ($10^6$ V/m) | 15.6 | 31.5 | 40.4 |
| $eF\delta z_{well}$ (meV) | 20.9 | 42.1 | 54.0 |
| $eF\delta z_{stren}$ (meV) | 37.4 | 44.1 | 50.5 |
| $\Delta_{well}$ (meV) | 18.2 | 30.4 | 36.9 |
| $\Delta_G$ (meV) | 18.6 | 30.7 | 37.1 |
| $\Delta_L$ (meV) | 3.7 | 3.7 | 3.7 |

method will be considerably less than the formula $\Delta E = eF\Delta z$ for each monolayer variation $\Delta z$. This is because a well-width change may result in a different transition energy, but it also changes the electron-hole overlap at high fields. The changing overlap reduces the effective broadening to lower energy. Inclusion of this effect may in fact result in an apparent shift of the edge to higher energy, but we shall

ignore that. One can approximate the effect of the changing transition strength by reducing the calculated Gaussian energy broadening due to well-width variations $\Delta_{well}$. Consider a Gaussian full width $\delta z_{well}$ for the well width variation, and $\delta z_{stren}$ for twice the well-width increase required for a reduction in the square of the e1-hh1 wavefunction overlap to half.

$$\frac{1}{\Delta_{well}^2} = \frac{1}{(eF\delta z_{well})^2} + \frac{1}{(eF\delta z_{stren})^2} \qquad [7.11]$$

The final broadening includes $\Delta_{well}$, $\Delta_{mater}$, and $\Delta_{phon}$. We do not include broadening due to phonon-scattering in the $z$-direction as it is not clear what effect this would have. Therefore $\Delta_L = \Delta_{phon}$, $\Delta_G^2 = \Delta_{well}^2 + \Delta_{mater}^2$. The broadening parameters for the three materials are given in Table 7.4. The strength term in the table does reduce

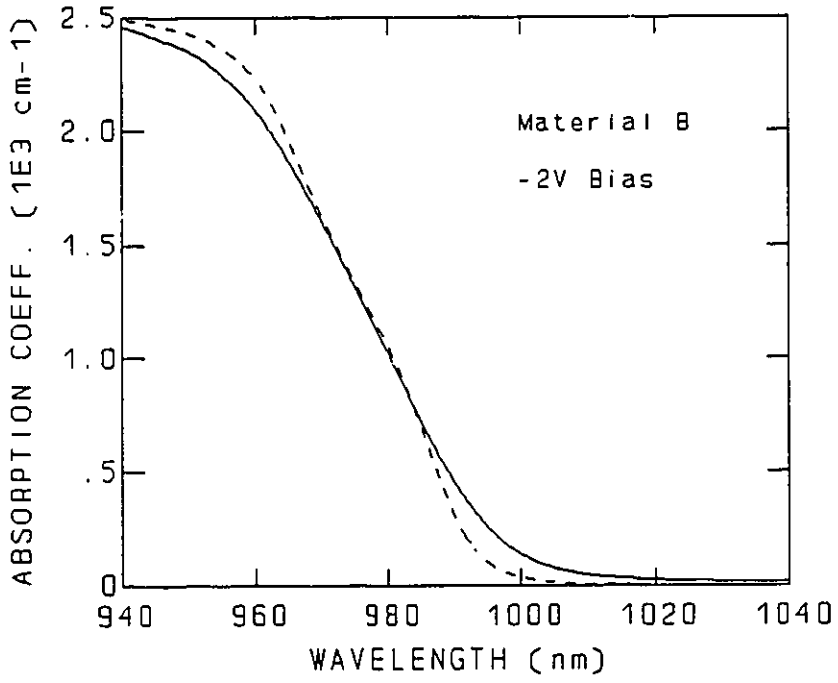


**Figure 7.5** Material 'B' theoretical absorption spectra for -2V applied bias. The dashed curve is the not-broadened spectrum, while the solid curve is the broadened absorption coefficient spectrum.

the Gaussian broadening at high fields. One can now calculate the band-edge absorption using Eqn. 7.7 and the values of $\kappa$ in Tables 7.1-7.3. Figure 7.5 shows the broadened and not-broadened band-edge absorption coefficients for material 'B' at a bias voltage of -2V. The roll over of the spectrum at short wavelength is an artifact of the calculation method. If higher energy wavefunctions had been included, the absorption would have continued to rise sharply at short-wavelength. The main effect of the broadening is to lengthen the band-tail to longer wavelength. This curve can be compared against the experimental curve, and the theoretical curve calculated in section 7.2. Figure 7.6 shows the result. The theoretical curve (b), calculated by

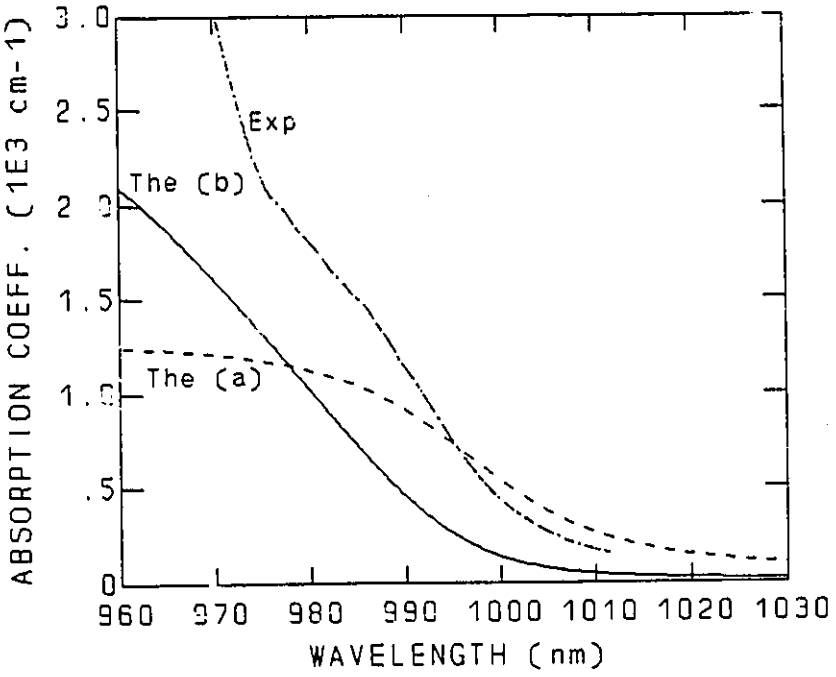


**Figure 7.6** Material 'B' Experimental absorption coefficient spectrum, and two theoretical spectra: (a) calculated as a single broadened transition, and (b) calculated as a continuum of transitions.

summing all transitions, does not extend to as long wavelength as the theoretical curve (a) calculated as a single broadened peak. This is largely due to our ignoring

excitons in the calculated curve (b). One could change the Heaviside function $H(E_e-E_h-h\nu)$ in Eqn. 7.10 to $[H(E_e-E_h-h\nu) + \xi\delta(h\nu-E_e+E_h+E_b)]$. At low field this would give the same answer as for the single broadened exciton peak, but what effect does the Coulomb attraction have on all the possible energies at high field? The Coulomb attraction between electrons and holes may very well have a different effect for each possible electron-hole transition. The deviation of theoretical curve (b) from experiment is largely due to ignoring the band-edge exciton, but it may also be due to uncertainty in the absolute strength of the transition. Here the same value of $\kappa$ was used in calculating absorption strengths as was used in section 7.2. This strength was not well defined by fitting, and it may not be valid to assume that it stays

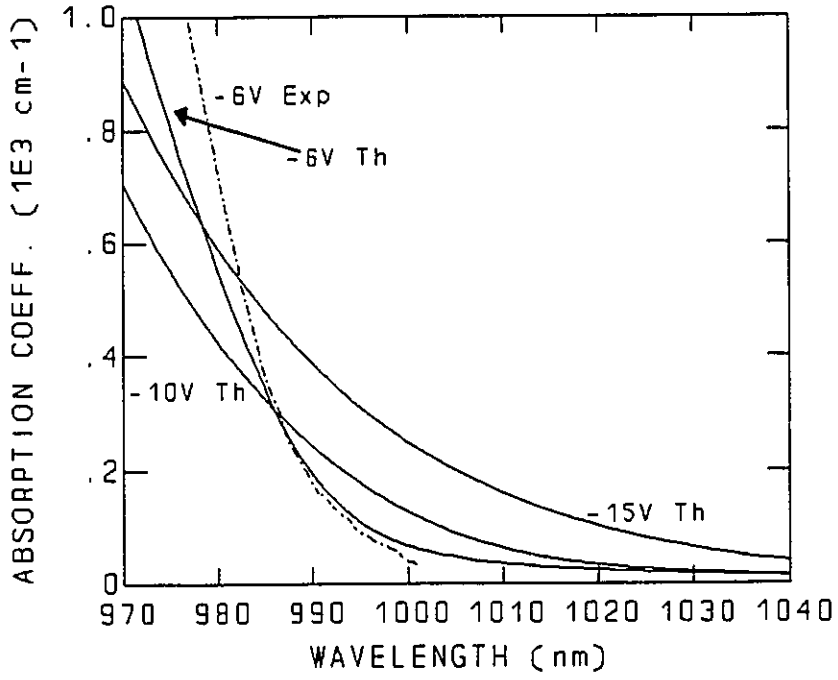


**Figure 7.7** Material 'A' theoretical and experimental high-field absorption coefficient spectra for various bias voltages. The theoretical curves were calculated by summing a continuum of transitions, ignoring excitons.

constant with field. Changing parallel effective hole mass with field is a possibility,

which would change κ. Also, valence band non-parabolicity may mean that the Heaviside function is not correct for the band-edge shape for any one transition. Therefore, uncertainties in the calculated strengths and the unknown effect of Coulomb attraction may account for the discrepancies between theory and experiment.

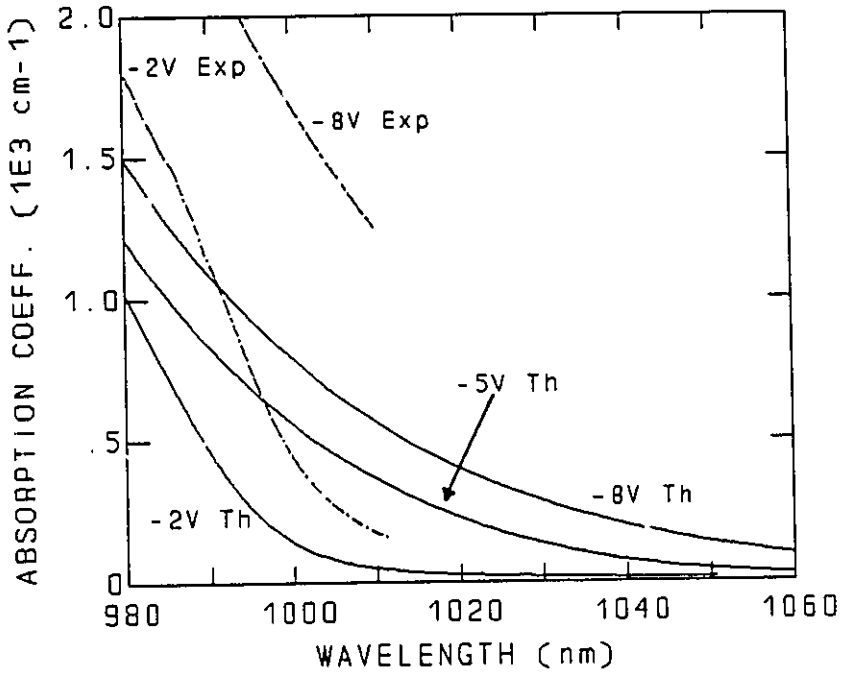


**Figure 7.8** Material 'B' theoretical and experimental high-field absorption coefficient spectra for various bias voltages. The theoretical curves were calculated by summing a continuum of transitions, ignoring excitons.

Figures 7.7, 7.8, and 7.9 show the comparison of the calculated and experimental high-field band edges for materials A, B, and C respectively. While material B shows a calculated edge at too short a wavelength, materials A and C show calculated curves correspond better to experiment. It is important not to read too much into this because of the discrepancies mentioned earlier.

While theory does not correspond exactly to experiment, the agreement is sufficient to use these high-field absorption coefficient calculations to determine the waveguiding transmission. This will be shown in the next chapter.

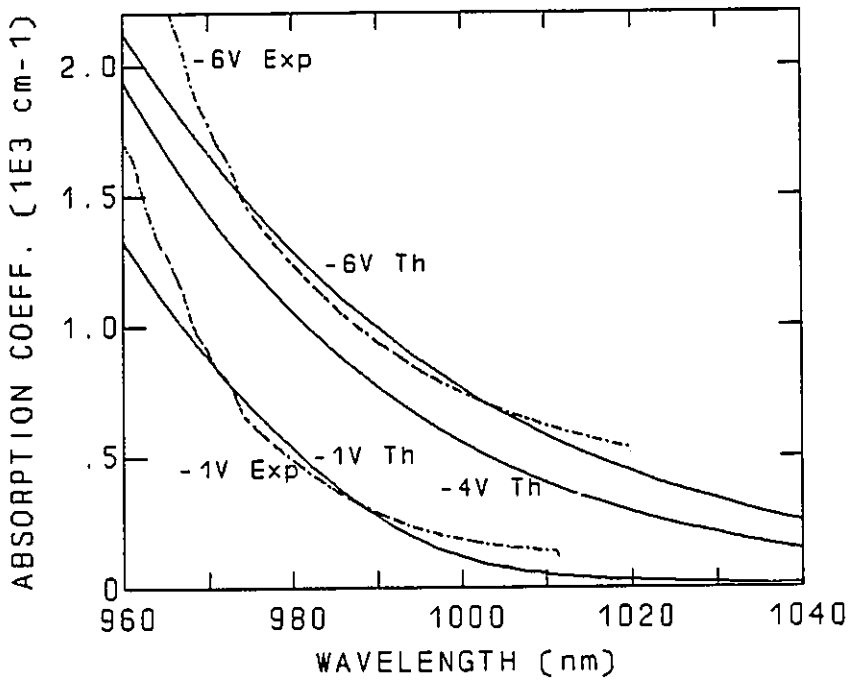


**Figure 7.9** Material 'C' theoretical and experimental high-field absorption coefficient spectra at various bias voltages. The theoretical curves were calculated by summing a continuum of transitions, ignoring excitons.

## 7.5 Conclusions

Using fitting parameters for the continuum and exciton absorption strength, as well as the Gaussian broadening due to well width variations, the low-field band-edge absorption fit well with experiment. This agreement showed the suitability of a combined Gaussian and Lorentzian shape to model the broadening, and provided evidence for a Lorentzian phonon broadening similar to the literature value of about

3.7 meV.

Theoretical absorption calculations at larger fields showed reasonable agreement to experiment in the long-wavelength band tail, but was too weak at higher photon energies due to the absence of higher well-energy solutions in the calculation. These calculations used a single broadened exciton and a single broadened continuum edge. At very high fields, this was not considered appropriate, and the edge was assumed to be a continuum of different electron-hole transitions. The agreement with experiment varied between samples due to uncertainties in the theoretical absorption strengths used and the absence of excitons in the calculation.

# CHAPTER 8

## Waveguiding Modulation

### 8.1 Introduction

In this chapter slab waveguiding transmission spectra will be shown for the three different materials at various bias voltages. The experimental transmission spectra will then be compared to theoretical spectra derived from the absorption coefficients calculated in Chapter 7. Rib waveguides were processed for all three materials, and the transmission and photocurrent spectra were then examined. From these spectra, conclusions will be made about modulator performance in our $In_xGa_{1-x}As$-GaAs multiple quantum-well waveguides.

### 8.2 Experimental Apparatus and Material Processing

All slab waveguiding and switching measurements done on material A were done using a monochromated white-light source. A diagram of the experimental set-up is shown in Figure 8.1. About 3 picoWatts of 2nm bandwidth light was focused into one end of a 2x2 Canstar fibre coupler using a 20x microscope objective. The fibre has a 4.5$\mu$m core, and the coupler has a measured 50% splitting wavelength of about 870nm. Light from a 1.15$\mu$m HeNe laser was focused into the other input fibre for system alignment, and was turned off during actual measurements. One output fibre (the fibre which contained the lowest intensity of 1.0$\mu$m monochromated light) directed light to a reference detector. The other output fibre was butt coupled

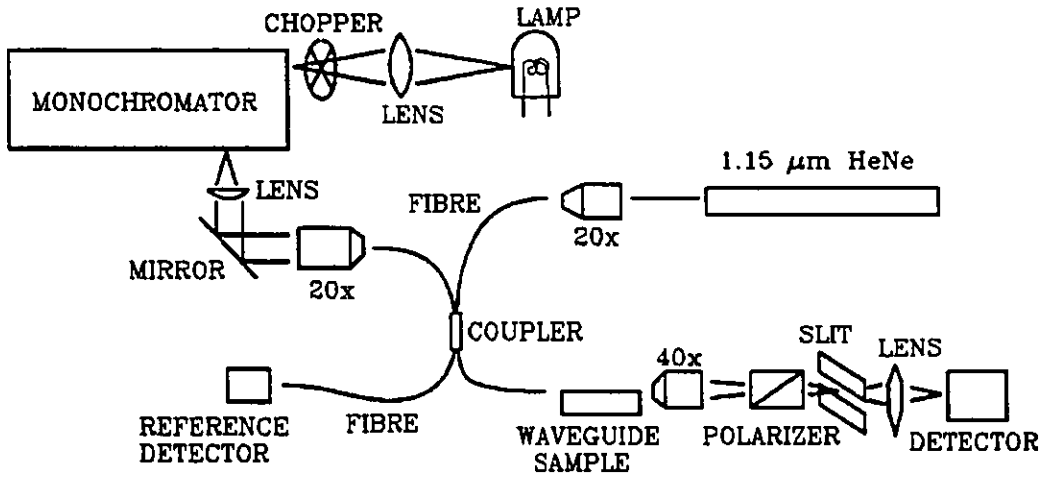


**Figure 8.1** Experimental Waveguiding Transmission set-up using a monochromated white light source. A fibre directs light to the waveguide.

to a waveguide sample using a combination of mechanical and piezo-electric positioners. The sample was sitting on the end of a very thin drill-bit to allow access to the waveguide ends. The waveguide output was collected by a 40x microscope objective, sent through a polarizer (to isolate either TE or TM light), and was focused onto a slit. The waveguiding light would pass through the slit, while stray light from the material substrate or the air would get filtered out. The waveguiding light was then focused to a silicon p-i-n photodetector, working in zero-bias mode with a 19.5MΩ current-to-voltage resistor. The photodetector circuit is found in Appendix E. Lock-in amplifiers were used to amplify the output of the detectors, and the resulting signals sent to computer. The monochromator had a motorized scan. By removing the waveguide and by measuring the relative outputs of the two detectors vs. wavelength, the system response of the coupler, lamp, and optics combination was measured. This response was used to correct the actual waveguiding measurements.

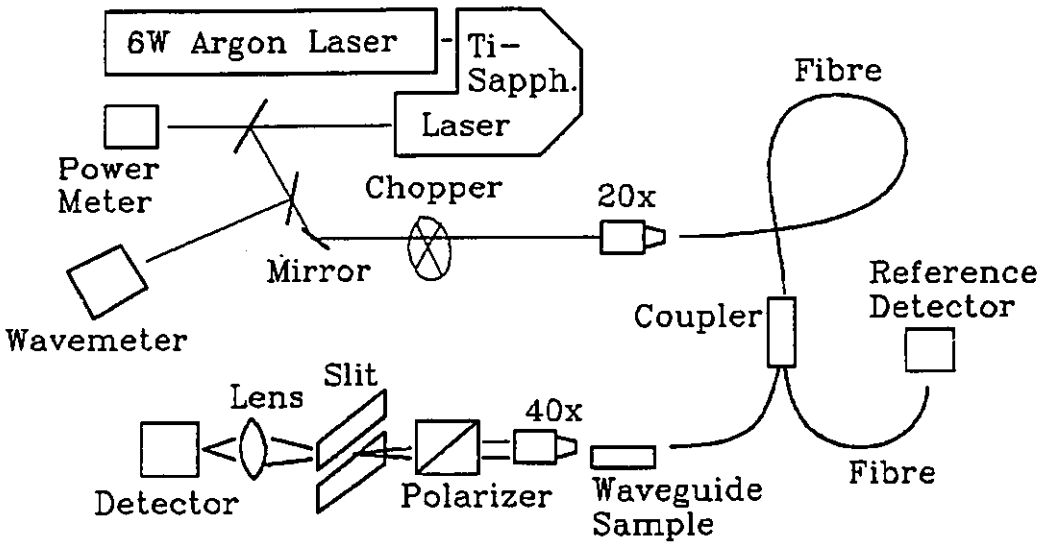


**Figure 8.2** Waveguiding transmission and photocurrent set-up using a tunable Ti-Sapphire laser as a source. A fibre directs light to the waveguide, while a reference detector records the incident intensity.

Slab waveguides of materials B and C, as well as rib waveguides made from all three materials were measured using the experimental set-up shown in Figure 8.2. The basic optical arrangement is the same as in Figure 8.1, but instead of a monochromated white light source, a Titanium-Sapphire laser was used. An additional power meter was used when maximimizing the Ti-Sapphire laser output, and a wavemeter measured the wavelength to a resolution of 0.3nm. Because the laser output varied with wavelength, and was quite noisy, the reference detector was necessary to divide out these changes. The wavelength was scanned manually, with each spectral point consisting of a computer integration of the output of the lock-in amplifiers connected to the detectors. By dividing the output of the two detectors, and later dividing by a measured system response, the final spectra were determined. Because of the manual scanning, however, the spectra do not have enough points to

make truly smooth curves. When measuring the transmission of the rib waveguides the slit in Figure 8.2 is changed to a rectangular aperture by attaching razor blades perpendicular to the slit. This was done to further eliminate non-waveguiding light.

The slab waveguide samples were cleaved from pieces processed for the transverse measurements of Chapter 3. The etched rib waveguides were processed

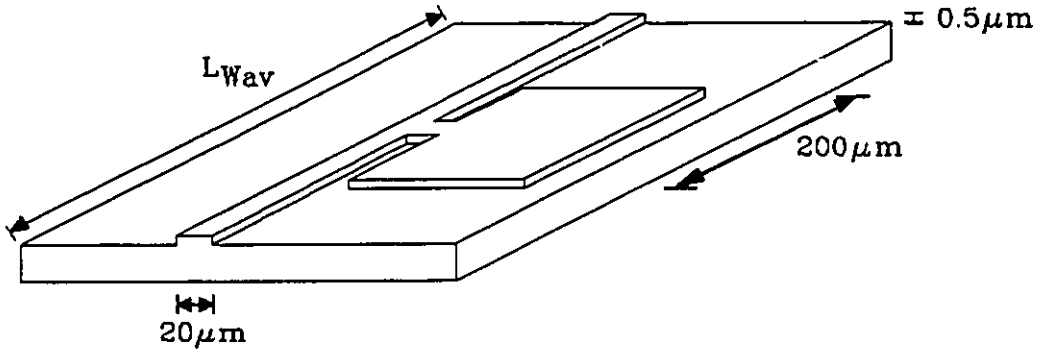


**Figure 8.3** A processed rib-waveguide, consisting of a 20$\mu$m-wide rib 0.5$\mu$m high, and a square 200$\mu$m-wide bonding pad connected to the waveguide by a 20$\mu$m-wide strip. The waveguide ends are cleaved.

with dimensions given in Figure 8.3. The substrate contact consists of electron-beam evaporated Gold-Germanium eutectic, annealed at 400C for 15 seconds. After cleaning the sample, gold was evaporated on the front side. Photoresist was then spun on, and a waveguide pattern was exposed and developed. The photoresist was hard-baked for 1 hour at 150C. A Potassium Iodide gold etch was used for about 10 seconds to remove the gold from the unwanted regions. A sulphuric acid etch was then used to etch the epilayers to a depth of 0.5$\mu$m. The etch consisted of 1 part concentrated $H_2SO_4$, 8 parts $H_2O_2$, and 80 parts $H_2O$. About 45 seconds of agitated etching was sufficient. The photoresist was removed with photoresist stripper. While it was hoped that this would result in a self-aligned gold covered waveguide, the gold peeled off from the thin waveguides during photoresist removal. On some

waveguides the gold must have lifted before the sulphuric acid etch, as the waveguides were damaged by the etch. However, some good samples were found, and the gold was not necessary for modulator operation. Gold still remained on the bonding pads, and as long as currents flowing through the devices are kept small, the sheet resistance of the upper p-doped layer should not cause a significant voltage drop.

## 8.3 Waveguiding Mode Calculations

For high speed operation, one would want a thin rib waveguide to reduce capacitance. One would also process the rib such that it was single lateral mode, and

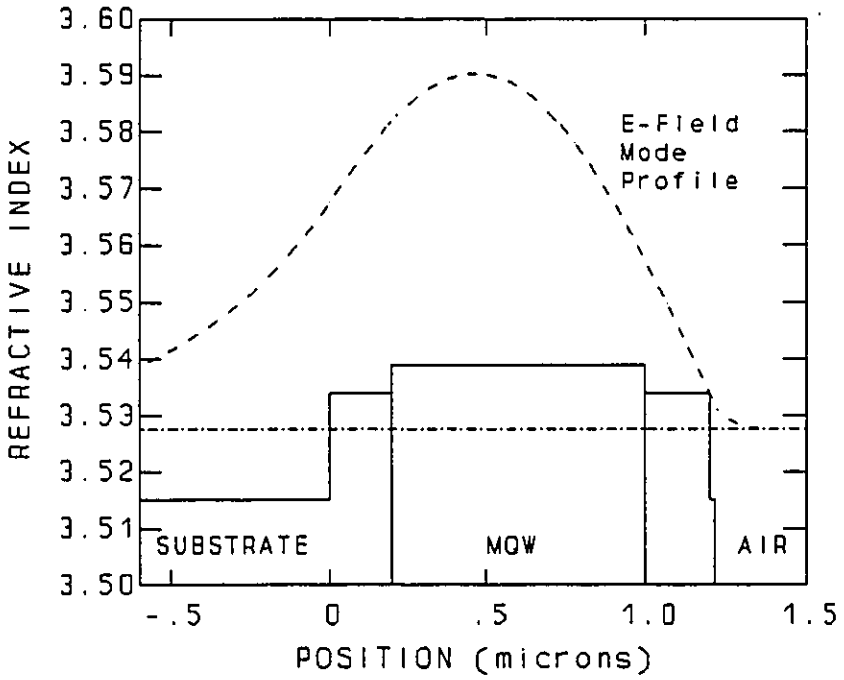


**Figure 8.4** Material 'A' slab waveguiding electric-field mode shape, effective mode index (dashed-dotted line), and refractive index profile.

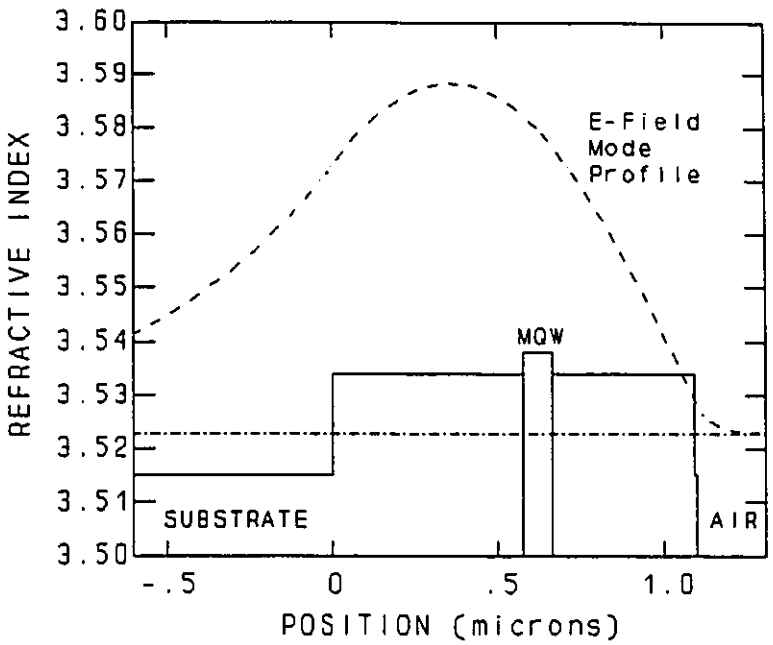


**Figure 8.5** Material 'B' slab waveguiding electric-field mode shape, effective mode index (dashed-doted line), and refractive index profile.

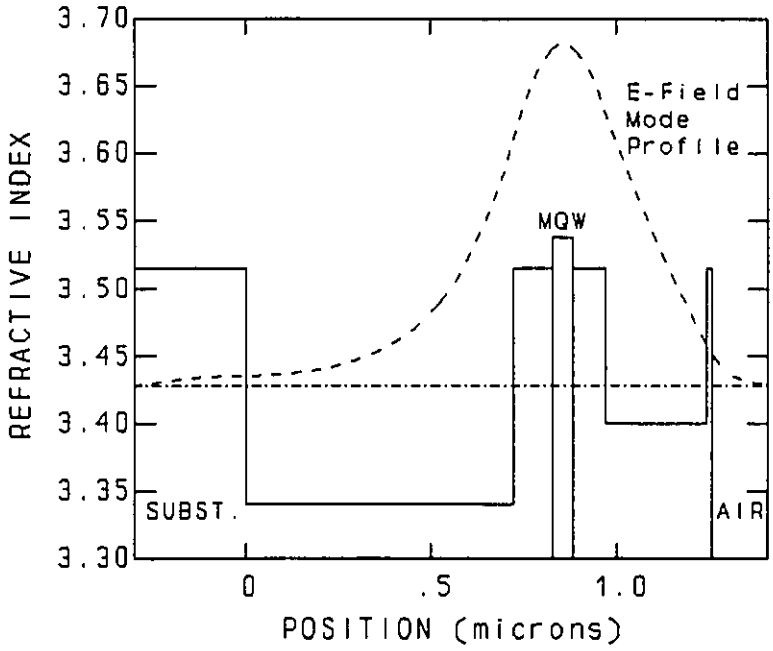


**Figure 8.6** Material 'C' slab waveguiding electric-field mode shape, effective mode index (dashed-dotted line) and refractive index profile.

such that the mode shape matched that of the input (or output) fibre. For our measurements, however, this was not necessary. By making the ribs 20$\mu$m wide, which is larger than required, the rib and slab waveguide modes should be very similar. We therefore need only to model slab waveguiding in these materials. Only TE-polarized waveguiding is calculated. The electric-field mode profiles, the material refractive index profiles, and the effective mode indices are shown in Figure 8.4, 8.5, and 8.6 for materials A, B, and C. The calculation method is from Appendix A. The refractive indices are from Casey [Casey, 1974] and Das [Das, 1985].

An important value to be derived from the waveguiding calculations is the confinement factor $\Gamma_{MQW}$. This corresponds to the fraction of the waveguiding intensity within the multiple quantum well region. When $\Gamma_{MQW}$ is multiplied by the absorption coefficient of the waveguide material, the result is the effective absorption per unit length of the waveguiding mode. Table 8.1 gives these values, as well as values for the mode absorption coefficient due to absorption due to a gold covering of the epilayers. We do not have gold on our waveguides, but we tried. Also given

**Table 8.1** MQW confinement factors, waveguide sample lengths, mode absorption coefficients due to the MQW regions, and metalization absorption and substrate leakage loss coefficients.

| | A | B | C |
|---|---|---|---|
| $\Gamma_{MQW}$ | 0.723 | 0.078 | 0.168 |
| $L_{Wav}$ slab ($\mu$m) | 360 | 430 | 910 |
| $\Gamma_{MQW}L_{Wav}$ slab (cm) | 0.026 | 0.0033 | 0.0072 |
| $L_{Wav}$ rib (cm) | 0.078 | 0.092 | 0.084 |
| $\Gamma_{MQW}L_{Wav}$ rib (cm) | 0.056 | 0.0072 | 0.014 |
| loss due to Au (dB/cm) | 3.5 | 3.8 | 28.5 |
| first mode loss (dB/cm) | 0 | 0 | 13.1 |
| second mode loss (dB/cm) | 8620 | 12600 | 6700 |

in this table is the loss coefficients due to leakage of the lowest-order mode into the

substrate. The loss of the leaky second order mode is also given. The existence of a low-loss second-order mode could greatly affect the absorption of the waveguiding light in the MQW regions. As shown in the table, the materials should also be strongly single mode. Notice that we have not taken into account index of refraction changes at the band-edge of the MQW. As the band-edge shifts with applied electric field, the refractive index reduces, changing the mode shape. This will slightly affect coupling, and the confinement factor, but it is not considered important in our case.

## 8.4 Experimental Slab Waveguiding and Switching

Waveguiding transmission spectra for the 360$\mu$m-long slab waveguide cleaved

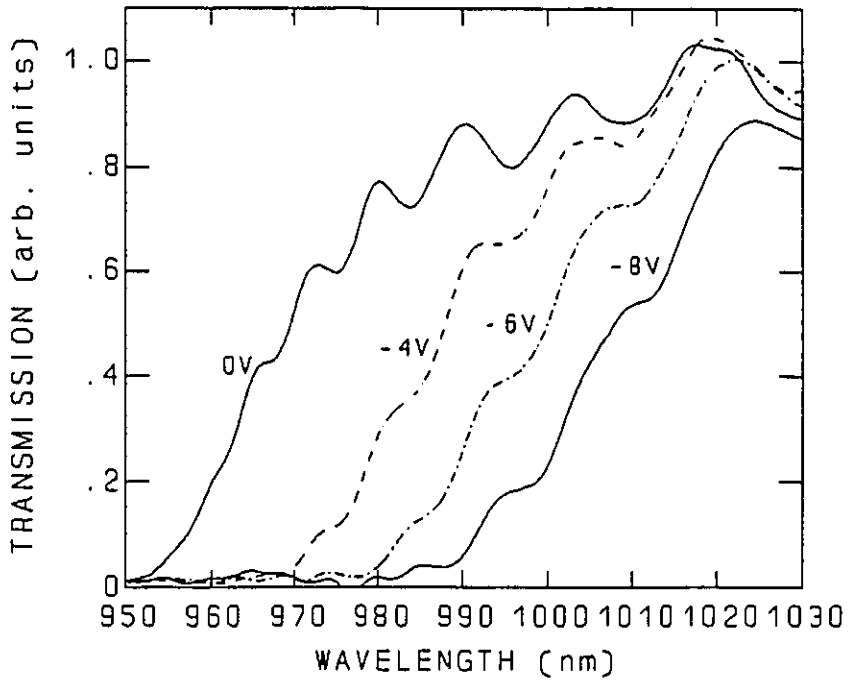


**Figure 8.7** Material 'A' transverse magnetic (TM) polarized, slab waveguiding transmission for several bias voltages.

from material A are shown in Figures 8.7 and 8.8. Figure 8.7 is for the TM-polarized

light and Figure 8.8 is for the TE-polarized light. Notice that the transmission edge at all biases, but especially at 0V-bias, is at shorter wavelength in the TM-polarized spectra. This is because an electron to heavy-hole optical dipole transition has no matrix element in the TM-direction. This means that the TM absorption edge consists of transitions between electrons and light-hole states, or transitions between electrons and mixed light/heavy holes. This may be important if switching of both

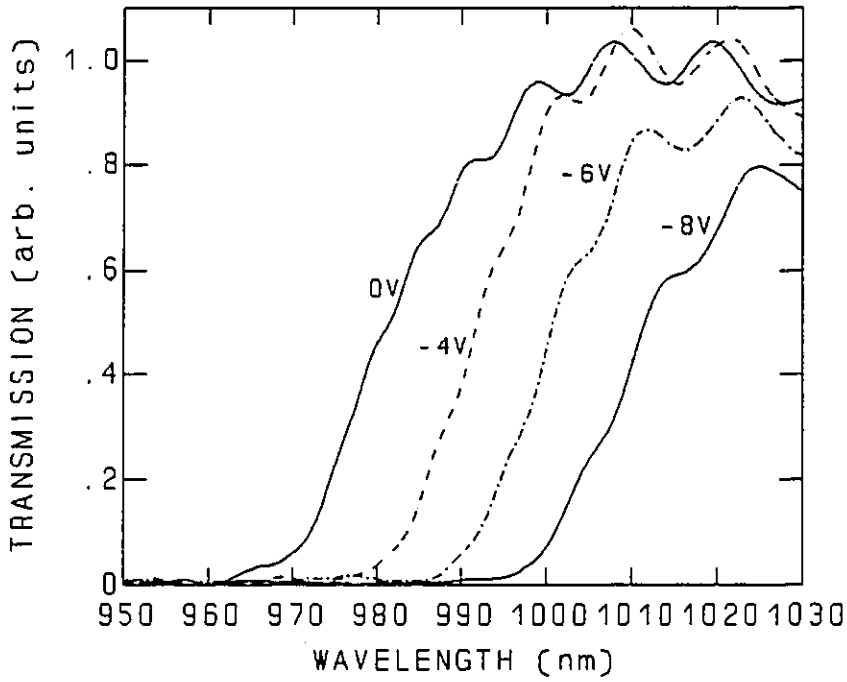


**Figure 8.8** Material 'A' transverse electric (TE) polarized, slab waveguiding transmission for several bias voltages.

TE and TM polarizations is required. We have not considered light holes in our calculations. The voltage on the slab sample could not be increased beyond about -9V bias, although rib samples could be biased to -16V. However, even between the 0V and -8V curves shown in Figure 8.8, it is clear that good switching can occur. The 0V to -8V switching ratios and the zero-bias transmission loss (given in a

logarithmic dB scale) are shown in Figure 8.9 for various operating wavelengths. If $T_{0V}$ and $T_{-8V}$ are waveguide transmission values at 0V and -8V bias, then the switching ratio between these operating biases is,

$$\text{Switching Ratio} = 10 \log_{10}\left(\frac{T_{0V}}{T_{-8V}}\right) \quad in\ dB \qquad [8.1]$$

The maximum switching ratio is about 25dB at 980nm, but the transmission loss is

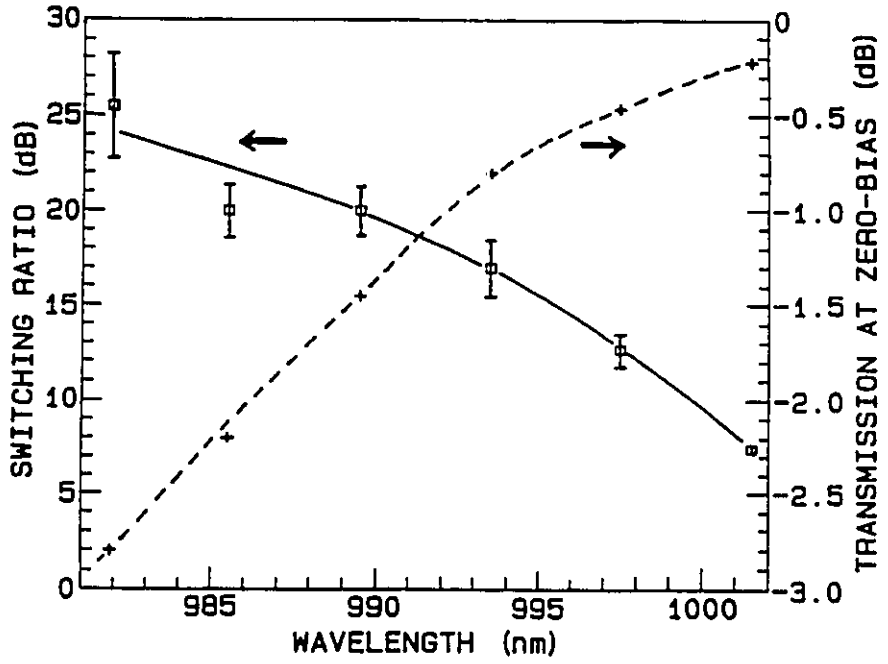


**Figure 8.9** Material 'A' slab waveguiding switching ratios between 0V bias and -8V bias. Also given is the transmission loss at 0V due to MQW absorption. Scattering and coupling losses are not measured.

3dB. At 1000nm, the switching ratio decreases to 7dB, but the transmission loss at zero bias is close to zero. The wavelength of operation will depend on whether switching ratio or loss is the most important factor. A longer sample would be bad for device speed, but would actually improve the switching performance. This is

because on the logarithmic scale, a longer sample would just multiply the values given in Figure 8.9 by the ratio of length change. For instance, at 993.5nm wavelength, doubling the length would result in 34dB of switching with only 1.6dB of zero-bias transmission loss. Although the absolute absorption coefficients are smaller at longer wavelength, the ratio of absorption coefficients between low and high bias are greater, increasing the performance of long modulators. This observation is correct even in bulk modulators. Therefore when designing a modulator, one usually trades off device size and speed vs. low loss and good switching ratio.

Figures 8.10 and 8.11 show the transverse electric (TE) polarized waveguiding

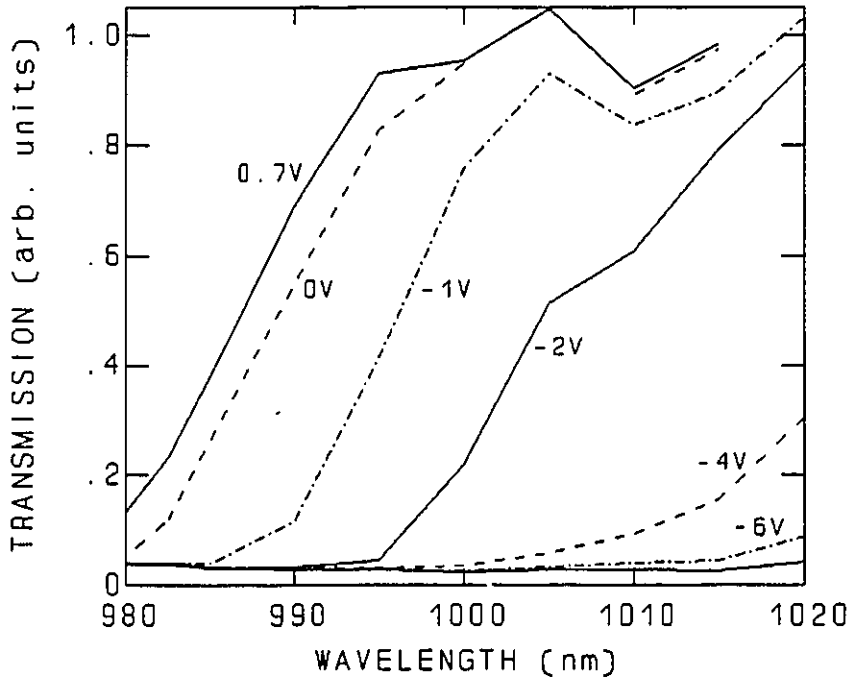


**Figure 8.10** Material 'B' TE-polarized slab waveguiding transmission spectra for various bias voltages. The waveguide length is 430$\mu$m.

transmission spectra for slab samples of materials B and C. For Fig. 8.10, a 100%

line was drawn corresponding to wavelengths where zero photocurrent occurred, and the transmission curves were divided by this line. This was done to avoid confusion as to the actual switching. Depending on the alignment of the input fibre to the waveguide, and of the slit which filters out stray light, the system response can increase or decrease with wavelength. This change is not a real change in

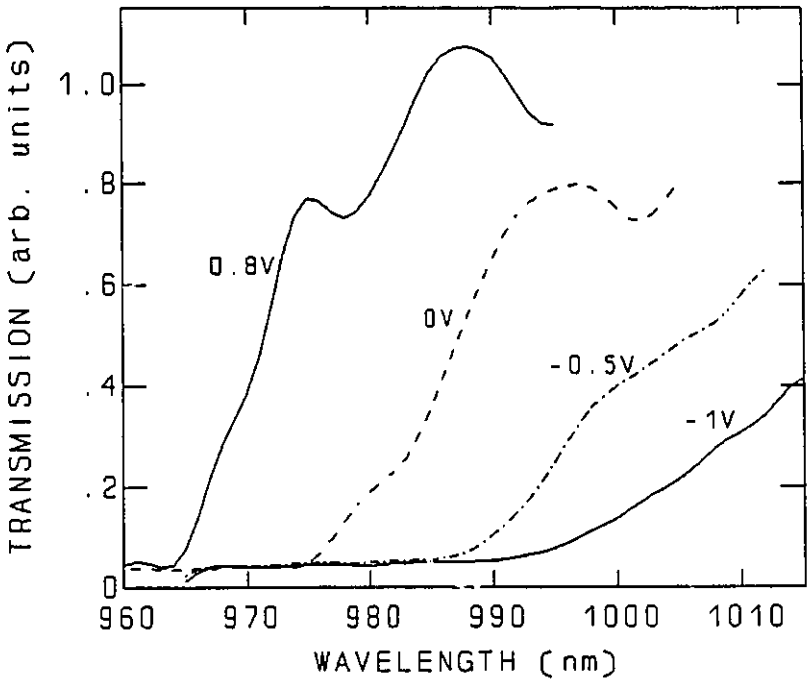


**Figure 8.11** Material 'C' TE-polarized slab waveguiding transmission for various bias voltages. The waveguide length is 910$\mu$m.

waveguiding, and was divided out to avoid confusion. All measurements showed some periodic fringes in the spectra. The exact cause was not determined, but there are many possible contributions, including interference between the sample and the fibre, or interference from defects in the samples, or some sort of diffraction effect occurring during input coupling. The interference periods are much too large to be Fabry-Perot fringes between the sample ends. Short-period (2nm) fringes in Fig. 8.11

(with about 20% depth) were smoothed out using a Fourier-transform smoothing routine, leaving longer-period fringes. Since some spectra, like in Figure 8.10, include only a few points, fringes will have the effect of adding noise to the curves.

As the slab samples of materials B and C could be pushed to higher fields than material A, the switching appears to be good over a wide wavelength range. The transmission does not reach zero at short wavelength due to stray light. Transmission curves for material C were essentially zero over the wavelength range shown for bias voltages -2V to -8V, and were therefore not taken. Switching can be accomplished with just a couple of volts of bias, but using high reverse-bias allows switching to occur over a large operating wavelength. Notice that the high built-in field of material C causes a large shift at 0V-bias as compared to the transmission edge at lower field at +0.8V bias. These experimental spectra will next be compared against theory.

## 8.5 Theoretical Slab Waveguiding Transmission

By modelling the theoretical electro-absorption, one can produce a model which will provide both qualitative and quantitative information about modulator performance, and the optimum design of electro-absorption devices. In this section, the absorption-edge calculations performed in the last chapter will be used to theoretically determine the slab waveguiding transmission spectra. These can be compared to the experimental curves of section 8.4, and with some adjustment for different waveguide lengths, can also be compared to the rib-waveguide results shown in the next section. These comparisons will allow interpretation of any discrepancies in the model. The solid theoretical curves in Figures 8.12 to 8.14 are calculated using a single broadened exciton and continuum edge. The dashed curves are

calculated using the high-field model by summing a continuum of band-edge transitions. The spectra are calculated using the formula,

$$\text{Trans} = \exp(-\alpha_{broad}\Gamma_{MQW}L_{Wav}) \qquad [8.2]$$

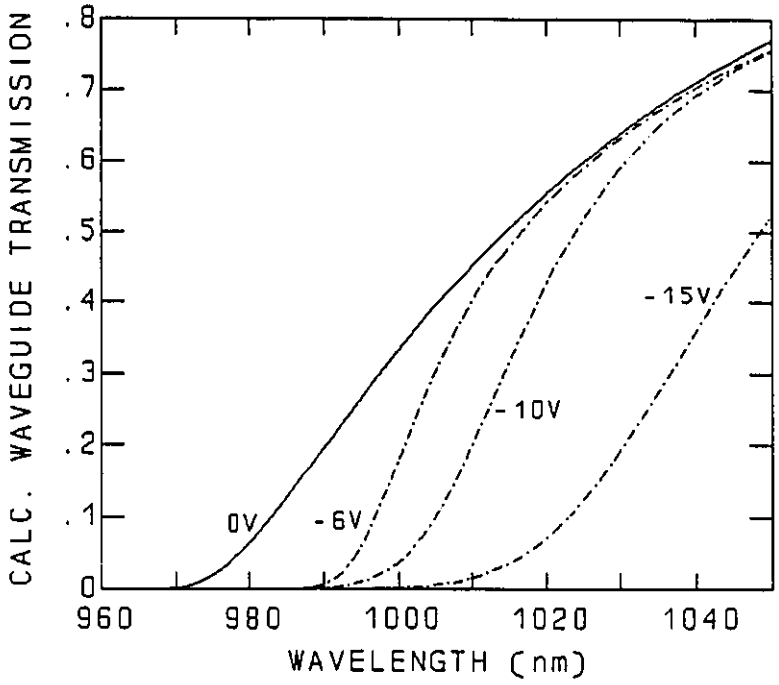


**Figure 8.12** Material 'A' theoretical slab waveguiding transmission spectra for various bias voltages. The dashed spectra use the high field calculation method. These curves can be compared to the experimental spectra of Figure 8.8.

The theoretical transmission spectra for material A compare well with both slab and rib waveguide spectra. The main difference is the tendency of the theoretical curve to never get to 100% transmission. This is largely a result of the Lorentzian phonon broadening of 3.7 meV which was included in the spectra. While a Lorentzian lifetime broadening is close to the correct shape, a Lorentzian curve will continue for many tens of its width before approaching zero. This does not correspond well to reality, since the long-wavelength tail of an absorption edge

typically shows an exponential shape, which much more quickly approaches zero. It is not clear how to remedy this without resorting to arbitrary modifications. The onset of transmission is determined quite well in the theoretical curves, however.

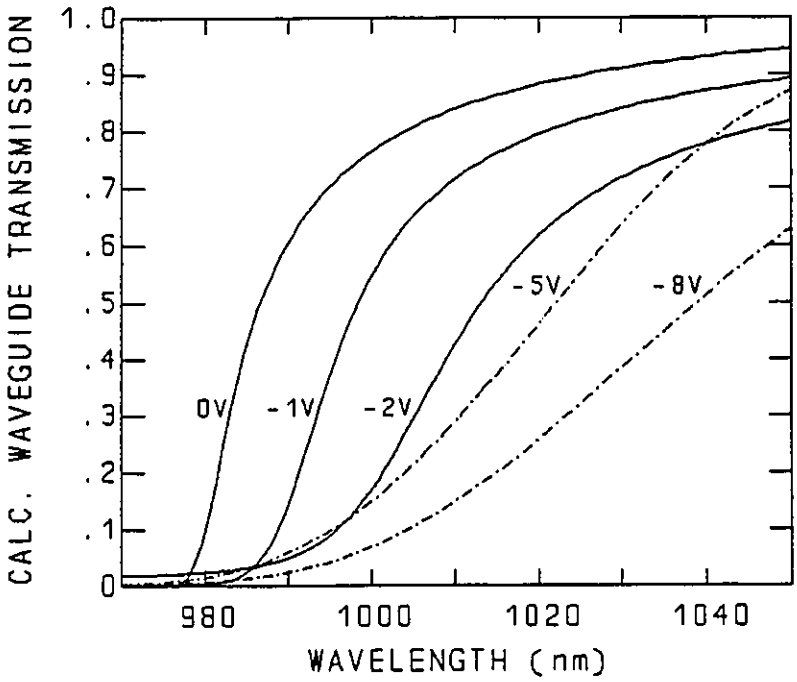


**Figure 8.13** Material 'B' theoretical slab waveguiding spectra for various bias voltages. The dashed spectra use the high field calculation method. These curves can be compared to the experimental spectra of Figure 8.10.

The theoretical spectra of Figure 8.13 for material B do not compare quite as well to experiment, but are not too bad. There is, of course, some discontinuity in changing from the model of a single broadened transition to the high-field model of a continuum of transitions. This is partly because of our ignoring excitons in the high-field model, and partly because of the inaccuracy of the single-transition model at high field, with its large Lorentzian broadening. However, as seen in Chapter 7, the theoretical model for material B does not provide a strong enough absorption edge. This results in the not-very sharp theoretical -8V transition edge seen in Fig.

8.13. The uncertainties in the parameters have already been mentioned in Chapter 7, and may explain this. One possibility not mentioned yet is that there is a considerable amount of bulk $In_{.07}Ga_{.93}As$ surrounding the quantum wells which may provide absorption at higher energy. While the significance of this is only speculation, the Franz-Keldysh effect in this bulk material, which has only a slightly larger bandgap than the quantum wells, may result in a larger absorption at just slightly higher energy than the bandgap. This larger absorption would provide a sharper absorption edge for the high-field spectra.

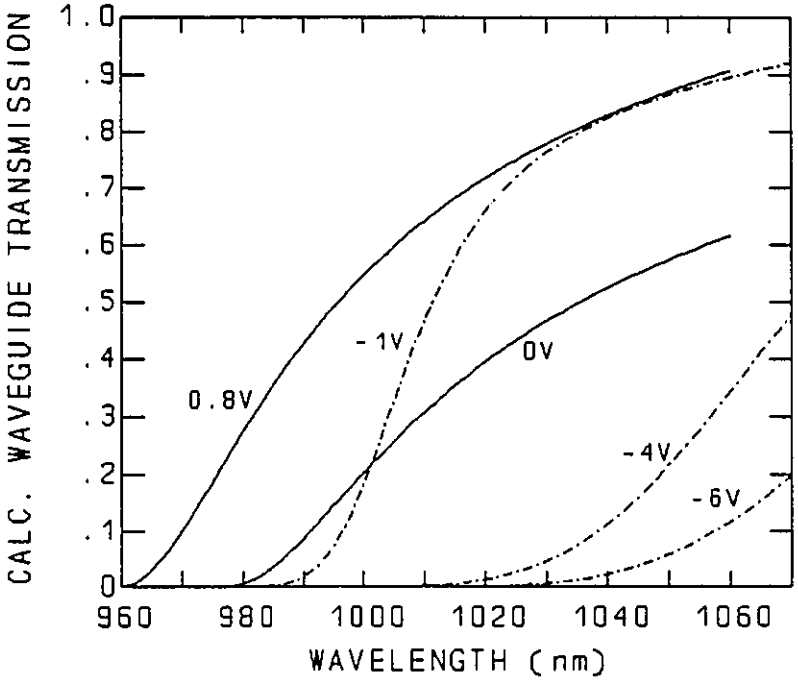


**Figure 8.14** Material 'C' theoretical slab waveguiding spectra for various bias voltages. The dashed spectra use the high field calculation method. These curves can be compared to the experimental spectra of Figure 8.11.

The theoretical material C transmission spectra correspond well to the rib and slab waveguide spectra. The main discrepancy is the transition from the 0V to the -1V-bias curves. The single transition model overestimates the shift of the 0V curve,

and the high-field model underestimates the shift of the -1V curve. However, the other very-low and very-high field curves are close to correct. Again, the Lorentzian broadening included in the calculations prevents any of the theoretical spectra from attaining 100% transmission.

## 8.6 Rib Waveguide Transmission, Switching, and Photocurrent

The length of cleaved rib-waveguide samples are given in Table 8.1. Rib-waveguiding transmission measurements were made in the same manner as for slab waveguide samples. The transmission spectra for rib samples cleaved from materials

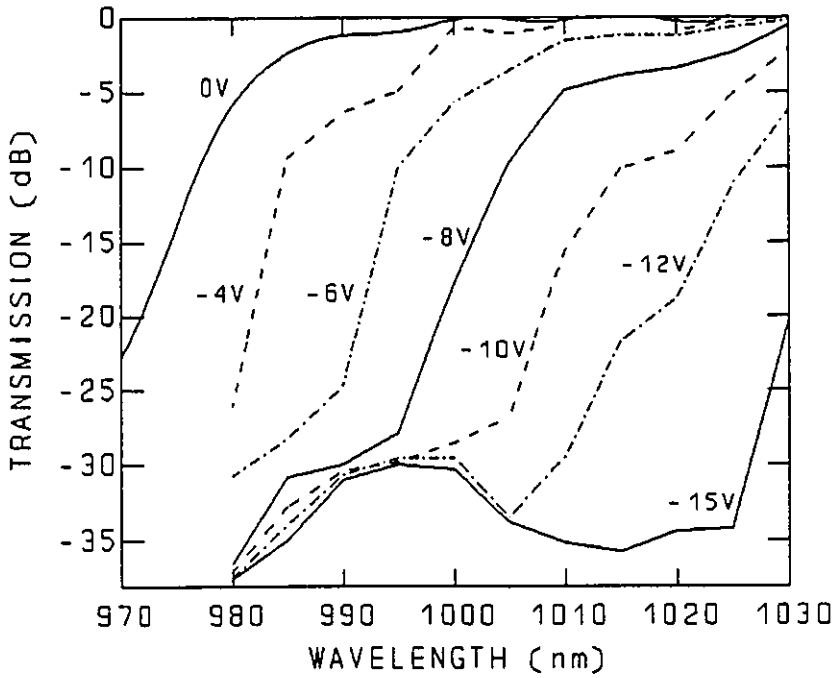


**Figure 8.15** Material 'A' rib-waveguide transmission spectra for various bias voltages. Transmission is shown on the logarithmic dB scale, with 100% transmission equal to zero.

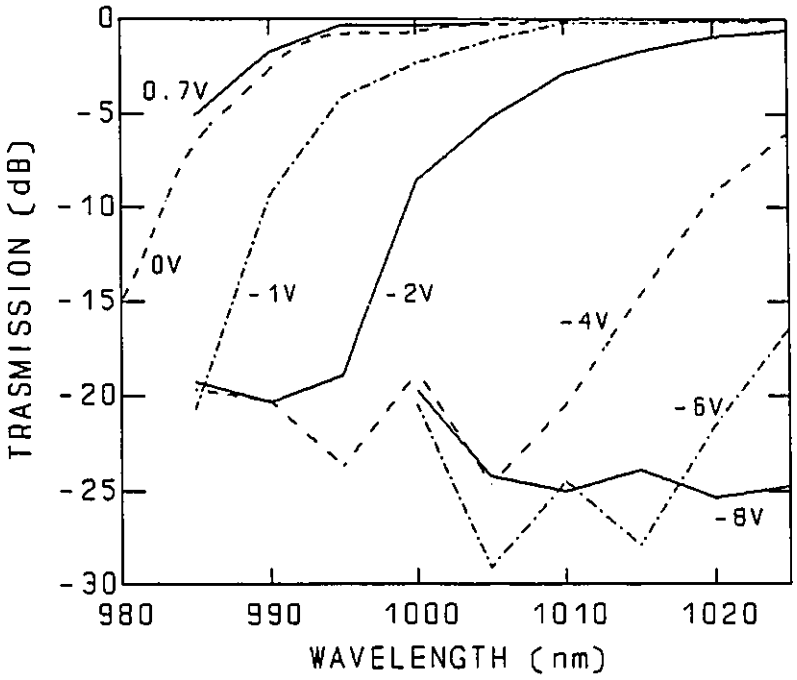


**Figure 8.16** Material 'B' rib-waveguide transmission spectra for various bias voltages. Transmission is shown on the logarithmic dB scale, with 100% transmission equal to zero.

A, B, and C are given in Figures 8.15, 8.16, and 8.17 respectively. The intensity of transmission is given on the logarithmic dB scale to facilitate the reading of switching and loss values. The switching between any two voltages at a particular wavelength is simply the subtraction of the transmission values in dB. The absorption loss at any one wavelength and bias is simply the negative of the transmission value in dB. Ten dB equals a factor of ten in power. As can be seen in all the spectra, as the reverse-bias is increased, the electric field increases, and the absorption edge shifts to longer wavelength. Material A shows up to 35dB of switching with less than 2 dB of loss at several wavelengths for bias changes from 0V to -15V. However, one might want to operate the device at a lower operating voltage. Even changes from 0V to -6V provide 23dB of switching with about 2dB of loss at 990nm wavelength. The rib-

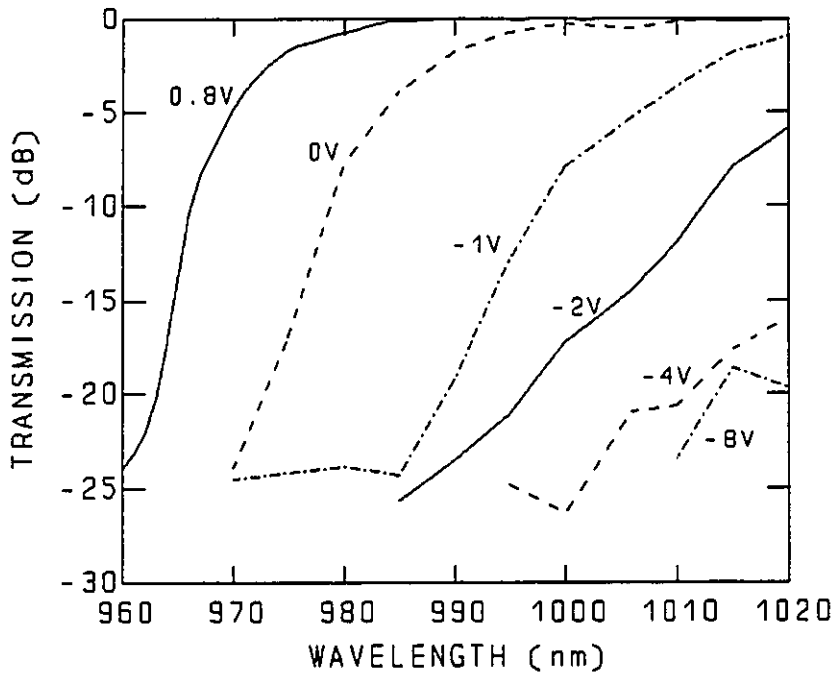


**Figure 8.17** Material 'C' rib-waveguide transmission spectra for various bias voltages. Transmission is shown on the logarithmic dB scale, with 100% transmission equal to zero.

waveguide samples from materials B and C also show good switching, with greater than 18dB of switching over a 40-50nm range in each material. One interesting feature with all rib waveguiding materials is the apparent saturation of transmission loss at some value between -25dB and -35dB. This levelling off of switching is not a true physical effect within the waveguide, but is rather the level of stray light detected by the detector. Therefore switching is almost surely better than the results given here. It is difficult to filter out all of the stray light travelling through the substrate, or travelling through the air above the waveguide. The 0dB level is set by drawing a line through the linear transmission spectra at wavelengths where photocurrent data show no absorption. This line became the 100% transmission line, and all spectra were divided by it.

The fact that high switching ratios were seen is not that new, although many investigations report lower values of 8dB to 13dB [Das, 1987] [Wakita, 1986]. Even bulk materials can produce 30dB switching, but what would not be expected in bulk materials is the large wavelength range of high performance switching operation seen here. The sharpness of low-field exciton absorption peak results in a low transmission loss at longer wavelength than the absorption edge. The electron and hole confinement produced by the quantum wells causes a larger absorption coefficient change with field than would be seen in bulk materials. It is important to high-power switching in quantum-well modulators that the carriers do not build up in the wells, but rather are swept out quickly and collected at the terminals. A build up of carriers would destroy the low-field exciton due to free-carrier scattering, degrading modulator performance. The carriers may also screen the applied field. Carrier build-up should not be a significant effect in electro-absorption modulators, as the fields used are usually high enough to sweep carriers out of the wells very quickly. A carrier may only spend a few picoseconds within the multiple-quantum-well region. Chapter 9 will examine how modulator structure is likely to affect InGaAs-GaAs modulator performance.

The waveguiding photocurrent was also measured in rib-waveguide samples of materials A and B. The current-to-voltage converter circuit is explained in appendix E. The modulator effectively acts as a waveguide detector, and the photo-generated carriers are measured. The photocurrent spectra are given in Figures 8.18 and 8.19. At low field, the photocurrent, and therefore the absorption, is close to zero over much of the wavelength range. At high reverse bias voltage, the absorption edge shifts to longer wavelength and the photocurrent approaches some maximum value corresponding to full absorption. One may notice, however, that the

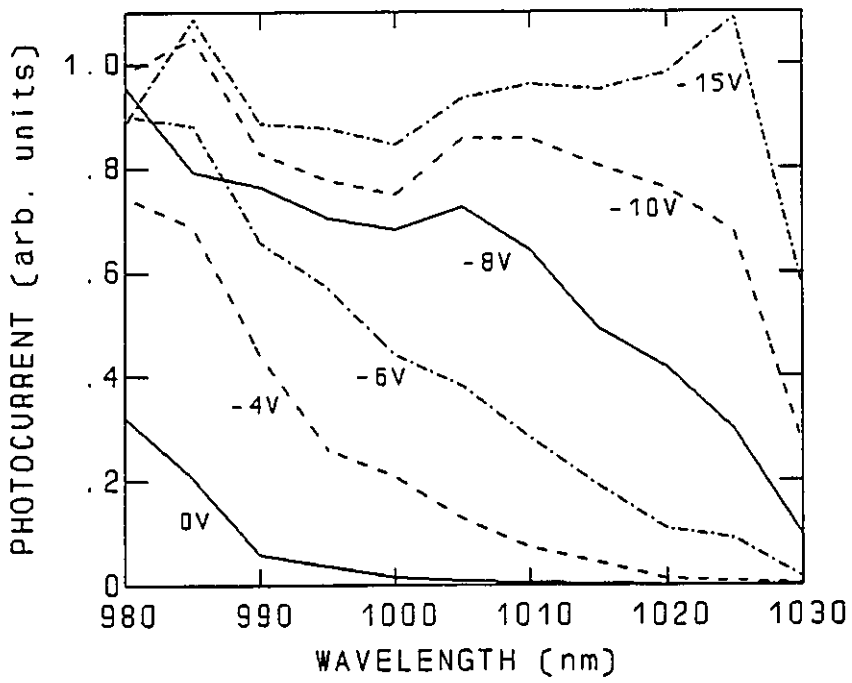


**Figure 8.18** Material 'A' rib-waveguiding photocurrent spectra for various bias voltages.

photocurrent never seems to fully saturate at some upper value, even at wavelengths where transmission spectra show almost no transmission. This is because some fraction of the photocurrent does not come from absorbed light waveguiding in the first order mode. Because of poor mode match between the fibre and the waveguide, a large amount of light is coupled into leaky radiation modes, or travels through the MQW epilayers once only, without waveguiding. This light would not be fully absorbed since it would interact with the MQW for only a short path length, but the absorbed part would still be seen in the photocurrent. As the MQW absorption coefficient increases with field, a larger fraction of this stray light will get absorbed, resulting in an ever-increasing photocurrent with field. One could design a waveguide with greater coupling to the fibre to reduce this effect. However, a high

thickness waveguide would have other problems, such as either a low confinement

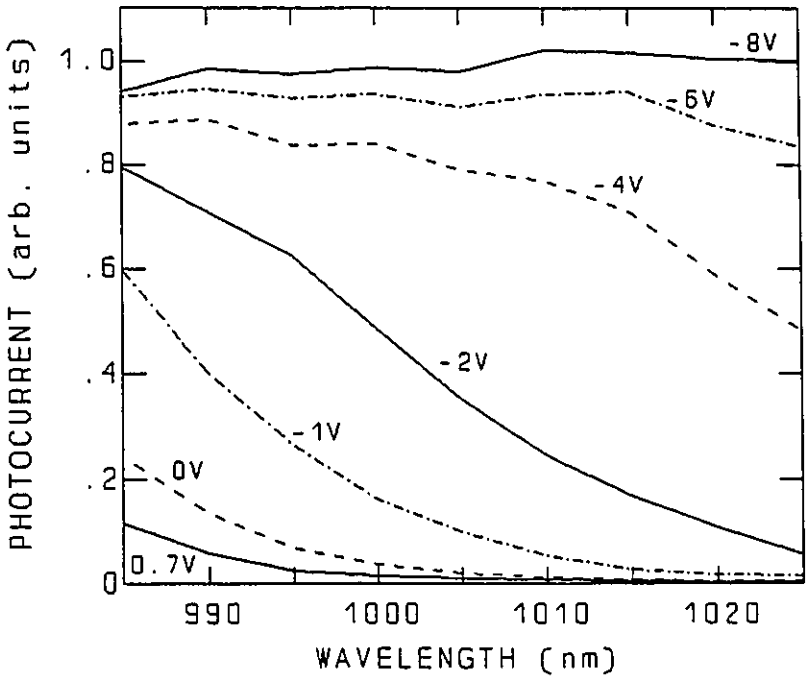


**Figure 8.19** Material 'B' rib-waveguiding photocurrent spectra for various bias voltages.

factor $\Gamma_{MQW}$ for the multiple quantum well, or else an overly thick intrinsic region which would require high operating voltages and may have non-uniform field due to residual intrinsic-region doping.

## 8.7 Conclusions

Apparatus was designed to measure the transmission spectra of cleaved slab waveguide samples, and cleaved rib-waveguides which were processed using wet chemical etching techniques. The waveguiding transmission spectra displayed up to 60nm shift of the transmission edge. Switching ratios were 20-35 dB on the rib-waveguide samples with less than 2dB of loss over a large (>35nm) wavelength range

using maximum voltage modulation. The samples also showed good results for small field changes, although the operating wavelengths were restricted. Theoretical absorption spectra generally agreed well with theory, although the assumed Lorentzian-shaped phonon broadening was seen to extend the theoretical band-tail absorption to too long a wavelength. This resulted in theoretical spectra which never approached 100% transmission. We observed it was necessary to change from the theoretical model of a single broadened feature to the model of a continuum of transitions at high field. Some discontinuity was seen at the interface between these two methods. Experimental waveguiding photocurrent spectra were also taken, which gave an indication of the wavelengths of zero low-field absorption.

# CHAPTER 9

# Theoretical Comparisons of Electro-Absorption in Various Structures

## 9.1 Introduction

In this chapter, we will compare the factors affecting modulator performance for various quantum-well structures. Because of possible electrical and light-scattering problems associated with defects in the dislocated structures, the structures in this chapter will be assumed to be strained to the substrate lattice constant. Similar performance factors have been investigated in $Al_xGa_{1-x}As$-GaAs structures [Cho, 1989][Daly, 1990], and in $In_xGa_{1-x}As$-GaAs structures [Coffey, 1988]. The work by Cho and Daly is not directly applicable to InGaAs structures, and the work done by Coffey is brief, and ignores the effects of various field-dependent broadening factors. Our calculation methods also differ from all of these papers.

Calculations by Miller et al. [Miller, 1985] use infinite barriers to approximate finite wells. While that is a gross approximation, it allows one to derive qualitative analyses of absorption changes with electric field which are easily generalized to any structure. While this may be acceptable for deep wells, it does not yield adequate accuracy for shallow wells, and gives no information about tunnelling. There are therefore really no shortcuts to determining quantum-well performance other than to perform the calculations. That is why this thesis provides models for absorption-edge calculation in low and high-field regimes. Because a modulator optimized for speed would probably have to operate in the low-field regime, we have used the low-

field model of a single band-edge exciton feature in this chapter. This is the easiest model to understand anyway. Using these calculations, I will attempt to determine guidelines for the design of $In_xGa_{1-x}As$-GaAs modulator structures.

## 9.2 Quantum-Well Masses, Energies, Energy Shifts, and Broadening

The effective bandgaps (not including the exciton binding energy) vs. indium concentration for various quantum-well widths are given in Figure 9.1. Any

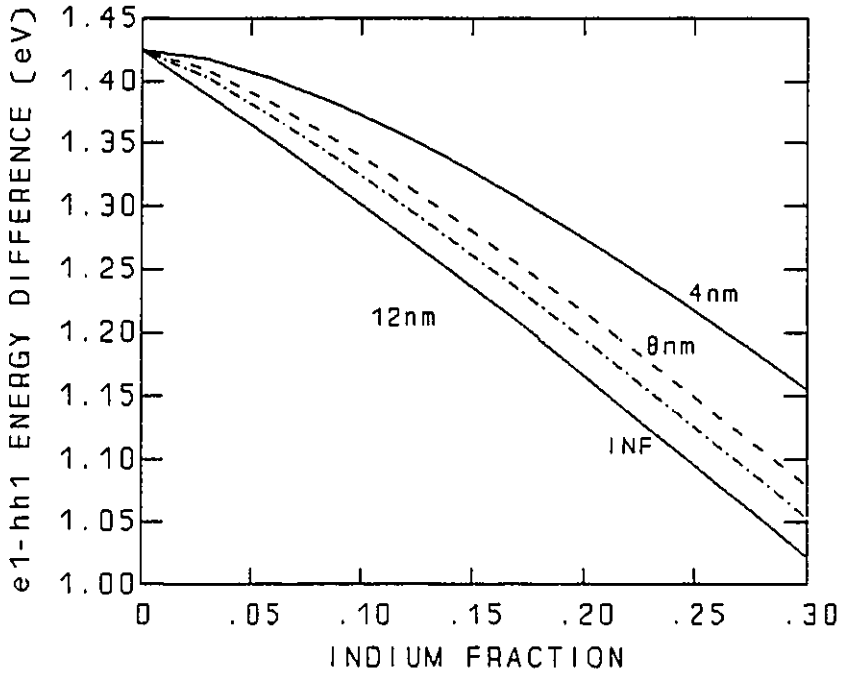


**Figure 9.1** The energy gap between the electron-1 and heavy-hole-1 energy solutions for 4nm, 8nm, 12nm, and infinitely-wide $In_xGa_{1-x}As$ quantum wells lattice matched to GaAs.

particular bandgap can be derived using a range of different well widths. This allows one to be able to tailor the electro-absorption properties. One parameter which affects binding energy, absorption sharpness, and absorption strength is the

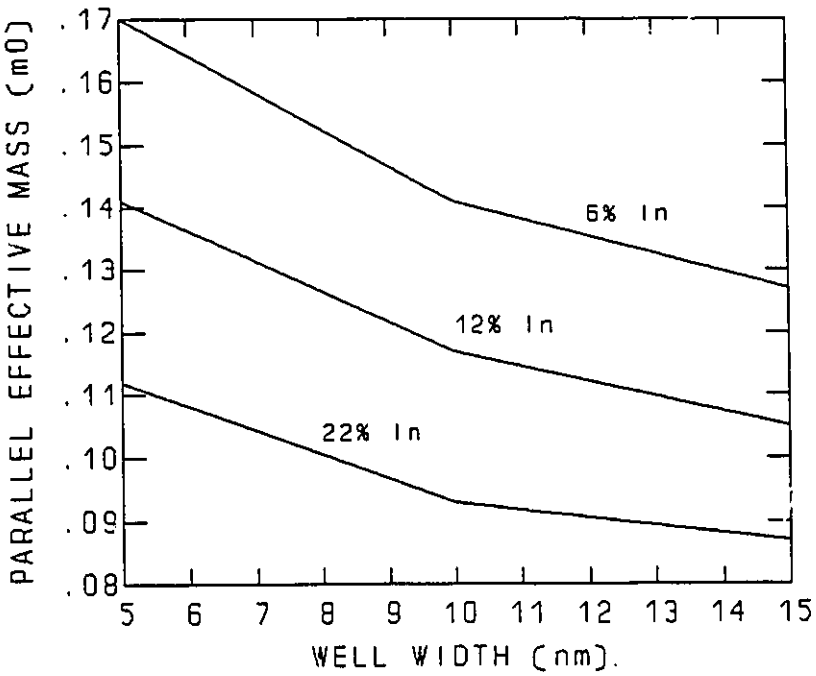


**Figure 9.2** The effective mass, $m_{\|}^{*}$, for the heavy-hole-1 wavefunction for motion parallel to the lattice planes. Curves are for 6%, 12%, and 22% indium-concentration quantum wells.

heavy-hole effective mass in the direction parallel to the layer planes. Values for this are given in Figure 9.2 vs. well width, calculated for a total of nine points. The parallel effective mass is larger in smaller indium concentration materials because there is not as much splitting between the heavy and light holes in these less strained materials. In deep wells, the decoupling of light and heavy holes makes the effective mass approach the diagonal-Hamiltonian value of $m_0/(\gamma_1+\gamma_2)$. For an indium fraction $x$, the Luttinger parameters are [Hellwege, 1982]: $\gamma_1=6.85+12.82x$, $\gamma_2=2.10+6.27x$, $\gamma_3=2.90+6.39x$. A wider well width results in a lower effective mass, again because the heavy-hole energy solution becomes more separated from the light-hole ones. A large effective mass increases the binding energy, and increases the absorption strength. It is not clear how the mass changes with field.

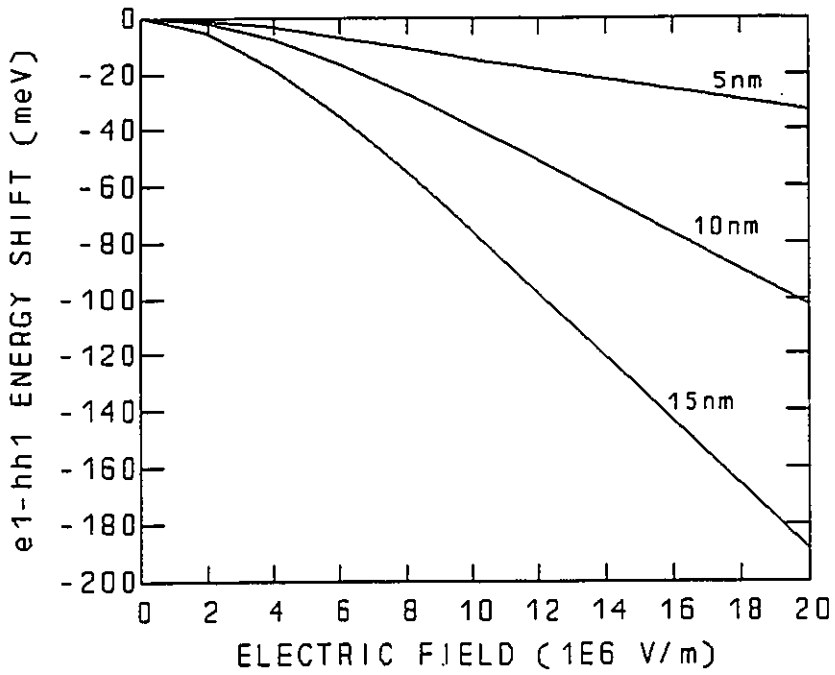


**Figure 9.3** The change in the electron-1 to heavy-hole-1 energy gap vs. electric field for 12% indium fraction $In_xGa_{1-x}As$ quantum wells of 5nm, 10nm, and 15nm well widths.

The absorption edge shifts with field (not including changes in exciton binding energy) are given in Figure 9.3 for 12% indium fraction wells. If $e$ is the magnitude of the electron charge, $F$ is the electric field, and $W$ is the well width, the energy shifts $\delta E$ at high field approach parallelism with the line $\delta E = -2eFW$. Therefore wider wells experience the greatest absorption-edge shifts for the lowest field. This, however, assumes that the lowest-energy exciton is the dominant band-edge absorption feature. For very wide wells, however, the lowest-energy transition weakens quickly with field, and a Franz-Keldysh-type calculation must be done. For very narrow wells, the energy shift with field is very small, and high fields must be used for switching. This is bad for high-speed devices. Figure 9.4 shows the absorption-edge shifts with field for 10nm wells. While the curves for various indium

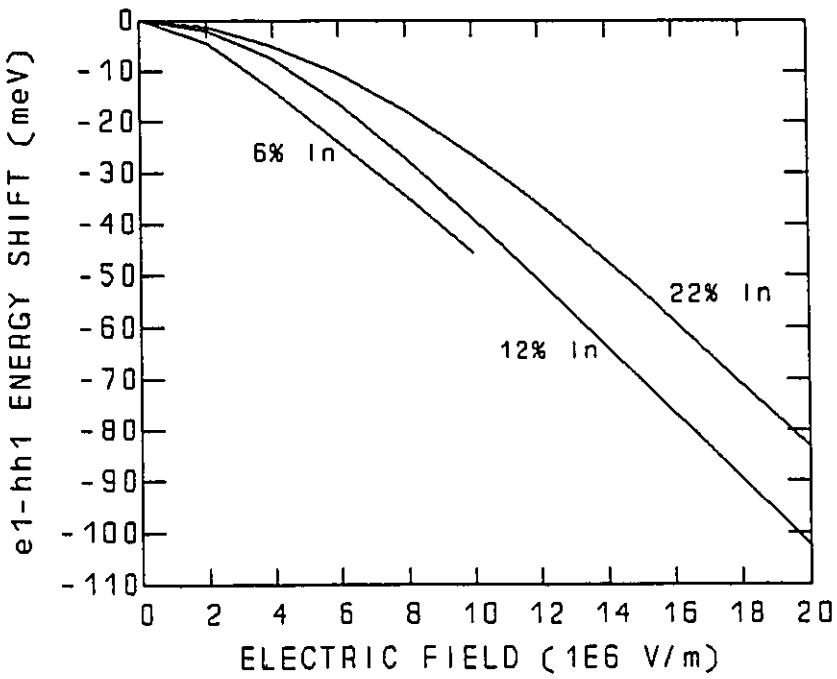


**Figure 9.4** The change in the electron-1 to heavy-hole-1 energy gap vs. electric field for 10nm-wide $In_xGa_{1-x}As$ quantum wells with indium fractions of 6%, 12%, and 22%.

concentrations do become parallel at high fields, notice that the low indium-fraction wells shift slightly more with field. This is due to the interaction of the wavefunctions in these shallower wells with the continuum. Therefore these larger shifts are also correlated to larger broadening.

A large component of the energy broadening at high field is the lifetime broadening of the exciton and 2-dimensional continuum edge due to wavefunction tunnelling. This tunnelling width is given in Figure 9.5 for 12% indium-fraction wells and three well widths. The broadening is seen to differ only slightly for the various well widths. The narrower well has energy solutions closer to the top of the quantum wells, so it makes sense that it should experience broadening at slightly lower field. The three curves approach the same slope at high field. The tunnelling

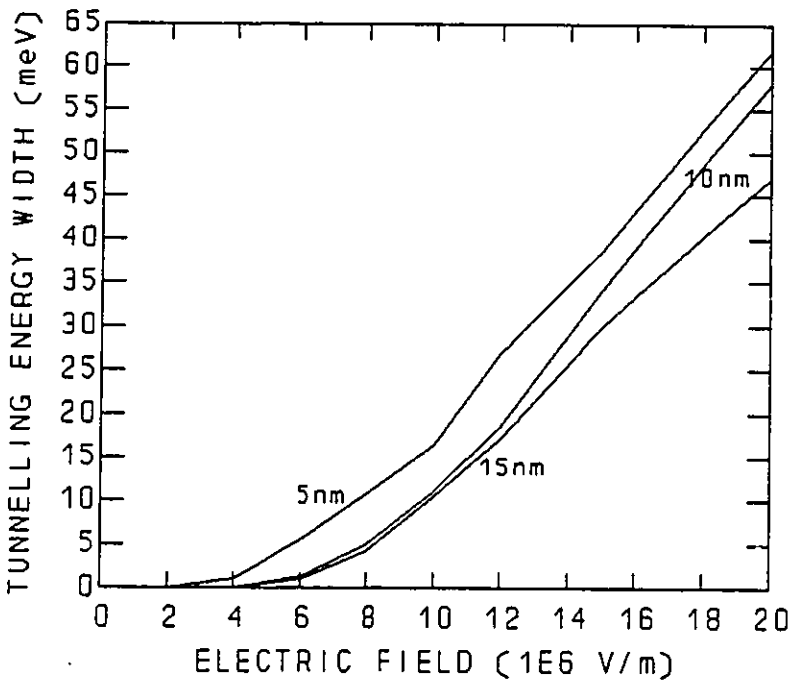


**Figure 9.5** The contribution to the energy width from electric-field-induced tunnelling of the wavefunctions out of $In_{.12}Ga_{.88}As$ quantum wells with well-widths of 5nm, 10nm, and 15nm.

broadening for 10nm wells at three different indium concentrations is given in Figure 9.6. Here the broadening is much larger for the smaller indium-concentration wells. The electric field required to cause any particular energy broadening is approximately proportional to well depth. The tunnelling broadening is of course zero at zero field. One must decide whether tunnelling broadening is good or bad for modulator performance. The answer depends on whether the modulator is required to perform at high speed. A high speed modulator requires maximum absorption change close to the band edge, so that a small device can be used. High broadening reduces the height of the exciton peak, reducing the maximum absorption change possible. However, the broadening could improve switching performance if one is willing to sacrifice some speed. A quickly broadening edge with field results in absorption

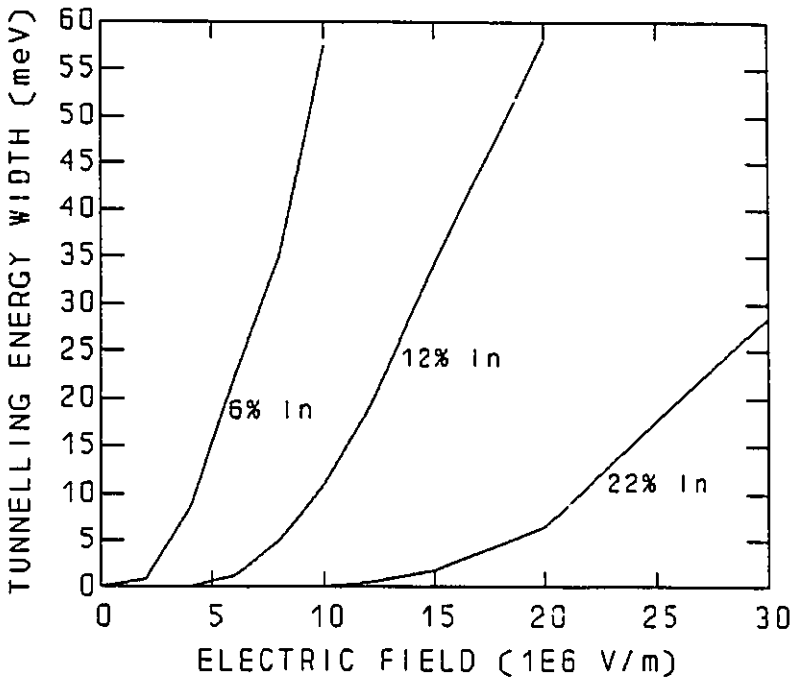


**Figure 9.6** The contribution to the energy width from electric-field-induced tunnelling of the wavefunctions out of 10nm-wide $In_xGa_{1-x}As$ quantum wells with indium fractions of 6%, 12%, and 22%.

changes occurring at long wavelengths, where no absorption occurred before. A long modulator would be able to utilize this absorption change to produce high switching ratios with low loss, similar to the modulators tested in this thesis. A quick broadening of the edge may also improve the wavelength range of switching operation, provided the low-field edge is sharp.

As mentioned in earlier chapters, the energy broadening $\Delta E_{well}$ due to a one monolayer well-width variation $\Delta z$ approaches the line $\Delta E_{well}=eF\Delta z$ at high field. This broadening may be important to performance at high field, but probably more important is the energy broadening due to well-width variations at low field. A good modulator will have as sharp an absorption edge as possible at low field. The energy broadening due to one-monolayer of well-width variation at zero field is given in

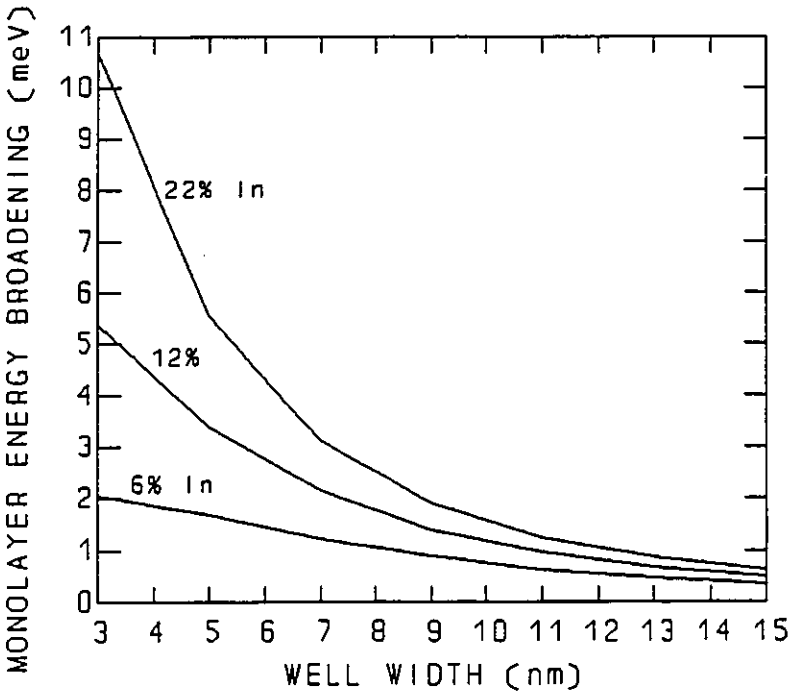


**Figure 9.7** The energy-width broadening due to a one-monolayer ($\Delta z = 0.282$nm) variation in the $In_xGa_{1-x}As$ well width, vs. quantum-well width, for 6%, 12%, and 22% indium-fraction materials at zero field.

Figure 9.7 for 10nm-wide wells with three indium-fractions. The larger indium-concentration wells, which are deeper in energy, have the largest broadening. This is because a deeper well has greater wavefunction confinement, and the effect of well-width variations will be 'felt' by the wavefunction to a greater degree. The same reasoning explains why thinner wells also experience considerably more broadening than wider wells. However, this effect also makes sense for thinner wells because a one-monolayer change in thickness is a larger fractional change in the well. Therefore quantum wells with larger binding energy also experience larger broadening due to well-thickness variations. If one desires a high-intensity, sharp, low-field exciton peak, the layer uniformity is therefore important.

## 9.3 Exciton and Continuum Absorption Strength Factors

In our low-field band model, there exists a broadened e1-hh1 exciton feature, and a broadened 2-dimensional continuum step edge starting at one binding-energy value to higher energy. The integrated absorption strength of both features is proportional to the square of the z-direction electron-hole wavefunction overlap, or $<\psi_e|\psi_h>^2$. How this overlap changes with field will affect how well the electro-absorption modulator works. For very-wide wells or very high fields, this value may not be meaningful, as broadened higher energy transitions may dominate the

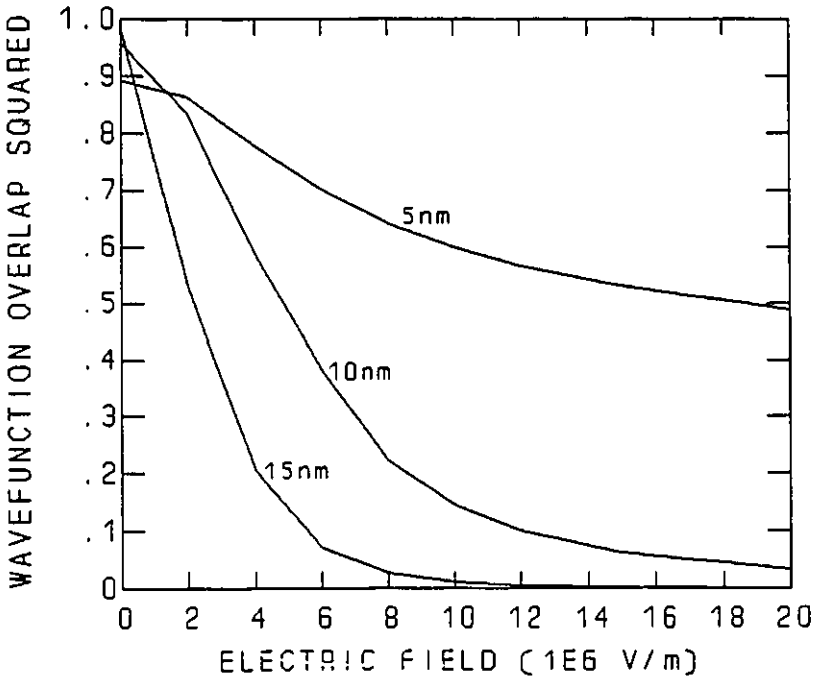


**Figure 9.8** The square of the electron-1 and heavy-hole-1 wavefunction overlap vs. electric field for 12% indium-fraction $In_xGa_{1-x}As$ quantum wells of width 5nm, 10nm, and 15nm.

absorption edge. However, Figure 9.8 shows how the square of the wavefunction overlap changes with field for various well thicknesses and a 12% indium-fraction.

Notice how the wavefunction overlap remains high at low field in the 5nm-wide well, while the overlap goes to zero in the 15nm well at high field. For wide wells, the absorption edge becomes more like the Franz-Keldysh edge of bulk materials, while for narrow wells the barrier confinement keeps the electron-1 and heavy-hole-1 wavefunctions together. Unfortunately the same confinement in narrow wells reduces the wavelength shift with field. One must trade off these two factors.

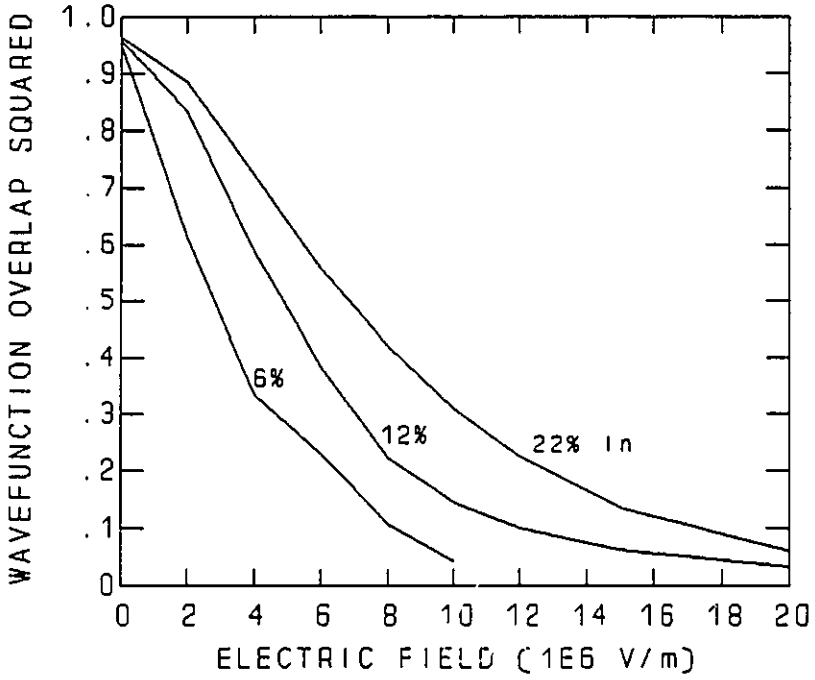


**Figure 9.9** The square of the electron-1 and heavy-hole-1 wavefunction overlap vs. electric field for 10nm-wide $In_xGa_{1-x}As$ quantum wells with indium fractions of 6%, 12%, and 22%.

The square of the e1-hh1 wavefunction overlap for 10nm wells vs. field is given in Figure 9.9 for various indium fractions. The difference between curves for 6% and 22% indium fractions are noticeable, but nothing like the variations with well-width seen in Figure 9.8. In the higher indium-fraction wells, the wells are deeper, and the slightly increased wavefunction confinement keeps the electrons and

holes together better at high fields. The deeper wells also help prevent wavefunction tunnelling.

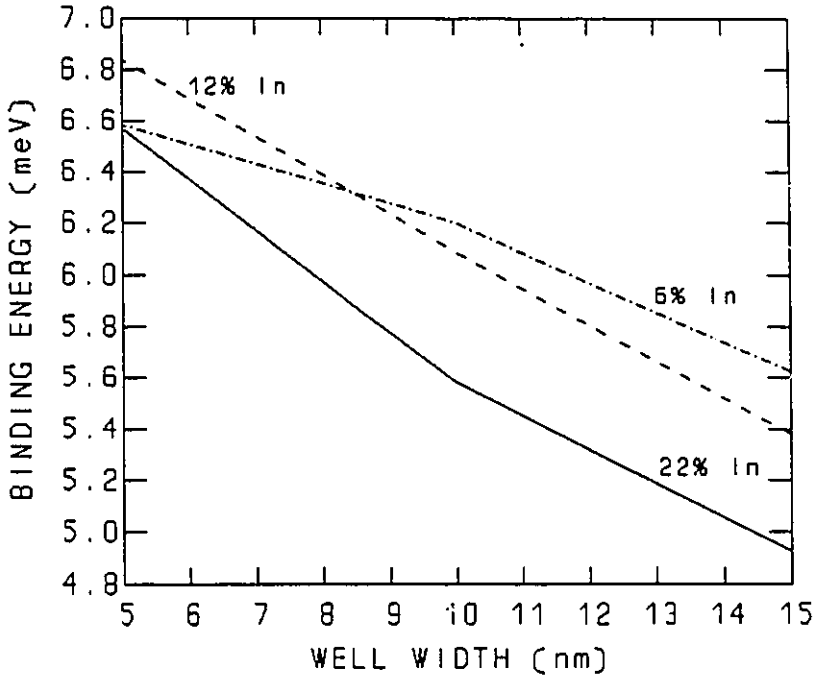


**Figure 9.10** The binding energy of the absorption-edge 1-s exciton state vs. $In_xGa_{1-x}As$ quantum-well width for indium fractions of 6%, 12%, and 22%. The electric field is zero.

The exciton strength is also proportional to the square of the radial portion of the wavefunction at the separation distance $\rho = 0$ [Elliott, 1952]. This value is generally larger for higher binding energies. A comparison of exciton binding energies vs. well width is given in Figure 9.10 for three indium fractions. The wider well widths generally have smaller binding energies. This is because the narrower wells have greater carrier confinement, meaning the electron and hole interact more. Of course a zero-width well has no confinement, so this binding energy trend must change for very narrow wells. The surprising aspect of Figure 9.10 is that the larger indium-concentration wells tend to have smaller binding energies, despite having

improved carrier confinement. The solution is that the deeper wells also have a smaller parallel heavy-hole mass. The increased strain in these higher indium concentration wells splits the light and heavy-hole bands to such a degree that the bands become almost totally decoupled, and the parallel hole mass approaches the low value of $m_0/(\gamma_1+\gamma_2)$ (the calculated masses are given in Figure 9.2). Also, we assume a dielectric constant $\epsilon_r$ equal to that of the $In_xGa_{1-x}As$ material in the binding-energy calculations, which is given by [Hellwege, 1982] $\epsilon_r = 12.8 + 3.35x$. The larger dielectric constant in larger indium-fraction wells also helps reduce the binding energy. This reduction in binding energy with well depth is probably opposite to the trend for unstrained systems such as AlGaAs-GaAs quantum wells.

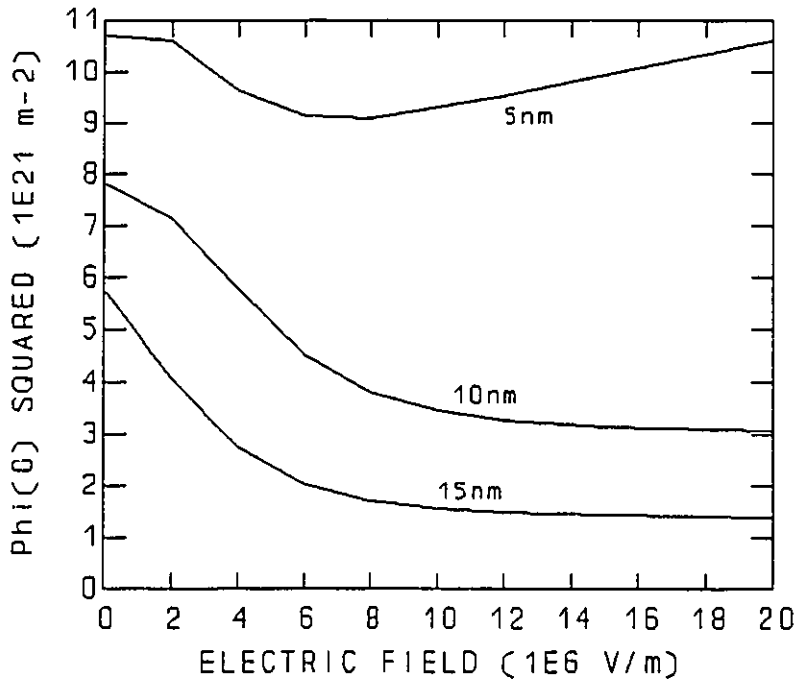


**Figure 9.11** The square of the radial part of the exciton wavefunction at $\rho = 0$ vs. electric field for 12% indium-fraction $In_xGa_{1-x}As$ quantum wells with widths of 5nm, 10nm, and 15nm.

The square of the radial binding energy for zero electron-hole separation vs. electric field is given in Figure 9.11. The graphs are for 12% indium-fraction wells and for well widths of 5nm, 10n, and 15nm. The narrower wells have a larger $\phi(0)^2$ value than wider wells, again due to a greater carrier confinement and a larger binding energy. The $\phi(0)^2$ value generally drops with field, as the electron and hole are forced apart by the electric field. For the very narrow 5nm well, however, the value does not change significantly. The increase with field is probably due to the greater electron effective mass experienced by the electron within the barrier GaAs

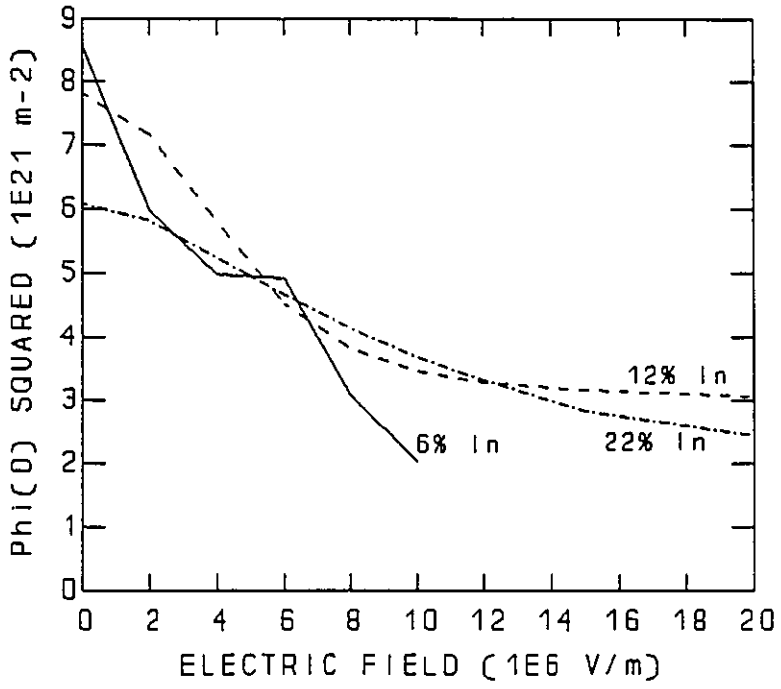


**Figure 9.12** The square of the radial part of the exciton wavefunction at $\rho = 0$ vs. electric field for 10nm-wide $In_xGa_{1-x}As$ quantum wells with indium fractions of 6%, 12%, and 22%.

material. However, it is clear that $\phi(0)^2$ is less affected by field in the 5nm well. This is good for modulator performance, but unfortunately we have seen earlier that this well also exhibits less energy shift with field.

The variation of $\phi(0)^2$ with field for 10nm wells for 6%, 12%, and 22% indium fraction wells is given in Figure 9.12. The difference between curves is not large. The 6% indium curve drops slightly faster with field because of tunnelling to the continuum. A comparison of the value of $\phi(0)^2$ for zero field between curves is explained by the binding energy calculations of Figure 9.10.

## 9.4 Discussion of Modulator Design

The first step in modulator design is to determine what factors are most important. Some performance factors which may be important are insertion loss, switching ratio, maximum switching frequency, voltage of operation, reliability, maximum optical power switchable, and frequency chirp. Chirping occurs during switching as the index of refraction changes. The rate of change of refractive index as compared to absorption determines the degree of chirp. Determining this is a topic for future research. The factors affecting reliability are difficult to determine, but one would expect that dislocations may result in current leakage paths over time. As long as one can sweep the photogenerated carriers out of the wells fast enough that they don't build up and screen the excitons, or screen the applied field, one doesn't have to worry about maximum switchable power. This would require the wells not being extremely deep. Speed has not been directly considered in this work because facilities were not available to measure it, but it should essentially be determined by the RC time constant of the device. As an estimate of speed performance, a modulator 100$\mu$m-long and 4$\mu$m wide processed from material A would have a capacitance of $6 \times 10^{13}$ Farads, and a maximum frequency of 50GHz. The other performance factors can be estimated from the calculations done in this chapter for $In_xGa_{1-x}As$ quantum wells lattice matched to the GaAs barriers.

Bulk materials work as electro-absorption modulators due to the Franz-Keldysh effect [Franz, 1958][Aspnes, 1966]. Therefore wide wells will perform as modulators, but they will not give optimum performance. A very narrow well requires large fields for switching and is very susceptible to well-thickness non-uniformity. The optimum design for speed would require a wide intrinsic region for low capacitance, and many wells for a large confinement factor and absorption coefficient. This would most likely require a dislocated structure, although one might be able to use a lattice matched structure with small indium concentration. For optimum switching ratios and small low-field loss, one would probably want a structure with a well width between 6.5nm and 13nm. The indium concentration should not be too large, since deep wells have smaller hole effective masses and therefore smaller low-field binding energies. Too small an indium concentration would result in an increased phonon scattering (not calculated in this thesis) and lower binding energies. However, Goossen et al. [Goossen, 1990] have seen sharp low-field absorption edges which rapidly broaden at low fields in $Al_{.02}Ga_{.98}As$-GaAs quantum wells. Therefore, as long as a strong absolute absorption change is not needed, shallow wells may in fact be advantageous for switching at low fields. Therefore I would say that indium fractions from about 3% to 17% may be optimal for $In_xGa_{1-x}As$-GaAs absorption modulators. With such a wide range of parameters to choose from, it is worth mentioning that the main criterion for good switching in any modulator is that the absorption edge at low field be sharp. This requires good layer uniformity, a minimum of alloy broadening, and small low-field phonon scattering.

# CHAPTER 10

# CONCLUSIONS

## 10.1 CONCLUSIONS

In this work, electric field induced changes in the excitonic band-edge absorption spectra of $In_xGa_{1-x}As$-GaAs Multiple Quantum Well (MQW) structures were investigated theoretically and experimentally. Emphasis was given to understanding and modelling the excitonic electro-absorption process, but experimental absorption and photocurrent spectra were vital to interpretation of the results. Since one of the purposes of doing this modelling was to understand optical modulator performance, waveguide modulators were processed from three different material growths. Transmission measurements showed high switching ratios with low loss.

The first step in being able to model absorption in semiconductor quantum wells under applied electric field is to calculate the allowed quantum-well energies and wavefunctions. To do this, we employed three exactly solvable methods. They are the discrete solution method [Hunt, 1991a], the resonant tunnelling method [Ghatak, 1988], and the complex-energy method. The first two methods have been employed independently by Ghatak [Ghatak, 1990] in the past for a parabolic conduction band using Airy functions, but the complex-energy method has not been done before with Airy functions. Also for the first time, all three exactly solvable methods were applied to the case of first-order conduction-band non-parabolicity

using parabolic cylinder functions. Comparisons of the methods showed that the resonant tunnelling calculation, with parabolic bands, was the most practical method, and was quite accurate.

Because the absorption edge at low field is dominated by the electron-1 to heavy-hole-1 exciton, one would like to be able to calculate the exciton wavefunction. First, however, one must derive a heavy-hole mass for carrier motion parallel to the layer planes. This was done by combining the exact solvability of Andreani's method [Andreani, 1987] and the matrix-size reduction of Broido's method [Broido, 1985] for calculating the heavy-hole dispersion curves. The resulting hole mass may be used in the exciton calculations without worrying about valence-band mixing due to the Coulomb interaction. This is true for our strained materials, but it may not be true for quantum wells with similar light-hole and heavy-hole energies.

The exciton Hamiltonian is not solvable analytically or by modern computers. Therefore we assume an exciton form separable in the growth (z-direction) and the radial (in-plane) directions. Assuming a z-direction wavefunction unperturbed by the Coulomb interaction, the radial portion of the exciton wavefunction was calculated numerically using the method of Wu for a single well [Wu, 1989]. We extended Wu's method, however, to a variational calculation of exciton wavefunctions and energies in true coupled quantum wells. It was determined that the single well approximation was sufficient for our experimental growths. Exciton broadening factors were then theoretically examined.

Transverse optical transmission (with light incident perpendicular to the sample front) and photocurrent measurements were performed on each of the three quantum-well structures. Two of these strained structures were dislocated from the substrate but with different numbers of wells. The third structure was strained to the

GaAs substrate lattice constant and had only 3 wells. The band-edge excitons in all materials displayed a red-shift, a broadening, and a reduction in absorption strength with field. The resulting family of transmission curves for various bias voltages showed that one could indeed get large absorption coefficient ratios between low-bias and high-reverse-bias at optical energies just below the bandgap. A comparison of experimental and theoretical electro-absorption spectra at moderate fields was favourable. The discrepancies were caused partly by ignoring the effects of broadened higher-energy transitions in the theoretical curves, and by the use of a Lorentzian shape for the tunnelling broadening at higher fields. At higher fields one should treat the absorption edge as a continuum of transitions. A model for this was developed which has some unique features. This extended the range of fields which could be accurately modelled, although the removal of excitons from this high field model causes some inaccuracies.

Slab and rib waveguide modulators were processed from the three material growths. The performance was similar between rib and slab, except it was easier to eliminate stray light from the rib measurements, thus increasing the maximum switching ratios measured. All rib-waveguide samples performed well. They typically exhibited over 20 dB of switching ratio over a 40nm wavelength range, with less than 3 dB of low-bias absorption loss. Scattering and coupling losses were not measured, but were high. Comparison of absorption with theory agreed reasonably well, with some discontinuity occurring between the low and high-field models. Differences were explained in terms of the same limitations as for the comparisons with transverse spectra earlier.

Various factors affecting modulator performance were calculated for well-widths between 5nm and 15nm, and for indium fractions between 6% and 22%.

Many trade-offs were evident. High indium-fraction wells have good carrier confinement, but have lower hole masses. Overall, the binding energies become reduced. At the other end of the scale, indium fractions lower than 6% would have little carrier confinement, reducing the binding energy. For wide wells, the band-edge energy solutions shift quicker with field, but the wavefunction overlaps drop faster also. The limit of wide wells is a bulk material. A narrow well, however, is extremely susceptible to low-field broadening due to well-width variations, and requires a larger field for a shift of the exciton. The structure chosen will depend on whether speed or high switching and low loss is the most important design factor. We give a guideline of 3% to 17% indium-fraction wells, with 6.5nm to 13nm wells.

## 10.2 RECOMMENDATIONS FOR FUTURE WORK

There are still a number of topics which still require study. For theoretical work, the problem of phonon scattering of excitons in quantum wells has not been fully examined in the literature. More complete calculations could be done, and it would be interesting to the see how phonon broadening changes with well parameters. This is particularly a problem with shallow wells, and is an interesting problem given the sharp excitons seen by Goossen et al. [Goossen, 1990] in shallow AlGaAs-GaAs quantum wells.

Experimentally, work could possibly be done on determining if small indium-fraction InGaAs-GaAs quantum wells exhibit suitable electroabsorption for use in waveguide devices. This could be done using only transverse measurements. Also interesting would be the use of AlGaAs-InGaAs quantum wells. While this might be too much like AlGaAs-GaAs systems to be novel, it would allow one to get extra carrier confinement without reducing the heavy-hole parallel effective mass as much.

# APPENDIX A

## An Exact Slab Waveguide Solution Method Including Losses

This appendix summarizes the method of Walpita [Walpita, 1985] for determining the eigenmode solutions to a dielectric slab waveguide. The resulting modes are exact solutions to the Transverse-Electric (TE) polarized or Transverse-Magnetic (TM) polarized waves travelling in a constant thickness multi-layer dielectric medium. For a situation involving no absorption losses, the electric field profile for waveguiding light will be a linear combination of the field profiles of the eigenmodes. This method is capable of caiculating bound eigenmodes, radiation modes, leaky modes, and modes which include absorption loss.

The coordinate system definition, and a drawing of a typical waveguide structure are given in Fig. A.1. The z-direction points normal to the surface of the waveguide. It is assumed that any individual light ray will propagate only in the x- and z-directions. Reflection of rays off the various material interfaces result in a wave moving mainly in the x-direction (exclusively in this direction for bound no-loss modes). Walpita assumes that the each of the $j$ materials have an isotropic magnetic permeability ($\mu_j$), but may or may not have a different electric permittivity in the z-direction as compared to the x- and y-directions. In such a situation, one can define the index of refraction in the z-direction as the extraordinary index $n_e$ and the index in the other directions becomes the ordinary index $n_o$. The relationship between the Electric field vector $E$ and the displacement vector $D$ becomes,

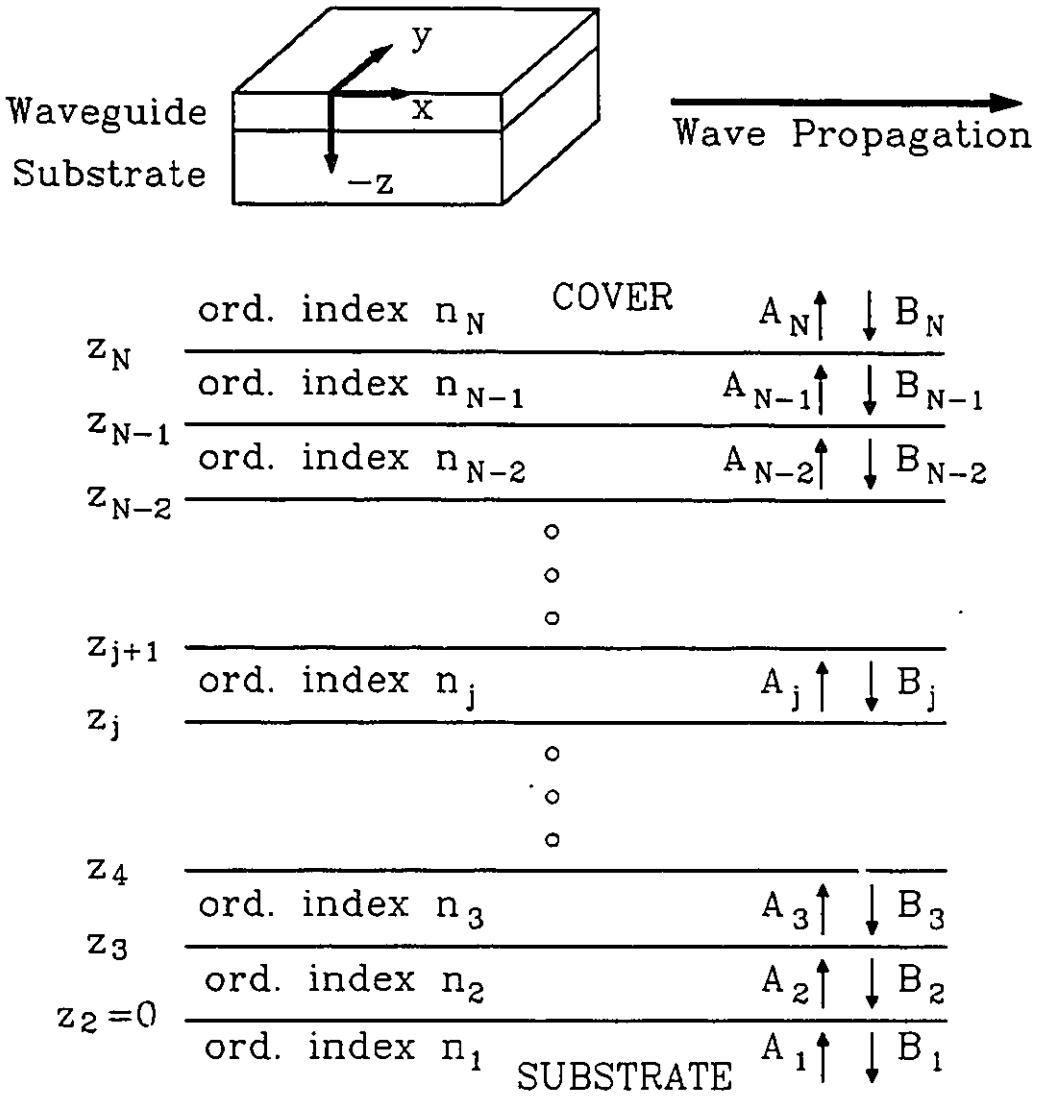


**Figure A.1** The co-ordinate definition, and the labelling conventions for the interfaces, the ordinary refractive indices, and the electric-field vectors corresponding to amplitudes $A_j$ and $B_j$.

$$\begin{bmatrix} D_x \\ D_y \\ D_z \end{bmatrix} = \epsilon_0 \begin{bmatrix} n_o^2 & 0 & 0 \\ 0 & n_o^2 & 0 \\ 0 & 0 & n_e^2 \end{bmatrix} \begin{bmatrix} E_x \\ E_y \\ E_z \end{bmatrix} \qquad \text{[A.1]}$$

where $\epsilon_0$ is the electric permittivity of free space. By solving Maxwell's equations, one can find that the wave equation for the electric field is,

$$\nabla^2 \vec{E}_j = \frac{1}{\mu_j} \frac{\partial^2 \vec{D}_j}{\partial t^2} \qquad \text{[A.2]}$$

One can relate the electric field $E_j$ and magnetic field $B_j = \mu_j H_j$ using the following forms of Maxwell's equations for a layer $j$ in the waveguide.

$$\nabla \times \vec{E} = -i\omega \vec{B} \qquad \text{[A.3]}$$

$$\nabla \times \vec{H}_j = i\omega \vec{D}_j \qquad \text{[A.4]}$$

The general electric-field solution for a waveguiding electro-magnetic wave in material $j$ is then,

$$\vec{E}_j = e^{-i(\beta x - \omega t)} \left[ A_j e^{-p_j (z - z_j)} + B_j e^{p_j (z - z_j)} \right] (E_{x0}, E_{y0}, E_{z0}) \qquad \text{[A.5]}$$

Here $t$ is time, $\omega$ is the angular frequency of the waves, $\beta$ is the x-direction wavevector, $p_j/i$ is the z-direction wavevector, and the vector $(E_{x0}, E_{y0}, E_{z0})$ is constant. The constant $z_j$ is the position of the interface between the layer $j$ and the layer $j$-$1$ for $j \geq 2$, and one defines $z_1 = z_2$. The values of the wavevectors and the $E$s will depend on the ordinary and extraordinary indices, and on whether the wave is TE or TM polarized. Since only TE-polarized waveguiding is analyzed in this thesis, it is sufficient to show only the TE result. The unknown variables in Eqn. A.5 then become,

$$p_j^2 = (\beta^2 - k^2 n_{0,j}^2) \ , \ -\frac{\pi}{2} \le \arg(p_j^2) < \frac{3\pi}{2} \qquad \text{[A.6]}$$

$$E_{x0}=0 \ , \ E_{y0}=1 \ , \ E_{z0}=0 \qquad \text{[A.7]}$$

This defines the $E$ and $B$ fields as follows,

$$\vec{E}_j = \left[A_j e^{-p_j(z-z_j)}(0,1,0) + B_j e^{p_j(z-z_j)}(0,1,0)\right] e^{-i(\beta x-\omega t)} \qquad \text{[A.8]}$$

$$\vec{B}_j = \frac{1}{i\omega}\left[A_j e^{-p_j(z-z_j)}(p_j,0,-i\beta) + B_j e^{p_j(z-z_j)}(-p_j,0,-i\beta)\right] e^{-i(\beta x-\omega t)} \qquad \text{[A.9]}$$

The coefficients $A_j$ and $B_j$ determine the amplitudes of the waves moving in the positive and negative z-directions respectively. The strategy for determining the values of $A_j$ and $B_j$ for each layer, and therefore the entire electric field distribution for the multi-layer waveguide, is to introduce suitable boundary conditions.

For a system consisting of $N$ layers there are $2N$ unknowns, and therefore one needs $2N$ boundary conditions for a well defined solution. If layer $1$ corresponds to the layer in the negative-most $z$-direction (the substrate), then the boundary conditions are as follows for a TE-polarized wave:

$$A_1 = 0 \ , \ \text{and} \ \ B_N = 0 \qquad \text{[A.10]}$$

$$E_{yj}|_{z_j} = E_{yj-1}|_{z_j} \ , \ \text{and} \ \ B_{xj}|_{z_j} = B_{xj-1}|_{z_j} \ , \ j \in (2..N) \qquad \text{[A.11]}$$

This means that there is continuity of $E_y$ and $B_x$ at the interfaces between layers. This condition means that the following vector is continuous,

$$\begin{bmatrix} E_{y,j} \\ i\omega B_{x,j} \end{bmatrix} = \begin{bmatrix} e^{-p_j(z-z_j)} & e^{p_j(z-z_j)} \\ -\Gamma_j e^{-p_j(z-z_j)} & \Gamma_j e^{p_j(z-z_j)} \end{bmatrix} \begin{bmatrix} A_j \\ B_j \end{bmatrix} \qquad \text{[A.12]}$$

where $\Gamma_j = p_j$ for TE modes

If the matrix in Eqn. A.12 is represented by the symbol $M_j$ then the continuity condition can be used to find the following formula relating the coefficients $A$ and $B$ for adjoining layers.

$$\begin{bmatrix} A_j \\ B_j \end{bmatrix} = \left[M_j\right]^{-1}_{z=z_j} \left[M_{j-1}\right]_{z=z_j} \begin{bmatrix} A_{j-1} \\ B_{j-1} \end{bmatrix} \qquad \text{[A.13]}$$

The inverse matrix $M_j^{-1}$ can be evaluated easily to give the following.

$$\begin{bmatrix} A_j \\ B_j \end{bmatrix} = \begin{bmatrix} \frac{1}{2} & -\frac{1}{2\Gamma_j} \\ \frac{1}{2} & \frac{1}{2\Gamma_j} \end{bmatrix} \left[M_{j-1}\right]_{z=z_j} \begin{bmatrix} A_{j-1} \\ B_{j-1} \end{bmatrix} \qquad \text{[A.14]}$$

Using this recursion formula, the matrices relating the different layer coefficients can be multiplied to give a 2x2 matrix relating layer *1* to layer *N*. If one also includes the boundary conditions of Eqn. A.10, one gets,

$$\begin{bmatrix} A_N \\ 0 \end{bmatrix} = \begin{bmatrix} a_1 & a_2 \\ a_3 & a_4 \end{bmatrix} \begin{bmatrix} 0 \\ B_1 \end{bmatrix} \qquad \text{[A.15]}$$

If one allows $B_1$ to be an arbitrary non-zero value, then the matrix element $a_4$ must be zero. To solve for the zero element one should step through different effective mode-index values $\beta/k$ and find a range in which the real part of $a_4$ changes sign. Enough steps should be used that different mode solutions will be separated. One then uses Newton's method to determine the value of $\beta$ at which the zero occurs.

For situations involving leaky waveguides, or materials with a complex index of refraction (such as metals), the effective mode wavevector $\beta$ will become complex. In this case a two-dimensional Newton's method is used to determine the complex $\beta$ value where $a_4$ is zero. In most cases, one can vary $\beta/k$ along the real axis just as for the real $\beta$ case, searching for a zero crossing in the real part of $a_4$. When a zero crossing is found, the real and imaginary axes become the two-dimensions of the Newton's method search for a true zero. It is possible for extremely high losses (or gains) that this method of initial search will not lead to a true solution. To account for these unlikely situations, one can alternatively initially search a grid of $\beta/k$ in the complex plane. In a rectangle defined by four neighbouring grid points, when the four $a_4$ values include both positive and negative values for both the real and imaginary parts, it can be assumed that the initial search is successful, and the solution is somewhere in the vicinity of the rectangle. The centre of the rectangle can then be used as a starting point for Newton's method. To reduce the chance of finding the same solution more than once, rectangles adjoining ones where the initial search is successful are disqualified from being starting values for a new solution. A successful search in any of these rectangles will still disqualify the rectangles adjacent to it, and so on. This may result in some solutions being missed if the grid is not fine enough.

A program called WAVEGUID has been written to calculate the mode solutions for no-loss and leaky or lossy waveguides. It uses the method of Walpita [Walpita, 1985] summarized here, and is a modification of an earlier program by P.E. Jessop which calculated only no-loss modes. The program also calculates the fraction of optical intensity in each layer of the waveguide structure.

# APPENDIX B

## A Franz-Keldysh-Like Method of Calculating Absorption

In the presence of high fields, one finds that the energy width of the lowest energy solution for a carrier in a quantum well is very large. This means that it is no longer adequate to model the solution as a Lorentzian-broadened single energy solution. One should treat the quantum-well as having a continuum of energy solutions. One should then be able to sum all possible energy transitions between electrons and holes to find the shape of the absorption edge. This appendix outlines how this is done. The formalism discussed here is a logical extension of Franz-Keldysh work done by Aspnes [Aspnes, 1966] and quantum-well work by Miller [Miller, 1984]. However, my formalism, using semi-infinite, analytically normalizable wavefunctions is new.

First consider the properties of the Airy function. For negative values of $Z_n$, one can say that [Abramowitz, 1964],

$$\mathrm{Ai}(Z_n) = M(-Z_n)\cos(\theta(-Z_n)) \ , \quad Z_n<0 \qquad \text{[B.1]}$$

$$\mathrm{Bi}(Z_n) = M(-Z_n)\sin(\theta(-Z_n)), \quad Z_n<0 \qquad \text{[B.2]}$$

That is, the Airy and Bairy functions are oscillatory functions, 90 degrees out of phase with each other. The magnitudes $M$ and arguments $\theta$ are, for large negative $Z_n$,

$$M^2(-Z_n) \approx \frac{1}{\pi}(-Z_n)^{-\frac{1}{2}}, \quad Z_n<<0 \qquad \textbf{[B.3]}$$

$$\theta(-Z_n) \approx \frac{\pi}{4} - \frac{2}{3}(-Z_n)^{\frac{3}{2}}, \quad Z_n<<0 \qquad \textbf{[B.4]}$$

Now, consider a envelope wavefunction $\psi_n$ for an electron (or hole) in a material layer n, which consists of a sum of Airy and Bairy functions. That is,

$$\psi_n = C_n \mathrm{Ai}(Z_n) + D_n \mathrm{Bi}(Z_n) \qquad \textbf{[B.5]}$$

This can be changed to the form,

$$\psi_n(Z_n) = \sqrt{C_n^2 + D_n^2}\, M(-Z_n)\cos\left(\theta(-Z_n) + \tan^{-1}\left(\frac{D_n}{C_n}\right)\right) \qquad \textbf{[B.6]}$$

We wish to determine the normalization constants for this wavefunction. To do this one needs to define the variable $Z_n$ in terms of the real space axis $z$. As given in Chapter 4, one has,

$$Z_n = \alpha_n[V_n + eFz - E_z], \quad \alpha_n = \left[\frac{2m_n^*}{(e\hbar F)^2}\right]^{\frac{1}{3}} \qquad \textbf{[B.7]}$$

This is a one-dimensional calculation, so $E_z$ means the Energy in the $z$-direction, and $V_n + eFz$ is the $z$-direction potential in layer $n$. The integration of the wavefunction probability from some finite value of $z$ (given by $z=z_0$ near $Z_n=0$), to the very large negative value of $z=-b$ (at $Z_n=-\beta$) is given by,

$$\int_{z=-b}^{z_0} \psi_n^2 dz \approx \frac{1}{2}(C_n^2 + D_n^2) \int_{Z_n=-\beta}^{0} M^2(-Z_n)\frac{dz}{dZ_n} dZ_n \qquad \textbf{[B.8]}$$

Remembering that $\beta \approx \alpha_n eFb$, this gives the following result,

$$\int_{z=-b}^{z_0} \psi_n^2 dz \approx (C_n^2 + D_n^2) \frac{\sqrt{b}}{\pi\sqrt{\alpha_n |eF|}} \qquad \textbf{[B.9]}$$

Because one wishes to normalize a wavefunction to equal *1*, Eqn. B.9 gives the normalization constant for the wavefunction. Assume that one is dealing with a semi-infinite layer with index $n=1$. The normalization constant $N$ is then,

$$N = \frac{\sqrt{\pi}}{\sqrt{C_1^2 + D_1^2}} \frac{\sqrt[4]{\alpha_1 |eF|}}{\sqrt[4]{b}} \qquad \textbf{[B.10]}$$

The next step is to determine the density of states per unit energy which occupy this layer of approximate width $b$. This requires finding the increment $\Delta Z$ near $Z=-\beta$ for a phase change of $\pi$.

$$\theta(\beta+\Delta Z) - \theta(\beta) = -\frac{2}{3}(\beta+\Delta Z)^{\frac{3}{2}} + \frac{2}{3}\beta^{\frac{3}{2}} \qquad \textbf{[B.11]}$$

Now, set the change equal to $\pi$.

$$\pi = \frac{2}{3}\beta^{\frac{3}{2}}\left(1-(1+\frac{\Delta Z}{\beta})^{\frac{3}{2}}\right) \qquad \textbf{[B.12]}$$

Use the first two terms of a binomial expansion to derive the following formula for $\Delta Z$,

$$\Delta Z = \pi \beta^{-\frac{1}{2}} \qquad \textbf{[B.13]}$$

One can use Eqn. B.7 to change $\Delta Z$ into an energy increment $\Delta E_z$, and can remember that $\beta = eFb$ to derive,

$$\Delta E_z = \frac{\pi}{\alpha_1^{3/2}\sqrt{|eF|b}} \qquad \textbf{[B.14]}$$

Therefore the one dimensional density of states in layer *1* with an extent about equal to *b*, is,

$$g_z(E_z)dE_z = \frac{\alpha_1^{3/2}\sqrt{|eF|b}}{\pi}dE_z \qquad \textbf{[B.15]}$$

Now that we have calculated both the normalization constants, and the density of states for a wave in a semiconductor layer with applied electric field, it is time to extend the calculation to the quantum well (or multiple quantum well) situation. Consider the diagram in Fig. B.1.

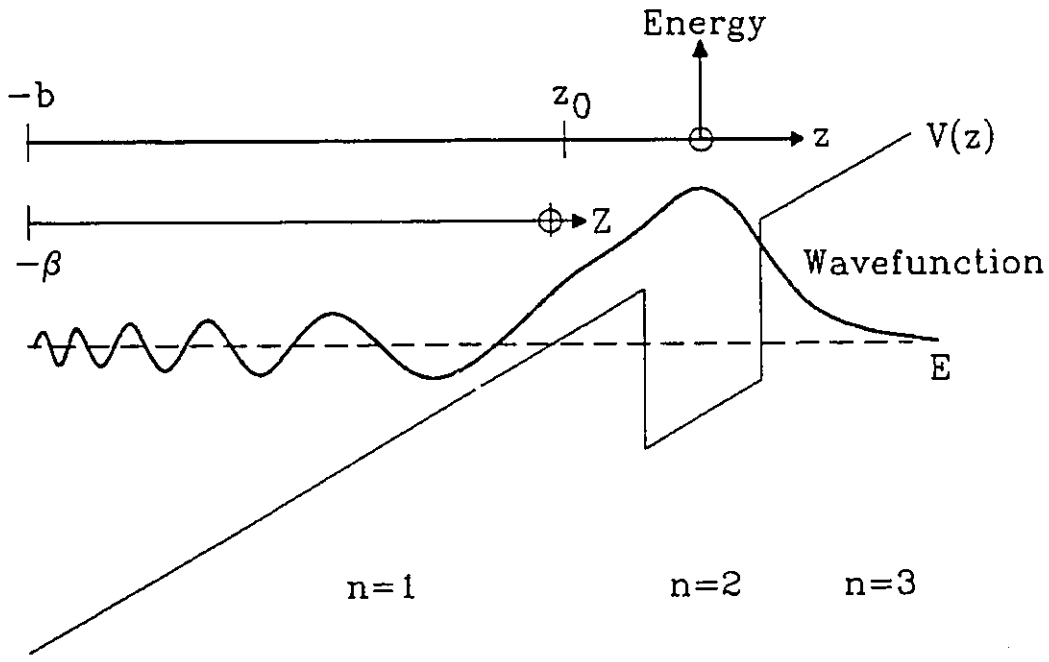


**Figure B.1** The real wavefunction for an energy E in a single quantum-well potential given by V(z). The z-value $z_0$ is near zero, while the value -b is semi-infinite.

Layer *1* is semi-infinite, so one can ignore the effect of the well on the

wavefunction normalization. This large extent also allows one to ignore the effect of any well-induced phase changes on the density of states. Therefore the normalization factor $N$ and the one-dimensional density of states $g_z(E_z)dE_z$ are correct for the entire multiple quantum well structure, not just layer *1*. Rather than rewriting the notation for the hole wavefunctions, it is easier to just flip over the hole band, and relabel the layers according to the convention given for electrons. The normalization constants for the electrons and holes can then be labelled $N_{ze}$ and $N_{zh}$. The density of states functions are then $g_{ze}(E_{ze})dE_{ze}$ and $g_{zh}(E_{zh})dE_{zh}$ (where $E_{zh}$ is given in terms of absolute electron potential). The total non-normalized wavefunctions for the electrons and holes are $\psi_{ze}(z)$ and $\psi_{zh}(z)$ (given in Eqn. B.6 for layer *1*). The absorption coefficient for a photon energy $h\nu$ is given by,

$$\alpha(h\nu) \propto \int\int N_{ze}^2 N_{zh}^2 \left|\langle \psi_{ze} | \psi_{zh} \rangle\right|^2 g_{ze}(E_{ze}) g_{zh}(E_{zh}) H(h\nu - E_{ze} + E_{zh}) dE_{ze} dE_{zh} \quad \textbf{[B.16]}$$

Here $H$ is the Heaviside function defined by,

$$H(\zeta) = \begin{cases} 0, & \zeta < 0 \\ 1, & \zeta \geq 0 \end{cases} \quad \textbf{[B.17]}$$

One finds in calculating Eqn. B.16 that the value of the semi-infinite extent $b$ of layer *1* cancels, since,

$$N_{ze}^2 \, g_{ze}(E_{ze})dE_{ze} = \frac{(\alpha_{1e})^2 |eF|}{C_1^2 + D_1^2} dE_{ze} \quad \textbf{[B.18]}$$

Because of broadening due to well-width variations, phonon scattering, and alloy randomness, one should convolve this absorption spectrum with a broadening function $\Gamma(E)$, which consists of both Gaussian and Lorentzian energy widths $\Delta_G$ and $\Delta_L$. It can be defined in terms of the Voigt function [Hui, 1978] $K(x,y)$ as follows,

$$\Gamma(E) = \frac{2\sqrt{\ln 2}}{\sqrt{\pi}\Delta_G} K\left(\frac{2E\sqrt{\ln 2}}{\Delta_G}, \frac{\Delta_L\sqrt{\ln 2}}{\Delta_G}\right) \qquad \textbf{[B.19]}$$

$$K(x,y) = \frac{y}{\pi}\int_{-\infty}^{\infty} \frac{e^{-t^2}}{y^2+(x-t)^2}\,dt \qquad \textbf{[B.20]}$$

A rational approximation is used to evaluate the Voigt function. The final broadened absorption spectrum $\alpha_{broad}(h\nu)$ is described by the following convolution.

$$\alpha_{broad}(h\nu) = \int_{-\infty}^{\infty} \Gamma(E)\alpha(h\nu - E)dE \qquad \textbf{[B.21]}$$

The actual implementation of this calculation requires the use of discrete wavefunctions calculated at some small spacing apart. How small a spacing? One must be able to approximate the overlap integral of the hole and electron wavefunctions for all the energies within a certain range as a constant. This is similar to saying that the wavefunction must be reasonably constant within its energy spacing. If this condition is met, then one can calculate the spectrum for the absorption edge by summing all discrete transitions.

# APPENDIX C

## Calculation of the Airy and Bairy Functions and Their Derivatives

The Airy and Bairy functions, given by the symbols Ai and Bi, are the solutions to the differential equation,

$$\frac{d^2\psi}{dZ^2} - Z\psi = 0 \qquad \text{[C.1]}$$

This equation is the solution to the wavefunction of a charged particle in a constant electric field, as shown in the quantum-well calculations of Chapter 4. Given in this appendix are the formulas for calculation of the Airy and Bairy functions and their derivatives, for different ranges of the complex variable $Z$. While many of the calculations for different situations are similar, it was decided that changing the format of Abramowitz [Abramowitz, 1964] to reduce space would add extra confusion. While these similarities were employed to reduce the size of the computer program needed to calculate the results, each formula will be expressed separately here. All formulas are from Abramowitz and Stegun [Abramowitz, 1964], although the ranges used for each formula were determined by trial and error, using a 10-byte representation for real numbers. This gives approximately 20 digits of accuracy. A computer with only an 8-byte real-number representation would need different ranges for maximum accuracy, and would possibly give poor accuracy where formulas for different ranges are joined. In the present calculations, it is estimated that the error is always less than $10^{-9}$ of the magnitude of the function envelope.

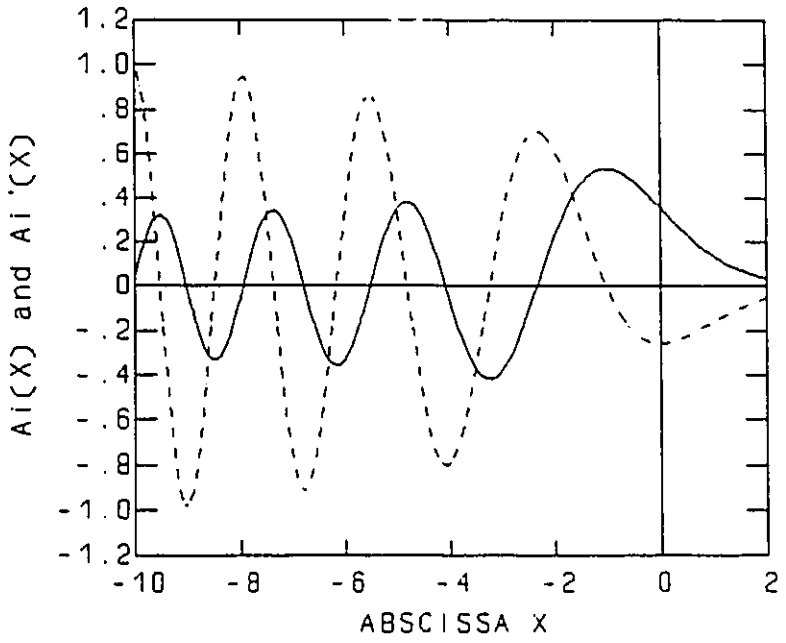


**Figure C.1** A graph of the Airy function Ai(*X*) and its derivative Ai'(*X*) for values of *X* between -10 and 2.

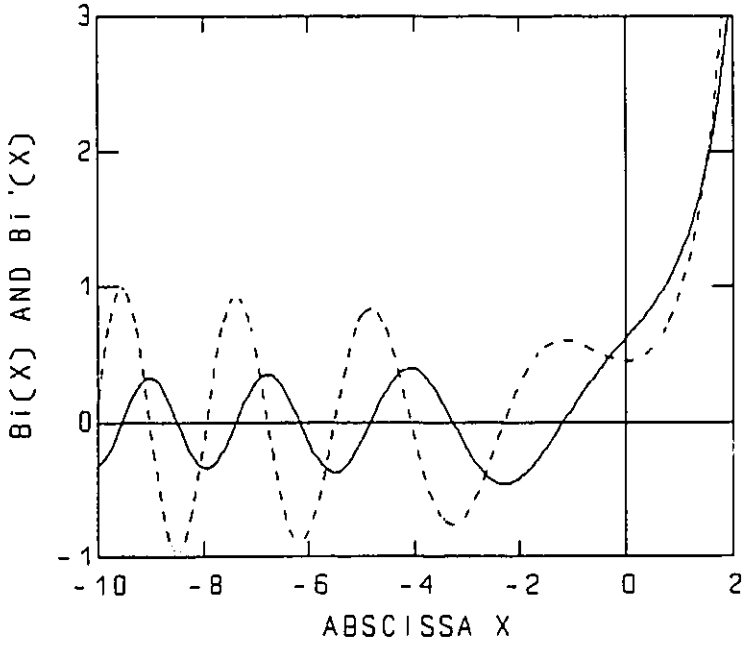


**Figure C.2** A graph of the Bairy function Bi(*X*) and its derivative Bi'(*X*) for values of *X* from -10 to 2.

First, some constants will be defined.

$$c_0 = 1 \ , \ c_k = \frac{\Gamma\left(3k+\frac{1}{2}\right)}{54^k k!\,\Gamma\left(k+\frac{1}{2}\right)} = \frac{(2k+1)(2k+3)...(6k-1)}{216^k k!} \qquad \text{[C.2]}$$

$$d_0 = 0 \ , \ d_k = -\frac{6k+1}{6k-1} c_k \quad (k=1,2,3,...) \qquad \text{[C.3]}$$

These constants for $k<61$ are pre-calculated to improve speed on future calculations. Next, a new variable, $\zeta$ will be introduced, which will be a function of $z$.

$$\zeta = \frac{2}{3} z^{3/2} \qquad \text{[C.4]}$$

It should be realized that in all the following formulas, unless otherwise stated, the functions of $z$ require the real part of $z$ to be greater than zero (or $|\arg(z)| < \pi/2$), while the functions of $-z$ require the real part of $z$ to be greater than or equal to zero (or $|\arg(z)| < \pi/2$).

## The Airy Function, Ai

$$\mathrm{Ai}(z) = \frac{1}{3}\sqrt{z}\left[I_{-1/3}(\zeta) - I_{1/3}(\zeta)\right] , \quad \mathrm{mag}(z) \le 6.5 \qquad \text{[C.5]}$$

$$\mathrm{Ai}(z) \approx \frac{1}{2}\pi^{-1/2} z^{-1/4} e^{-\zeta} \sum_{0}^{N} (-1)^k c_k \zeta^{-\zeta} \ , \ \mathrm{mag}(z) > 6.5 \qquad \text{[C.6]}$$

$$\mathrm{Ai}(-z) = \frac{1}{3}\sqrt{z}\left[J_{1/3}(\zeta) + J_{-1/3}(\zeta)\right] , \quad \mathrm{mag}(z) < 9 \qquad \text{[C.7]}$$

$$\mathrm{Ai}(-z) \approx \pi^{-1/2} z^{-1/4} \left[ \sin\left(\zeta + \frac{\pi}{4}\right) \sum_{0}^{N} (-1)^k c_{2k} \zeta^{-2k} - \cos\left(\zeta + \frac{\pi}{4}\right) \sum_{0}^{N} (-1)^k c_{2k+1} \zeta^{-2k-1} \right] \quad [C.8]$$

Eqn. C.8 is used on the range mag($z$)≥9. The four equations together cover the entire complex plane. The Bessel functions $I$ and $J$ will be defined later. The summation limit $N$ can be defined as the largest integer whereby the magnitude of the terms are still decreasing, or the index at which the terms are smaller than the last significant digit of the sum (whichever comes first).

## The Bairy Function, Bi

$$\mathrm{Bi}(z) = \sqrt{\frac{z}{3}} \left[ I_{-1/3}(\zeta) + I_{1/3}(\zeta) \right], \quad \mathrm{mag}(z) \le 8.5 \quad [C.9]$$

$$\mathrm{Bi}(z e^{\pm \pi i/3}) \approx \sqrt{\frac{2}{\pi}} e^{\pm \pi i/6} z^{-1/4} \left[ \sin\left(\zeta + \frac{\pi}{4} \mp \frac{i}{2} \ln 2\right) \sum_{0}^{N} (-1)^k c_{2k} \zeta^{-2k} \right.$$
$$\left. - \cos\left(\zeta + \frac{\pi}{4} \mp \frac{i}{2} \ln 2\right) \sum_{0}^{N} (-1)^k c_{2k+1} \zeta^{-2k-1} \right], \quad \mathrm{mag}(z) > 8.5 \quad [C.10]$$

$$\mathrm{Bi}(-z) = \sqrt{\frac{z}{3}} \left[ J_{-1/3}(\zeta) - J_{1/3}(\zeta) \right], \quad \mathrm{mag}(z) < 8.5 \quad [C.11]$$

$$\mathrm{Bi}(-z) \approx \pi^{-1/2} z^{-1/4} \left[ \cos\left(\zeta + \frac{\pi}{4}\right) \sum_{0}^{N} (-1)^k c_{2k} \zeta^{-2k} + \sin\left(\zeta + \frac{\pi}{4}\right) \sum_{0}^{N} (-1)^k c_{2k+1} \zeta^{-2k-1} \right] \quad [C.12]$$

Eqn. C.12 is used on the range mag($z$)≥8.5. Eqn C.10 is used for $ze^{\pm \pi i/3}$ with positive real values. Eqn. C.10 has ± and ∓ symbols in it. The upper symbol is used for values of $ze^{\pm \pi i/3}$ in the first quadrant, and the lower symbol is used for $ze^{\pm \pi i/3}$ in the fourth quadrant.

**The Derivative of the Airy Function, Ai'**

$$\mathrm{Ai}'(z) = -\frac{1}{3}z\left[I_{-2/3}(\zeta) - I_{2/3}(\zeta)\right], \quad \mathrm{mag}(z) \le 6.5 \qquad \text{[C.13]}$$

$$\mathrm{Ai}'(z) \approx -\frac{1}{2}\pi^{-1/2}z^{1/4}e^{-\zeta}\sum_{0}^{N}(-1)^k d_k \zeta^{-\zeta}, \quad \mathrm{mag}(z) > 6.5 \qquad \text{[C.14]}$$

$$\mathrm{Ai}'(-z) = -\frac{1}{3}\sqrt{z}\left[J_{-2/3}(\zeta) - J_{2/3}(\zeta)\right], \quad \mathrm{mag}(z) < 9 \qquad \text{[C.15]}$$

$$\mathrm{Ai}'(-z) \approx -\pi^{-1/2}z^{1/4}\left[\cos\left(\zeta+\frac{\pi}{4}\right)\sum_{0}^{N}(-1)^k d_{2k}\zeta^{-2k} + \sin\left(\zeta+\frac{\pi}{4}\right)\sum_{0}^{N}(-1)^k d_{2k+1}\zeta^{-2k-1}\right] \qquad \text{[C.16]}$$

**The Derivative of the Bairy Function, Bi'**

$$\mathrm{Bi}'(z) = \frac{z}{\sqrt{3}}\left[I_{-2/3}(\zeta) + I_{2/3}(\zeta)\right], \quad \mathrm{mag}(z) \le 8.5 \qquad \text{[C.17]}$$

$$\mathrm{Bi}'(ze^{\pm\pi i/3}) \approx \sqrt{\frac{2}{\pi}}e^{\mp\pi i/6}z^{1/4}\left[\cos\left(\zeta+\frac{\pi}{4}\mp\frac{i}{2}\ln 2\right)\sum_{0}^{N}(-1)^k d_{2k}\zeta^{-2k}\right.$$
$$\left.+\sin\left(\zeta+\frac{\pi}{4}\mp\frac{i}{2}\ln 2\right)\sum_{0}^{N}(-1)^k d_{2k+1}\zeta^{-2k-1}\right], \quad \mathrm{mag}(z) > 8.5 \qquad \text{[C.18]}$$

$$\mathrm{Bi}'(-z) = \frac{z}{\sqrt{3}}\left[J_{-2/3}(\zeta) + J_{2/3}(\zeta)\right], \quad \mathrm{mag}(z) < 8.5 \qquad \text{[C.19]}$$

$$\mathrm{Bi}'(-z) \approx \pi^{-1/2}z^{1/4}\left[\sin\left(\zeta+\frac{\pi}{4}\right)\sum_{0}^{N}(-1)^k d_{2k}\zeta^{-2k} - \cos\left(\zeta+\frac{\pi}{4}\right)\sum_{0}^{N}(-1)^k d_{2k+1}\zeta^{-2k-1}\right] \qquad \text{[C.20]}$$

Eqn. C.20 is used on the range $\mathrm{mag}(z) \ge 8.5$. Eqn C.18 is used for $ze^{\pm\pi i/3}$ with positive real values. Eqn. C.18 has $\pm$ and $\mp$ symbols in it. The upper symbol is used for

values of $ze^{\pm\pi i/3}$ in the first quadrant, and the lower symbol is used for $ze^{\pm\pi i/3}$ in the fourth quadrant.

## The Bessel Functions $I_\nu(z)$ and $J_\nu(z)$

The Bessel Functions are used to calculate the Airy and Bairy functions for small $z$. The formulas used for calculating these functions are given as follows.

$$I_\nu(z) = \left(\frac{1}{2}z\right)^\nu \sum_{k=0}^{\infty} \frac{\left(\frac{1}{4}z^2\right)^k}{k!\,\Gamma(\nu+k+1)} \qquad [C.21]$$

$$J_\nu(z) = \left(\frac{1}{2}z\right)^\nu \sum_{k=0}^{\infty} \frac{\left(-\frac{1}{4}z^2\right)^k}{k!\,\Gamma(\nu+k+1)} \qquad [C.22]$$

The sum is calculated until the last term is smaller than the least-significant digit of the sum. Now, the values of the Gamma functions can be evaluated using the recursion formula,

$$\Gamma(\nu+n+1) = (\nu+n)\Gamma(\nu+n) \qquad [C.23]$$

and by using the following $\Gamma$ values.

$\Gamma(-2/3)$ = -4.018407802061621450483 5
$\Gamma(-1/3)$ = -4.062353818279201250835 8
$\Gamma(1/3)$ = 2.678938534707747633655 7
$\Gamma(2/3)$ = 1.354117939426400416945 3
$\Gamma(4/3)$ = 0.892979511569249211218 56
$\Gamma(5/3)$ = 0.902745292950933611296 86

The terms $k!\Gamma(\nu+k+1)$ are pre-calculated for $k<61$ to improve speed on future Bessel function calls, thereby improving the speed of Airy and Bairy function calculations.

# APPENDIX D

## The Modified Parabolic Cylinder Functions $A^W$ and $B^W$

The Schrodinger equation for a charged particle in an electric field, with an effective mass which changed linearly with kinetic energy can be shown to reduce to the form (see Chapter 4),

$$\frac{d^2\psi}{dX^2} + (X^2-\epsilon)\psi = 0 , \quad X>\sqrt{\epsilon} \qquad \text{[D.1]}$$

While this is only the solution in a single material layer $n$, the index n is dropped here to avoid confusion and double indices later in this appendix. Here $\psi$ is the wavefunction in material $n$, $X$ is a linear function of kinetic energy and any imaginary component of energy, and $\epsilon$ is a constant. If the energy is complex, the wavefunction and both $X$ and $\epsilon$ will also be complex. The solutions are parabolic cylinder functions, but it turns out that these are very difficult to calculate except for the limiting case of large $X$. Shown here will therefore be a general series solution, which can be expanded about any point. Solutions for different ranges must be joined together to provide a means of calculating the function values at any point.

A Frobenius-type solution will be used. That means that one assumes a series solution of the form,

$$\psi \propto \sum_{m=-\infty}^{\infty} a_m(x-b)^{m+q} , \quad a_p=0, \text{ for } p<0 \qquad \text{[D.2]}$$

One finds, after substituting this into Eqn. D.1, that a solution is that $q=0$, and that

$a_0$ and $a_1$ may have any value. Two distinct situations exist,

$$\begin{cases} a_0 = 0 \ , \ a_1 = 1 \ , \text{ for odd solution about } b \\ a_0 = 1 \ , \ a_1 = 0 \ , \text{ for even solution about } b \end{cases} \qquad \text{[D.3]}$$

The recursion formula used to get all subsequent $a_m$ values for either solution situation is,

$$a_{m+2} = \frac{-(b^2-\epsilon)a_m - 2ba_{m-1} - a_{m-2}}{(m+1)(m+2)} \ , \quad m \geq 0 \ , \ m \in \mathbf{I} \qquad \text{[D.4]}$$

The two solutions are only 'even' and 'odd' in the limit of small excursions along the real axis away from the expansion point $b$.

As mentioned in chap. 4., our purpose is to define functions $A^w$ and $B^w$ for material layer $n$ which are the two independent solutions to Schrodinger's equation. Eqn. D.1 is only used for regions where the kinetic energy $K>0$. For $K \leq 0$, the effective mass is assumed constant, and the Airy differential equation applies, with solutions Ai and Bi, as given in chapter 4. The solutions $A^w$ and $B^w$ can therefore be given as,

$$A^w(K) = \begin{cases} s_{j,Aw}\sum_{m=0}^{\infty} a_{m,j,odd}(X-b_{j,Aw})^m + t_{j,Aw}\sum_{m=0}^{\infty} a_{m,j,even}(X-b_{j,Aw})^m \ , \ X_j < X < X_{j+1} \ , \ K>0 \\ \mathrm{Ai}(Z(K)) \ , \ Z = \left[\frac{2m^*}{(e\hbar F)^2}\right]^{\frac{1}{3}}(-K - iE_{im}) \ , \ i=\sqrt{-1} \ , \ K \leq 0 \end{cases}$$

[D.5]

$$B^w(K) = \begin{cases} s_{j,Bw}\sum_{m=0}^{\infty} a_{m,j,odd}(X-b_{j,Bw})^m + t_{j,Bw}\sum_{m=0}^{\infty} a_{m,j,even}(X-b_{j,Bw})^m \ , \ X_j < X < X_{j+1} \ , \ K>0 \\ \mathrm{Bi}(Z(K)) \ , \ Z = \left[\frac{2m^*}{(e\hbar F)^2}\right]^{\frac{1}{3}}(-K - iE_{m}) \ , \ K \leq 0 \end{cases}$$

[D.6]

the index $j$ refers to the fact that the series must be separated into sections, and

joined at the boundaries $X_j$ by using appropriate constants $s_j$ and $t_j$. The series must also be joined smoothly to the functions Ai or Bi at the interface $K=0$ ($X=\epsilon^{1/2}$ and $\mathrm{Re}(Z)=0$). A sample situation for the function $A^W$ is given in Figure D.1.

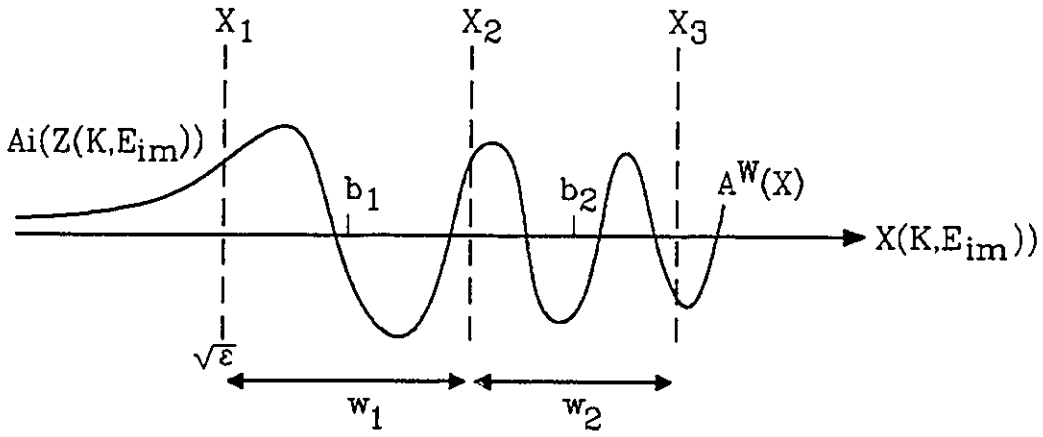


**Figure D.1** A typical function $A^W$ for a given value of $\epsilon$. The series are broken up into sections, each expanded around a point $b_j$, with an $X$-width $w_j$.

By solving for the values of $s_j$ and $t_j$ for each function $A^W$ and $B^W$ for a particular value of $\epsilon$ (which can be complex), one can then use the series definitions to evaluate the functions at any future time. When working with real values of $\epsilon$ and $X$, $\epsilon$ stays constant for all kinetic energies within a particular material type and electric field. This means that the series coefficients $s_j$ and $t_j$ can usually be pre-calculated for the material types and electric fields used. For complex $\epsilon$ and $X$, however, the coefficients are only useful for a constant imaginary component of $X$, which means that for random evaluations in the complex plane, the coefficients must be constantly re-evaluated. Fortunately, most routines were written to minimize jumping about on the imaginary axis.

Still to be explained is how to calculate the ranges for each series solution, and how to join the solutions. An appropriate formula for the range width, which

for small imaginary parts, loses about 8-digits of the floating point accuracy at the intersection between ranges is,

$$w_j = \frac{40}{\sqrt{(\Re e(X_j)+w_j)^2-\Re e(\epsilon)}} \qquad \text{[D.7]}$$

In fact, this can be reduced to a quadratic equation, but in general such an equation might be transcendental, and can be solved by iteration. Just substitute the answer back in the equation a few times to get the final result. To get the first range $w_1$, one knows that $X_1=\epsilon^{1/2}$, and can use as a starting guess that $w_1=(1600/(\mathrm{Re}(\epsilon))^{1/2})^{1/3}$. Once $w_1$ is found, one gets $X_2=X_1+w_1$. Using the final value of $w_1$ as the initial guess for $w_2$, iteration is used to find $w_2$, and so on. The range can be extended arbitrarily far, although the ranges do narrow up when one gets to larger $X$ values. As for the coefficients $s_j$ and $t_j$, they are determined by joining the ranges so that the functions $A^W$ and $B^W$ are smooth, and so are their first derivatives. One first determines $s_{1,Aw}$ and $t_{1,Aw}$ by setting up two equations, and by equating the series values in range $j=1$ and their derivatives to those of $\mathrm{Ai}(Z)$ at $K=0$. The coefficients in region $j=2$ can then be calculated using the appropriate boundary conditions at $X=X_2$, and so on for all ranges. The $s_{j,Bw}$ and $t_{j,Bw}$ values can be calculated similarly.

# APPENDIX E

## Detector and Current-to-Voltage Conversion Circuits

Most of the spectral measurements made in this thesis involved detection of low light levels. The spectral power coming out of a 0.7nm bandwidth from the monochromator was about 5 nW. The power coupled into a 4.5$\mu$m core fibre in a 2nm bandwidth was about 4 pW. The light transmitted from a fibre end, through a sample waveguide, and into a silicon detector was typically <400 fW. To maximize signal to noise, the detector circuit shown in Figure E.1 was built. The detector operates at zero bias, so one can characterize the internal noise of the silicon diode as Johnson noise. Johnson current noise per unit bandwidth $i_n$ for any resistance $R$ is given by,

$$i_n = \left(\frac{4k_BT}{R}\right)^{\frac{1}{2}} \qquad \text{[E.1]}$$

For an ideal op-amp, the input current noise power per unit bandwidth for the detector circuit is,

$$i_{n,input} = \left(\sqrt{i_{n,diode}} + \sqrt{i_{n,resist}}\right)^2 \qquad \text{[E.2]}$$

The diode resistance is about 50MΩ, and the total gain resistance in the detector is 19.5MΩ when measuring small signals. This results in a noise current of 48 fA/Hz$^{1/2}$. Measurements of the output noise on a lock-in amplifier resulted in a 33 fA/Hz$^{1/2}$ measured noise. The reason for the discrepancy is not clear. Perhaps the silicon

diode resistances are higher than expected, in which case it would have been advantageous to have increased the detector gain $2R$ to larger than 19.5MΩ.

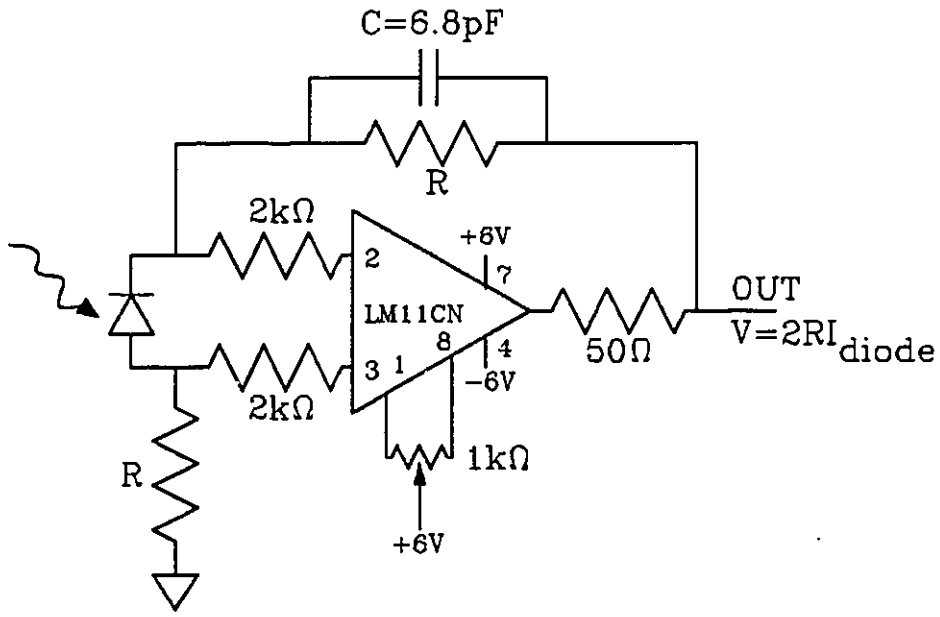


**Figure E.1** The detector circuit for the 2.5mm diameter silicon photodiodes used to measure light levels. The value of R is 9.75MΩ for detection of low light levels, but was reduced to 50kΩ when using the Ti-Sapphire laser source.

A similar circuit to that of Figure E.1 is used for convert photocurrents to output voltages, and is shown in Figure E.2. This circuit allows any bias voltage $V_{bias}$ to be applied to the sample. One must be careful that the voltage resulting from amplifying the leakage current through the feedback resistance $R$, is not larger than the op-amp power supply voltage. The feedback resistor must be chosen with this in mind. For low signal levels, and zero bias voltage, the resistance was as high as 2MΩ, while for high signal levels, and considerable bias voltage, it was as low as 5kΩ.

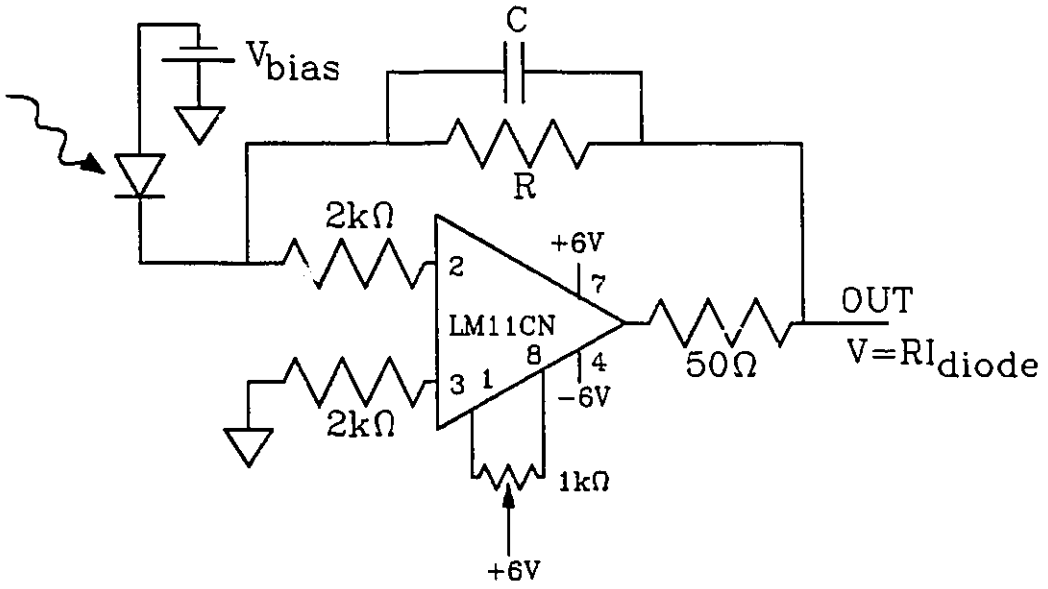


**Figure E.2** The current-to-voltage conversion circuit for measuring sample photocurrent at any reverse-bias voltage.

# APPENDIX F

## Valence-Band Continuity Condition at a Material Boundary

As shown in Equation 5.23, the valence-band Schrodinger equation in the envelope-function approximation is,

$$\left[\sum_q \tilde{H}_{pq} B_n^q + [V_n - E]\right] = 0 : \begin{cases} p,q \in \{1..2\} \text{ for upper} \\ p,q \in \{3..4\} \text{ for lower} \end{cases} \qquad \text{[F.1]}$$

One can easily rewrite this equation into a general tensor form in order to show how boundary conditions at the interface can be determined. Without explicitly defining the tensor elements, we have [Altarelli, 1983] [Krichbaum, 1986]:

$$\sum_q \left[(V_n - E + C_p \zeta_n)\delta_q^p + \sum_\alpha \sum_\beta \left[D_{pq}^{\alpha\beta} k_\alpha k_\beta\right]\right] B_n^q = 0 : \begin{cases} \alpha,\beta \in \{x,y,z\} \\ p,q \in \{\{1,2\} \\ \text{or } \{3,4\}\} \end{cases} \qquad \text{[F.2]}$$

We perform an integration on this equation along a path in the $z$-direction near an interface between two different layers [Krichbaum]. One gets:

$$\int_{z\text{-path}} (V_n - E + C_p \zeta) B_n^p dz + G_p^z k_z B_n^p + \sum_{\substack{q \\ q \neq p}} \sum_\alpha \left[(D_{pq}^{\alpha z} + D_{pq}^{z\alpha}) k_\alpha B_n^q\right] = 0 : p,q \in \begin{Bmatrix} \{1,2\} \\ \text{or} \{3,4\} \end{Bmatrix} \qquad \text{[F.3]}$$

$B_p$ must be continuous across a material boundary if the wavefunction $\Psi$ is. This means that the integral term in Eqn. F.3 is continuous across a boundary. Then:

$$G_p^z k_z B_n^p + \sum_{\substack{q \\ q \neq p}} \sum_{\alpha} \left[ (D_{pq}^{\alpha z} + D_{pq}^{z\alpha}) k_\alpha B_n^q \right] \text{ is continuous} \qquad \text{[F.4]}$$

This is slightly different than Altarelli's result [Altarelli, 1983] which is,

$$2G_p^z k_z B_n^p + \sum_{\substack{q \\ q \neq p}} \sum_{\alpha} \left[ (D_{pq}^{\alpha z} + D_{pq}^{z\alpha}) k_\alpha B_n^q \right] \text{ is continuous} \qquad \text{[F.5]}$$

We have tried both conditions, and find that the difference has very little effect on the calculated quantum-well solutions. Because Altarelli's result is widely used [Andreani, 1987], we have adopted it. By substituting the appropriate expressions into the tensors $G$ and $D$, one finds that the following vectors are continuous:

$$\bar{I}_n^U = \begin{bmatrix} (\gamma_1 - 2\gamma_2)k_z & -i\sqrt{3}\gamma_3 k_1 \\ i\sqrt{3}\gamma_3 k_1 & (\gamma_1 + 2\gamma_2)k_z \end{bmatrix} \begin{bmatrix} B_n^1 \\ P_n^2 \end{bmatrix} \text{ and } \bar{I}_n^L = \begin{bmatrix} (\gamma_1 + 2\gamma_2)k_z & -i\sqrt{3}\gamma_3 k_1 \\ i\sqrt{3}\gamma_3 k_1 & (\gamma_1 - 2\gamma_2)k_z \end{bmatrix} \begin{bmatrix} B_n^3 \\ B_n^4 \end{bmatrix} \qquad \text{[F.6]}$$

# REFERENCES


Abramowitz, M., and Stegun, I. A. 1964. Handbook of Mathematical Functions, Nat. Bureau of Standards, Washington, D.C.

Ahn, D., and Chuang, S.-L. 1988. "Optical Gain in a Strained-Layer Quantum-Well Laser." IEEE J. Quantum Electron. 24, 2400.

Altarelli, M. 1983. *in* Lecture notes in Physics 177, Application of High Magnetic Fields in Semiconductor Physics, edited by Landwehr, G., Springer-Verlag, Berlin.

Altarelli, M., Ekenberg, U., and Fasolino, A. 1985. "Calculations of hole subbands in semiconductor quantum wells and superlattices." Phys. Rev. B. 32, 5138.

Andreani, L. C., Pasquarello, A., and Bassani, F. 1987. "Hole subbands in strained GaAs-$Ga_{1-x}Al_xAs$ quantum wells: Exact solution of the effective-mass equation." Phys. Rev. B. 36, 5887.

Andreani, L. C., and Pasquarello, A. 1989. "Theory of excitons in GaAs-$Ga_{1-x}Al_xAs$ quantum wells including valence band mixing." Superlatt. and Microstruct. 5, 59.

Aspnes, D. E. 1966. "Electric-Field Effects on Optical Absorption near Thresholds in Solids." Phys. Rev. 147, 554.

Bastard, G. 1982a. "Theoretical investigations of superlattice band structure in the envelope-function approximation." Phys. Rev. B. 25, 7584.

Bastard, G., Mendez, E. E., Chang, L. L., and Esaki, L. 1982b. "Exciton binding energy in quantum wells." Phys. Rev. B. 26, 1974.

Bastard, G., and Brum, J. A. 1986. "Electronic States in Semiconductor Heterostructures" Invited Paper, IEEE J. Quantum Electron. QE-22, 1625.

Broido, D. A., and Sham, L. J. 1985. "Effective masses of holes at GaAs-AlGaAs heterojunctions." Phys. Rev. B. 31, 888.

Casey, H. C., Sell, D. D., and Panish, M. B. 1974. "Refractive index of $Al_xGa_{1-x}As$ between 1.2 and 1.8 eV." Appl. Phys. Lett. 24, 63.

Chemla, D. S., Miller, D. A. B., Smith, P. W. 1985. "Nonlinear optical properties of GaAs/GaAlAs multiple quantum well material: phenomena and applications." Opt. Engin. 24, 54.

Chippindale, C. L. 1990. AlGaAs/GaAs Electroabsorption Waveguide Modulators. M. Eng. Thesis, McMaster University, Hamilton.

Cho, H.-S., and Prucnal, P. R. 1989. "Effect of Parameter Variations of the Performance of GaAs/AlGaAs Multiple-Quantum-Well Electroabsorption Modulators." IEEE J. Quantum Electron. 25, 1682.

Coffey, D. 1988. "Photoabsorption due to excitons for InGaAs-GaAs superlattice quantum wells in the presence of an applied electric field." J. Appl. Phys. 63, 4626.

Coffey, D. 1989. "Contribution to the quantum-well exciton linewidth due to the intrasubband scattering by optical phonons in an applied electric field." Phys. Rev. B. 40, 11654.

Daly, M. G. 1990. An Infrared Optical Phase Modulator in GaAs and the QCSE in $Al_xGa_{1-x}As$-GaAs Quantum Wells. McMaster University, Hamilton.

Das, U. and Bhattacharya, P. K. 1985. "Variation of refractive index in strained $In_xGa_{1-x}As$-GaAs heterostructures." J. Appl. Phys. 1, 341.

Das, U., Berger, P. R., and Bhattacharya, P. K. 1987. "InGaAs/GaAs multiquantum-well electroabsorption modulator with integrated waveguide." Optics Lett. 12, 820.

Ekenberg, U., and Altarelli, M. 1987. "Exciton binding energy in a quantum well with inclusion of valence-band coupling and nonparabolicity." Phys. Rev. B. 35, 7585.

Elliott, R. J. 1952. "Intensity of Optical Absorption by Excitons." Phys. Rev. 108, 1384.

Franz, W. Z. "Einfluss Eines Elecktrishen Feldes auf Eine Optisore Absorptionskante." Naturforsch. 13, 484, 1958.

Ghatak, A. K., Thyagarahan, K., and Shenoy, M. R. 1988. "A Novel Numerical Technique for Solving the One-Dimensional Schroedinger Equation Using Matrix Approach -- Application to Quantum Well Structures." IEEE J. Quantum Electron. 24, 1524.

Ghatak, A. K., Goyal, I. C., and Gallawa, R. L. 1990. "Mean Lifetime Calculations of Quantum Well Structures: A Rigorous Analysis." IEEE J. Quantum Electron. 26, 305.

Goossen, K. W., Cunningham, J. E., and Jan, W. Y. 1990. "Excitonic electroabsorption in extremely shallow quantum wells." Appl. Phys. Lett. 57, 2582.

Hellwege, K.-H., *editor in chief.* 1982. Landolt-Bornstein, Numerical Data and Functional Relationships in Science and Technology, New Series, Volume 17a, *edited by* Madelung, O. Springer-Verlag, Berlin.

Hong, S. C., Jaffe, M., and Singh, J. 1987. "Theoretical Studies of Optical Modulation in Lattice Matched and Strained Quantum Wells Due to Transverse Electric Fields." IEEE J. Quantum Electron. QE-23, 2181.

Hui, A. K., Armstrong, B. H., Wray, A. A. 1978. "Rapid Computation of the Voigt and Complex Error Functions." J. Quant. Spectrosc. Radiat. Transfer. 19, 509.

Hunt, N. E. J., and Jessop, P. E. 1988a. "Lasing and High Intensity Photoluminescence in InGaAs-GaAs Strained layer superlattices." Superlatt. and Microstruct. 4, 671.

Hunt, N. E. J. 1988b. Photoluminescence and Optically-Pumped Gain and Lasing in $In_xGa_{1-x}As$-GaAs Strained-Layer Superlattices. M.Sc. Thesis, McMaster University, Hamilton.

Hunt, N. E. J., Jessop, P. E., and Wasilewski, Z. R. 1991a. "Experimental and theoretical electroabsorption in an InGaAs-GaAs strained-layer superlattice, and the performance of a wave-guide modulator." Can. J. Phys. 69, 483.

Hunt, N. E. J., and Jessop, P. E. 1991b. "Excitonic Band Edge Electro-absorption in Multiple Quantum-Well Waveguide Modulator Structures." Invited Paper. Int. J. Nonlinear Opt. Phys. 1, *in press*.

Kan, Y., Nagai, H., Yamanishi, M., and Suemune, I. 1987. "Field Effects on the Refractive Index and Absorption Coefficient in AlGaAs Quantum Well Structures and Their Feasibility for Electrooptic Device Applications." IEEE J. Quantum Electron. QE-23, 2167.

Krichbaum, M. 1986. "Envelope Function Calculations for Superlattices.", *in* Two-Dimensional Systems: Physics and New Devices, ed. Bauer, G, Kuchar, F., and Heinrich, H. Springer-Verlag, Berlin.

Larsson, A., Andrekson, P. A., Eng, S. T., and Yariv, A. 1988. "Tunable Superlattice p-i-n Photodetectors: Characteristics, Theory, and Applications." IEEE J. Quantum Electron. 24, 787.

Ludowise, M. J., Dietze, W. T., Lewis, C. R., Camras, M. D., Holonyak, N. Jr., Fuller, B. K., and Nixon, M. A. 1983. "Continuous 300-K laser operation of strained superlattices." Appl. Phys. Lett. 42, 487.

Luttinger, J. M. and Kohn, W. 1955. "Motion of Electrons and Holes in Perturturbed Periodic Fields." Phys. Rev. 97, 869.

Luttinger, J. M. 1956. "Quantum Theory of Cyclotron Resonance in Semiconductors: General Theory" Phys. Rev. 102, 1030.

Mendez, E. E., Agullo-Rueda, F., and Hong, J. M. 1990. "Temperature dependence of the electronic coherence of GaAs-GaAlAs superlattices." Appl. Phys. Lett. 56, 2545.

Miller, D. A. B., Chemla, D. S., Damen, T. C., Gossard, A. C., Wiegmann, W., Wood, T. H., Burrus, C. A. 1984. "Band-Edge Electroabsorption in Quantum Well Structures: The Quantum-Confined Stark Effect." Phys. Rev. Lett. 53, 2173.

Miller, D. A. B., Chemla, D. S., Damen, T. C., Gossard, A. C., Wiegmann, W., Wood, T. H., and Burrus, C. A. 1985. "Electric field dependence of optical absorption near the band gap of quantum-well structures." Phys. Rev. B. 32, 1043.

Mo, G., and Sung, C. C. 1988. "Bound exciton states of multiple-quantum-well structures in external fields." Phys. Rev. B. 38, 1978.

Nojima, S. 1988. "Electric field dependence of the exciton binding energy in GaAs\\$Al_xGa_{1-x}As$ quantum wells." Phys. Rev. B. 37, 9087.

Ogale, S. B., Madhukar, A., and Cho, N. M. 1987. "Influence of transverse electric field on the photoluminescence linewidth of excitonic transition in quantum wells: Alloy disorder and composition fluctuation contributions." J. Appl. Phys. 62, 1381.

Osbourn, G. C. 1982. "Strained-layer superlattices from lattice mismatched materials." J. Appl. Phys. 53, 1586.

Press, W. H., Flannery, B. P., Teukolsky, S. A., Vetterling, W. T. 1989. Numerical Recipes in Pascal, Cambridge University Press, Cambridge.

Rajan, K., Devine, R., Moore, W. T., and Maigne, P. 1987. "Dislocation structure in $In_xGa_{1-x}As/GaAs$ strained-layer superlattices." J. Appl. Phys. 62, 1713.

Rudin, S., and Reinecke, T. L. 1988. "Exciton linewidths due to LO phonon coupling in semiconductor quantum wells in the presence of applied electric fields." Solid State Commun. 68, 739.

Rudin, S., and Reinecke, T. L. 1990. "Temperature-dependent exciton linewidths in semiconductor quantum wells." Phys. Rev. B. 41, 3017.

Sanders, G. D., and Chang, Y. -C. 1985. "Effect of band hybridization on exciton states in $GaAs\text{-}Al_xGa_{1-x}As$ quantum wells." Phys. Rev. B. 32, 5517.

Sugawara, M., Fujii, T., Kondo, M., Kato, K., Domen, K., Yamazaki, S., and Nakajima, K. 1988. "Evaluation of exciton absorption peak broadening factors in InGaAsP/InP multiple quantum wells." Appl. Phys. Lett. 53, 2290.

Tarucha, S., and Ploog, K. 1987. "Electric Field Effects on Excitons in $Al_xGa_{1-x}As$ Quantum Wells and their Applications to Optoelectronic Devices." J. de Physique. C5, 85.

Twardowski, A., and Hermann, C. 1987. "Variational calculation of polarization of quantum-well photoluminescence." Phys. Rev. B. 35, 8144.

Weiner, J. S., Gossard, A. C., English, J. H., Miller, D. A. B., Chemla, D. S., and Burrus, C. A. 1987. "Low-Voltage Modulator and Self-Biased Self-Electro-Optic-Effect Device." Electron. Lett. 23, 75.

Wakita, K, Kawamura, Y., Yoshikuni, Y., Asahi, H. 1986. "Long-wavelength waveguide multiple-quantum-well (MQW) optical modulator with 30:1 ON/OFF ratio." Electron. Lett. 22, 907.

Walpita, L. M. 1985. "Solutions for planar optical waveguide equations by selectring zero elements in a characteristic matrix." J. Opt. Soc. Am. A. 2, 595.

Weisbuch, C. 1987. *in* Semiconductors and Semimetals, Vol. 24. Applications of Multiquantum Wells, Selective Doping, and Superlattices, *edited by* Dingle, R. Academic Press Inc., London.

Wu, J.-W. 1989. "Binding Energies of Wannier Excitons in Semiconductor Quantum Wells: Numerical integration of the in-plane radial equation." Solid State Comm. 69, 1057.